

© [2012]

Kisa Mwakanyamale

ALL RIGHTS RESERVED

A geophysical characterization and monitoring strategy for determining controls on
groundwater-surface water exchange regulating contaminant transport at the Hanford

300-Area

by

Kisa Mwakanyamale

A Dissertation submitted to the

Graduate School – Newark

Rutgers, The State University of New Jersey

in partial fulfillment of the requirements

for the degree of

Doctor of Philosophy

Graduate Program in

Environmental Sciences

written under the direction of

Professor Lee D. Slater

and approved by

Newark, New Jersey

October, 2012

ABSTRACT OF THE DISSERTATION

A geophysical characterization and monitoring strategy for determining controls on groundwater-surface water exchange regulating contaminant transport at the Hanford

300-Area

By Kisa Mwakanyamale

Dissertation Director:

Professor Lee D. Slater

The transport of Uranium contaminated groundwater to the Columbia River in the hyporheic corridor of the U.S. Department of Energy Hanford 300-Area, Richland, Washington, is influenced by the depth and location of the Hanford-Ringold contact. Ringold Formation sediments have distinct physicochemical properties compared to the Hanford Formation sediments through which groundwater flows. Definition of the spatial variability and the depth to the Hanford-Ringold contact across the site is crucial to improve understanding of contaminant transport between the aquifer and the river. This dissertation focuses on the use of geophysical datasets to build a hydrological framework for understanding groundwater-surface water interaction and mixing of Uranium contaminated groundwater with Columbia River.

Geophysical data including resistivity, induced polarization (IP) and streambed temperature were collected in the 300-Area. The first part of this dissertation report on the use of resistivity/IP survey to image spatial distribution of the primary lithologic units controlling flow across the site. The Hanford- Ringold contact is clearly identified from

the sharp contrast in polarizability between the two units. Variation in the elevation of this contact provides evidence of a depression in the Hanford-Ringold contact connecting the aquifer and the river, likely facilitating flow and transport at the site.

Fiber-optic cables were used for distributed temperature sensing (FO-DTS), to monitor real time temperature along the river corridor. It is recognized that groundwater discharge in 300-Area is controlled by fluctuations in the river stage. The second part of this dissertation focuses on time series and time-frequency analysis of FO-DTS and river stage data to better understand the control of river stage on groundwater discharge. Time series analysis of FO-DTS data identified spatial distribution of groundwater discharge zones on the river bed. Time-frequency analysis provides spatial information on the strength of stage-driven discharge of groundwater along the river corridor.

The third part of this dissertation addresses the need for a new approach to extract quantitative information from FO-DTS data while providing an assessment of uncertainty associated with this information. A combination of discriminant analysis and spectral analysis is used to quantitatively map zones of enhanced groundwater discharge while providing measures of classification uncertainty.

ACKNOWLEDGEMENTS

It has been a great privilege to get to spend a number of years in the Department of Earth and Environmental Sciences at the University of Rutgers-Newark. Its members will always remain dear to me.

I am most grateful to my advisor, Dr. Lee D. Slater for allowing me to work on this project and all that I have learned under his supervision. I am grateful for his guidance and for many opportunities that he provided me to broaden my professional experience. This thesis would not have been possible without his help, support and patience, and I owe him my heartfelt appreciation.

I would also like to acknowledge my thesis committee members, Dr. Fred Day-Lewis, Dr. Dimitrios Ntarlagiannis and Dr. Evert Elzinga. Many thanks for the guidance and excellent advice for my research. The recommendations and instructions they have provided have enabled me to finish this thesis effectively. I gratefully acknowledge Professor Andrew Binley of Lancaster University-England for his insightful suggestions, support and learning opportunities.

I would also like to thank all my instructors and teachers. Special thanks go to Dr. Alexander Gates for all the advice and opportunities, and to Dr. Yuan Gao, Dr. Kristina Keating, Dr. Adam Kustka and Professor Andreas Vassiliou. To Ms. Liz Morrin, thank you for your tremendous help. Nothing would be possible in the department without you.

This research was supported by the U.S. Department of Energy under grant number DOE - DE - FG02 - 08ER64561. I have also benefited from fruitful discussions and field interactions with Andy Ward, Jason Greenwood, Christopher Strickland, and Carole Johnson. Many thanks to Roelof Versteeg and Timothy Johnson for all their input in this research.

I am indebted to my fellow graduate students for providing enjoyable environment to learn and grow. It has been a pleasure working with you. I am especially grateful to Chi Zhang, Jessica Halsey, Sweeta Chauhan, Dawn Semple and Judy Robinson. Special thanks to Michael Kalczynski, James Nolan, Andrew Parsekian, Jeff Heenan, Yves Persoanna, Samuel Falzone, Neil Terry and Ashley New. Many thanks to Mehrez El-wasif for S-transform codes.

Finally I would like to express deep appreciation to my family and friends who provided so much needed support and encouragement throughout my education journey. To Allan Koyo, your friendship is indescribable, I can only say thank you. It is difficult to overstate my gratitude to my parents, Margreth and Abel Mwakanyamale. This would not have been possible without their constant support and encouragement. Thank you for believing in me. Mom, dad, this one is for you!

Table of Contents

| | |
|--|-----------|
| CHAPTER 1. Introduction | 1 |
| 1.1 Background | 1 |
| 1.2 Problem | 2 |
| 1.3 Study Site | 4 |
| 1.4 Objectives | 6 |
| 1.5 Scope of the Dissertation | 7 |
| CHAPTER 2. Methods | 10 |
| 2.1 Electrical Methods | 10 |
| 2.1.1 Resistivity | 10 |
| 2.1.2 Induced Polarization | 12 |
| 2.1.3 Petrophysical Properties | 14 |
| 2.1.4 Inverse Methods | 16 |
| 2.2 Fiber Optic Distributed Temperature Sensing | 17 |
| 2.2.1 Heat as Groundwater Tracer | 19 |
| CHAPTER 3. Lithologic Imaging Using Complex Conductivity: Lessons Learned from the Hanford 300 Area | 22 |
| 3.1 Introduction | 23 |
| 3.2 Study Site | 25 |
| 3.3 Electrical Measurements | 30 |
| 3.4 Electrical Properties | 32 |
| 3.5 Methods | 33 |
| 3.5.1 Field surveys | 34 |

| | |
|---|-----------|
| 3.5.2 <i>Laboratory calibrations</i> | 38 |
| 3.5.3 <i>Error analysis</i> | 39 |
| 3.5.4 <i>Inversion of field data</i> | 44 |
| 3.6 Field Results | 45 |
| 3.7 Synthetic Data | 51 |
| 3.8 Synthetic inversion results | 53 |
| 3.9 Discussion | 54 |
| 3.9.1 <i>Implications for lithological characterization of the 300 Area</i> | 54 |
| 3.9.2 <i>Implications for complex conductivity field surveys</i> | 58 |
| 3.10 Conclusions | 60 |
| CHAPTER 4. Spatially variable stage-driven groundwater-surface water interaction inferred from time-frequency analysis of distributed temperature sensing data | 62 |
| 4.1 Introduction | 63 |
| 4.2 Field Site | 64 |
| 4.3 Methods | 66 |
| 4.3.1 <i>Fiber Optic Distributed Temperature Sensing</i> | 66 |
| 4.3.2 <i>S-transform</i> | 66 |
| 4.3.3 <i>Field data acquisition</i> | 68 |
| 4.3.4 <i>Time series and time-frequency analysis</i> | 68 |
| 4.4 Results | 69 |
| 4.5 Discussion | 75 |
| 4.6 Conclusions | 78 |

| | |
|--|------------|
| CHAPTER 5. Statistical classification of spatial variation of groundwater discharge from DTS data | 79 |
| 5.1 Introduction | 80 |
| 5.2 Study Site | 82 |
| 5.3 Methods | 84 |
| 5.3.1 <i>Fiber Optic Distributed Temperature Sensing</i> | 84 |
| 5.3.2 <i>Spectral Analysis</i> | 85 |
| 5.3.3 <i>Discriminant Analysis</i> | 86 |
| 5.3.4 <i>Data Acquisition</i> | 87 |
| 5.3.5 <i>Data Analysis</i> | 88 |
| 5.4 Results | 89 |
| 5.5 Discussion and Conclusions | 94 |
| CHAPTER 6. Conclusion | 96 |
| 6.1 General Conclusion | 96 |
| 6.2 Implication for 300-Area Hydrological Model | 98 |
| 6.3 Recommendations | 99 |
| REFERENCES | 101 |
| APPENDICES | 111 |
| Appendix A. Supplemental material for Chapter 3 | 111 |
| Appendix B. Supplemental material for Chapter 4 | 116 |
| Appendix C. Supplemental material for Chapter 5 | 119 |
| CURRICULUM VITAE | 123 |

List of Illustrations

| | |
|---|----|
| Figure 1.1. Hyporheic Zone | 3 |
| Figure 1.2. River stage fluctuation | 3 |
| Figure 1.3. Map of the study site | 4 |
| Figure 1.4. Geologic cross section | 5 |
| Figure 2.1. Common electrode configurations | 12 |
| Figure 2.2. Raman and Brillouin backscattering | 18 |
| Figure 2.3. Annual (or diurnal) streambed temperature | 21 |
| Figure 3.1. Map of the study site | 26 |
| Figure 3.2. Hydrogeologic cross section | 28 |
| Figure 3.3. Field Survey setup | 35 |
| Figure 3.4. Decay Curves | 38 |
| Figure 3.5A. Error Models at $\epsilon > 100\%$ | 42 |
| Figure 3.5B. Error Models at $\epsilon > 20\%$ and $\epsilon > 100\%$ | 43 |
| Figure 3.6. Field Inversion Results | 46 |
| Figure 3.7. Comparison of field inversion results between long and short lines | 49 |
| Figure 3.8. Comparison of field inversion results at different error cut-off levels | 50 |
| Figure 3.9. Synthetic Inversion Results | 53 |
| Figure 3.10a. Elevation of the Hanford-Ringold contact | 56 |
| Figure 3.10b. Elevation of the Hanford-Ringold contact and uranium contours | 58 |
| Figure 4.1. Location Study Site and identified groundwater discharge zones | 70 |
| Figure 4.2. Time series analysis of FO-DTS and river stage data | 72 |
| Figure 4.3. Time-Frequency analysis using 1-D S-transform | 74 |
| Figure 4.4. Time-Frequency analysis using 2-D S-transform | 75 |

| | |
|---|----|
| Figure 5.1. Location of the study site, Hanford Formation thickness and streambed temperature | 84 |
| Figure 5.2. FFT and DA results for winter and summer data | 91 |
| Figure 5.3. Map of Hanford Formation thickness, DA and posterior probability | 94 |

CHAPTER 1

1.0 INTRODUCTION

1.1 Background

Groundwater-surface water interactions occurs at the zone beneath and adjacent to the surface water bodies [Lambs, 2004; Alley *et. al.*, 2002; Biksey and Gross, 2001]. The mixing of surface water with groundwater is govern by the position of the surface water bodies relative to the groundwater flow system, the characteristic of the sediments and underlying materials and the climatic setting. Whereas the geologic framework affects the flow paths through which groundwater flows, the type of sediments at the interface between groundwater and surface water can dictate the spatial variability of groundwater discharge to the surface water [Alley *et al.*, 2002].

Interactions between groundwater and surface water occurs in two scenarios; the first scenario is during high river stage and the second is during low river stage. River water infiltrates the river banks during periods of high river stage and mix with the approaching groundwater. Mixing between groundwater and infiltrating river water causes dilution of contaminants potentially present in the groundwater. During periods of low river stage, groundwater discharge from the aquifer appears as riverbank seepage. Riverbank seepage creates the potential for transfer of contaminants potentially present in the groundwater into the river. Consequently, the characterization of groundwater-surface water interactions is crucial to understanding contaminant transport between aquifers and rivers. Such information has a major impact on water quality management and ecological health of groundwater dependent [Keery *et. al.*, 2007].

1.2 Problem

Uranium contamination in the Hanford site 300 Area resulted from underground storage of spent nuclear waste for over forty years, starting on 1943 to 1975. The disposed chemical record includes Uranium (U (VI)), Copper (Cu), Aluminum (Al), Fluorine (F), Nitrate (Ni) and large volumes of acid (HNO₃) and base (NaOH) [Dennison *et. al.*, 1989]. These chemicals were deposited on the North and South side of the 300 Area. The 300 Area is no longer used for nuclear fuel production and large portion has been undergoing environmental cleanup [Patton *et al.*, 2003]. The groundwater under the 300 Area has contaminants from both 300 Area derived materials (primarily uranium) and from the contaminated groundwater plumes from the other Hanford Site's Areas [Patton *et. al.*, 2003]. The highest uranium concentration in groundwater was observed from the early 1950s to the late 1980s.

The contaminated groundwater discharges to the Columbia River through the hyporheic zone (a zone of groundwater-river water interaction) (Figure 1.1) [Peterson and Connelly, 2001; Peterson and Connelly, 2004; Fritz and Arntzen, 2007]. Various efforts have been carried out to prevent any further contamination of the river e.g. removal of highly contaminated sediments, but the concentration of uranium in the groundwater have remained steadily high [Tyler, 1992; Hartman *et. al.*, 2006; Slater *et. al.*, 2010]. The groundwater flow system beneath the 300 Area represents a primary pathway for contaminant movement away from source areas to ultimately discharge into the river. The groundwater flow system is influenced by the frequent fluctuation in the river stage controlled by hydroelectric dam operations.

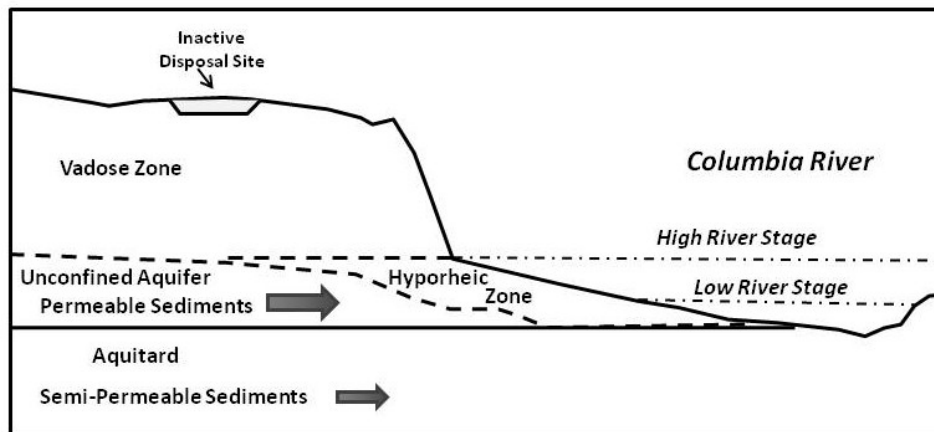


Figure 1.1 Diagram of the hyporheic zone at Hanford 300 Area. Figure modified from *Fritz et al.* [2007].

Hydroelectric dam operations on the Columbia River, upstream of the 300 Area are known to drive complex river stage fluctuations (Figure 1.2), which in turn controls groundwater surface water interaction. *Lindberg and Chou*, [2001] and *Peterson et al.* [2008] noted that, the highest stage levels typically occur during May and June months. Understanding of the hydrological framework of the 300 Area will help to understand the transport of uranium and its impact on the Columbia River.

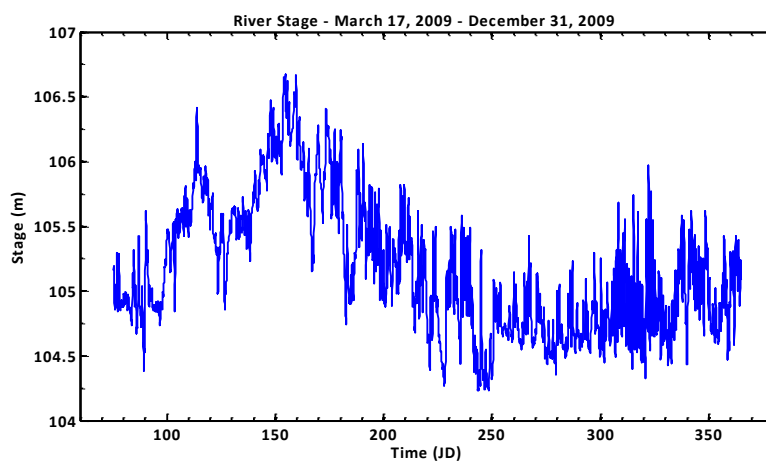


Figure 1.2 Example of the river stage fluctuation in the Columbia River corridor at the 300 Area from March 17, 2009 to December 31, 2009.

1.3 Study Site

The 300 Area is located on the west bank of the Columbia River at the south end of the Hanford Site in Richland area, southeastern Washington State (Figure 1.3). The geology of 300 Area mainly consists of two geological formations; the Hanford Formation and the Ringold Formation (Figure 1.4). Ringold Formation includes sediments that lie immediately above the bedrock, basalt flow. Directly above the Ringold Formation is the Hanford Formation. The two formations differ physically in their lithological properties which controls the hydrological framework of the 300 Area.

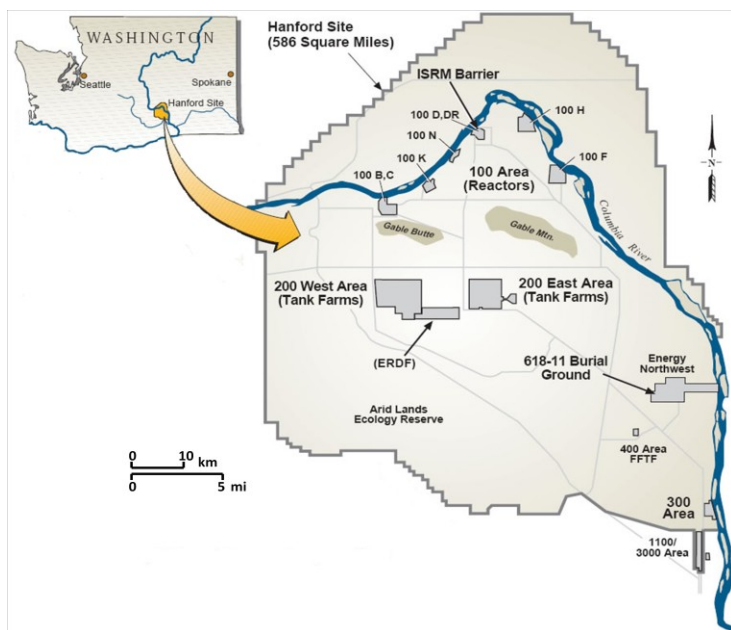


Figure 1.3 Map of Washington State showing the location of the Hanford Site in the southeast Washington. 300 Area is located in the southeastern Hanford site, west of Columbia River.

The lower unit, Ringold Formation is divided into gravel dominated interval (upper) and mud dominated interval (lower) [Kunk *et. al.*, 1993]. The upper unit which has hydraulic conductivity value of ~ 21.36 meters/day [Williams *et al.*, 2007] consists largely of

cemented and compacted quartzitic gravels with mica rich silt and fine sand matrix [Lindberg and Bond, 1979; Kunk et al., 1993; Fritz et al., 2007]. The lower mud unit which has a much lower hydraulic conductivity, forms a confining aquitard consists of silty-clay to silty-sand sediments [Tyler, 1992; Peterson et al., 2008].

The Hanford formation consists mainly of unconsolidated sand and gravel facies that range in thickness from 2 to 6 meters [Peterson and Connelly, 1992; Peterson and Connelly, 2001]. The hydraulic

conductivity of these facies is high at ~100 meters/day [Williams et al., 2007]. The Hanford Formation gravels represents the unconfined aquifer and contains highly permeable buried channels that acts

as flow paths to the contaminated groundwater. These flow paths are believed to be incised into the

Ringold formation. The presence of these paleochannels is postulated to provide a direct connectivity between the aquifer and the Columbia River in the 300 Area and is responsible for the rapid response of groundwater levels to fluctuations in river stage [Lindberg and Bond, 1979].

In the 300 Area, the water table is located near the contact between the Hanford Formation and Ringold Formation. The interface between the Hanford Formation and

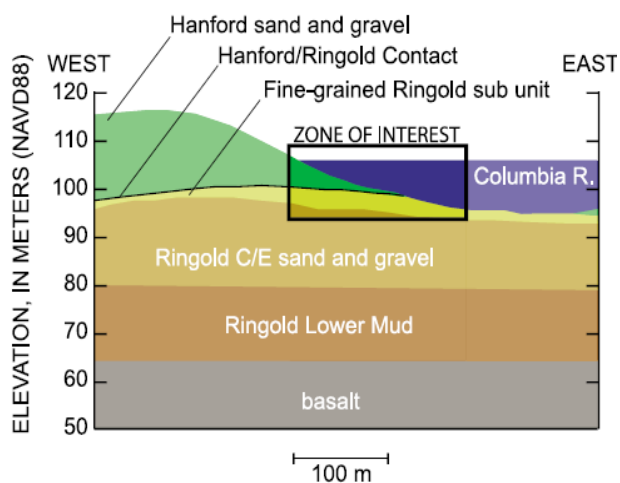


Figure 1.4 Geologic cross section of the 300 Area, showing the Hanford Formation, Ringold Formations and the Hanford - Ringold contact. Figure from Slater et al. [2010].

Ringold Formation (Hanford-Ringold contact) is then a very important hydrogeologic feature [Fritz *et. al.*, 2007] that is known to control the vertical migration of the groundwater. When the river stage raises, river water infiltrate the aquifer inland as far as 400 meters [Peterson *et. al.*, 2008] and the river water displaces or mixes with groundwater [Lindberg and Chou, 2001]. During low river stages, the hydraulic gradient of the water table is reversed and the groundwater flow direction is towards the east-southeast [Lindberg and Chou, 2001] and then discharges to the Columbia River.

1.4 Objectives

Heterogeneity in physical properties (e.g. grain size) of the parent lithology, along with the dynamic, complex hydrologic processes at the water table, pose significant challenges for the design of hydrologic model to simulates groundwater movement. Due to the aforementioned facts, the following hypotheses were created;

1. Variability in the hydrological framework in the 300 Area is caused by the variation in height and spatial location of the Hanford-Ringold contact which controls the transfer of uranium into the river.
2. Paleochannels incised into the Ringold Formation acts as flow path for contaminated groundwater and facilitate the mixing of contaminated groundwater with the river water.
3. Mixing of contaminated groundwater with the river water is largely controlled by fluctuation in the river stage, which is very complex due to daily (e.g. hydroelectric dam operations) and seasonal variation.

The aim of this thesis is to use field scale geophysical methods to test the hypothesis mentioned above, to improve understanding of the 300 Area hydrological frame work and hence improve understanding of groundwater-surface water interaction and mixing of uranium contaminated groundwater with Columbia River water. The specific objectives of this study in response to the hypotheses above are to;

Hypothesis 1

Objective 1: Use integrated geophysical methods to better define the variability in depth and location of the Hanford-Ringold contact in the 300-Area.

Hypothesis 2

Objective 2: Use integrated geophysical methods to identify and map paleochannels connecting the contaminated groundwater to the river corridor.

Hypothesis 3

Objective 3: Use time series and time-frequency analysis to better understand;

- (1) Groundwater discharge in response to river stage fluctuations
- (2) Factors controlling the river stage fluctuations.

1.5 Scope of the Dissertation

This study address the use of geophysical method to achieve the objectives mentioned above. Chapter 2 introduced the basic principles of the two geophysical methods used here, electrical methods (Resistivity and Induced Polarization) and the fiber optic distributed temperature sensing (FO-DTS).

The following chapters, 3, 4 and 5 includes an individual abstract, introduction, methods, results, discussion and conclusions, organized as follows; Chapter 3 addresses objectives 1 and 2. Field scale, 2D time domain resistivity and induced polarization (IP) were data were acquired in the field with the goal of resolving the major hydrogeological framework at the 300 Area by identifying variability of the depth to the Hanford-Ringold contact (H-R contact) and mapping paleochannel across the 300 Area. Exploiting the equivalence between time domain and frequency domain electrical measurements, the time domain measurements collected in the field were converted to complex resistivity measurements (frequency domain; phase, real and imaginary conductivity) for a better interpretation of lithological variability.

Chapter 4 addresses objective 3 by reporting on time series and time-frequency analysis of the FO-DTS and river stage time series. Analysis of the two time series provides spatial information on the strength of stage-driven exchange of uranium contaminated groundwater in response to subsurface heterogeneity. Time series analysis using stage-temperature correlation coefficient was used to obtain strength of the dependence between riverbed temperature and river stage fluctuations in relations to groundwater discharge. Time-frequency analysis of the stage and FO-DTS data identifies the spatial distribution of discharge zones and provided information on the dominant forcing periods of the complex dam operations driving stage fluctuations and hence groundwater-surface water exchange at the 300-Area.

Chapter 5 finalizes on the third objective by exploring a rigorous way to develop a rule for quantitatively predicting the groundwater exchange and non-exchange zones along the Columbia River corridor and quantify uncertainty associated with that prediction. The combination of spectral analysis and discriminant analysis was used on the Hanford Formation thickness and the FO-DTS data to condense the two large datasets and focus on salient features related to groundwater exchange processes. The discriminant analysis function developed in this investigation was able quantitatively map 75% of sites as either groundwater exchange zones or non-exchange zones at 100% confidence level.

Finally, Chapter 6 summarizes the main findings from the previous chapters, and provides the overall conclusions, including contributions of this research to the remediation efforts in the 300 Area. The appendices at the end of this dissertation include supplemental materials (figures and brief discussion) for Chapter 3, Chapter 4 and Chapter 5.

CHAPTER 2

2.0 METHODS

A range of geophysical methods have been applied at the groundwater - surface water interface in an attempt to delineate lithological variation, identify the presence and location of pollutants or to delineate the hyporheic zone. Groundwater and surface water exhibit distinctive physical characteristics [Lambs, 2004] when the two entities combine in the hyporheic zone their characteristics blend and a new gradient is established especially for contaminants. The new gradient is the basis for applied geophysical methods to delineate the hyporheic zone. Different geophysical methods applied in the various environments depend on the physical properties expected to vary e.g. lithological heterogeneity or conductivity due to presence of pollutants. A sharp contrast in physical properties exists between different sediment types found in the 300-Area, allowing the use of geophysical methods to attest to our objectives. Geophysical methods used here include electrical methods and temperature monitoring.

2.1 Electrical Methods

Electrical measurements have been used for decades for characterization of the lithology and hydraulic characteristic of geological structures. The purpose of electrical surveys is to determine the subsurface resistivity distribution, both laterally and vertically, by making measurements on the ground surface [Loke, 1996]. Electrical methods used here include electrical resistivity and induced polarization (IP).

2.1.1 Resistivity

Resistivity (ρ) is a measure of the ability of soil/rocks to conduct or insulate electrical current. Conductivity (σ) is the inverse of resistivity. The fundamental physical law used in resistivity surveys is Ohm's Law (Equation 2.1) that governs the flow of current in the ground. Ground resistivity is measured by inducing a direct current (I) into the ground using a pair of current electrodes and the resulting voltage difference (V) caused by the medium is measured between a pair of potential electrodes (Figure 2.1). The direct current introduced through a pair of electrodes it will penetrate to a depth governed by the current, the electrode separation and the resistivity of the subsurface formation. It will cause a potential difference at points between these electrodes which will be governed by the same factors. Thus, if the distance between current electrodes is increased, this will cause an increasing penetration into the ground which will be expressed at the surface by changes in the potential difference as measured at the potential electrodes [*Ginzburg and Levanon, 1976*].

$$R = \frac{V}{I} (\Omega) \quad (2.1)$$

Where R is the measured transfer resistance. In the subsurface, electrical currents are not confined to a circuit. Considering an electrically uniform rectangular block of cross-sectional area A and length L , the resistivity of that block can then be calculated by;

$$\rho = \frac{V}{I} \times \frac{A}{L} = RK(\Omega m) \quad (2.2)$$

Notably, the resistivity of the material is a function of the geometric factor K (Equation 2.2). The geometric factor is governed by the configuration of the electrodes used in the field. The current and potential electrodes are generally arranged in a linear configuration. The most common configurations include Wenner, Dipole-Dipole, and Schlumberger (Figure 2.1).

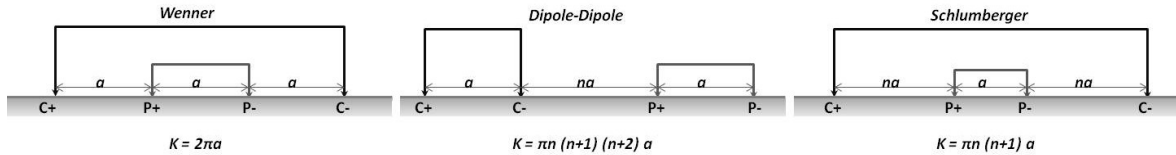


Figure 2.1 Electrode configurations for linear resistivity surveys. Current is delivered through the electrodes C+ and C-, and resulting voltage is measured by electrodes P+ and P-. Figure modified from *Reynolds* [1998].

Each of these electrode configurations has their own advantages and disadvantages, depending on the type of survey to be performed. For a detailed description on electrode configurations see *Dahlin and Loke*, [1998].

The resistivity of a formation depends on its mineralogical composition, porosity and the shape of the pores, the fluid saturation and the ionic concentration of the formation fluid [*Ginzburg and Levanon*, 1976]. Thus for a given formation of fairly constant composition and porosity one can expect a constant resistivity provided the chemical composition of the formation fluid remains constant. Increasing concentrations of ions in the fluid would lower the overall resistivity of the rock. Resistivity generally decreases with increasing porosity. Geoelectrical resistivity techniques are popular and successful in; determination of depth to different lithological contacts, thickness and boundary of an aquifer, determination of interface between saline water and fresh water, porosity of aquifer, water content in aquifer, hydraulic conductivity of aquifer, etc.

2.1.2 Induced Polarization

Induced polarization (IP) is a geophysical phenomenon which measures the rate at which material can store electric charge. This phenomenon has two components, time domain

and frequency domain. In time domain current is applied into the medium for a period, and then it is turned off, what is recorded is the decay of voltage between two potential electrodes after the cut-off of the electrical current. The voltage remaining (v_r) at the beginning of the off-period is measured and compared with the on-period voltage (v_p) [Marshall and Madden, 1959]. The measured voltage integrated in the time window (t_1 and t_2) is characterized by the chargeability, M , (Equation 2.3);

$$M = \frac{I}{\Delta t} \frac{1}{V_p} \int_{t_1}^{t_2} V_r dt \quad (2.3)$$

When the measurements are made in frequency domain, the phase shift (ϕ) between injected current and voltage response is measured. The phase shift is usually small, in the order of one degree or less [Marshall and Madden, 1959]. The combined conduction and polarization properties of earth materials measured with resistivity and IP can be conveniently expressed by an effective complex electrical conductivity (σ^*);

$$\sigma^* = \sigma' + i\sigma'' \quad (2.4),$$

where $i = \sqrt{-1}$. The real conductivity (σ') represents energy loss as current flow in phase with the applied electric field whereas the imaginary conductivity (σ'') represents energy stored as displacement of current 90° out of phase with the applied field. The energy storage is assumed to be associated only with the interfacial polarization at low frequencies. The measured parameters, $|\sigma|$ and ϕ , recorded with a frequency domain IP instrument are related to σ' and σ'' as follows;

$$|\sigma| = \sqrt{(\sigma'^2 + \sigma''^2)} \quad (2.5),$$

$$\phi = \tan^{-1} \left[\frac{\sigma''}{\sigma'} \right] \approx \left[\frac{\sigma''}{\sigma'} \right] \quad (2.6).$$

The phase shift between injected current and voltage response measured in the field with a frequency domain IP instrument is therefore a measure of the ratio of polarization to conduction [*Lesmes and Frye, 2001; Ulrich and Slater, 2004*] (Equation 2.6). It should be noted that the approximation in equation 2.6 only holds in nonmetallic environments where polarization effects are small e.g. $\phi < 100$ mrad [*Vinegar and Waxman, 1984; Slater and Lesmes, 2002; Kemna et al., 2004; Ulrich and Slater, 2004*].

Normalized IP parameters are defined by multiplying the field IP parameters by the measured conductivity (or dividing by resistivity) and provide a direct measure of surface polarization [*Lesmes and Frye, 2001; Slater and Lesmes, 2002*]. For example, multiplying ϕ measured with a frequency domain instrument by $|\sigma|$ approximately yields σ'' (Equation 2.7);

$$\sigma'' = |\sigma| \sin \phi \approx |\sigma| \phi \quad (2.7).$$

The approximation in Equation 2.7 again holds for small phase angles only. Similarly, multiplying M measured with a time domain instrument by $|\sigma|$ yields a normalized chargeability (M_n) [*Lesmes and Frye, 2001*].

2.1.3 Petrophysical Properties

In nonmetallic environments, electric charge is transferred by two mechanisms; electrolytic conduction (σ_{ele}) and surface conduction (σ_{surf}). Electrolytic conduction involves ionic transport of charge through the fluid in the interconnected pore space, while surface conduction occurs within an ionic double layer at the grain–fluid interface. Electrolytic conduction, a purely real term, is controlled by water saturation, porosity and

ionic concentration of the pore fluid. Surface conduction, a complex, frequency-dependent term is largely determined by specific surface area and grain/pore distribution of the material. Fluid chemistry and mineralogy control the surface charge density and the surface ionic mobility and typically exert a second order control on surface conduction [Lesmes and Frye, 2001; Slater and Lesmes, 2002; Ulrich and Slater, 2004]. It is often assumed that the electrolytic and surface conduction paths add in parallel [Marshall and Madden, 1959; Vinegar and Waxman, 1984],

$$\sigma^* = \sigma_{ele} + \sigma_{surf}^* \quad (2.8)$$

Using this model, the real component of the measured complex conductivity is a function of both electrolytic and surface conductivity mechanisms whereas the imaginary component of the conductivity is only a function of the surface conductivity,

$$\sigma' = \sigma_{ele} + \sigma'_{surf} \quad (2.9),$$

$$\sigma'' = \sigma''_{surf} \quad (2.10).$$

Combining Equation 2.6, 2.9 and 2.10, phase response can be estimated by;

$$\phi = \frac{\sigma''_{surf}}{\sigma_{ele} + \sigma'_{surf}} \quad (2.11).$$

Equation 2.11 shows that the phase response is controlled by both electrolytic conduction and the real and imaginary components of surface conduction.

The strong near linear relationship between IP parameters and structural properties (e.g. specific surface area, clay concentration), coupled with the relatively low sensitivity of IP measurements to fluid chemistry, provides an opportunity to reduce ambiguity in the interpretation of conductivity imaging surveys [Slater and Lesmes, 2002]. The combined acquisition of IP and conductivity measurements can help separate the electrical response

due to pore fluid properties from that due to lithology [Kemna *et al.*, 2004; Slater *et al.*, 2010; Slater and Lesmes, 2002]. Weller *et al.* [2010] recently showed that a strong linear relationship between surface area normalized to the pore volume (S_{por}) and normalized IP parameters (imaginary conductivity ($\sigma'' = c_p (S_{por})$ subscript p denotes single frequency IP) and normalized chargeability ($M_n = c_s (S_{por})$ subscript s denotes spectral IP dataset)) can fit a wide range of sandstone and unconsolidated sediments. They tentatively suggested that this empirical relationship is the IP equivalent of the classic *Archie's Law* [1942] ($\sigma'_{bulk} = \sigma_w \phi^m S^n$), σ'_{bulk} is a bulk conduction term, σ_w is the solution conductivity, ϕ is the porosity, S is the saturation, and m and n are the cementation and saturation exponents, respectively) for relating resistivity to porosity [Weller *et al.*, 2010]. S_{por} is related to the size of the interconnected, polarizable surface of a porous medium and is therefore sensed by IP measurements (see for review, [Slater, 2007]).

2.1.4 Inverse Methods

The calculated ρ (or σ) and M/ϕ value are not the true properties of the subsurface, but apparent values that are a property of a homogeneous ground that will give the same value for the same electrode arrangement. Data processing is required to transform measured data to a 1-D, 2-D, or 3-D spatial distribution of electrical properties [Reynolds, 1998; Binley and Kemna, 2005]. To determine the true values of the distribution of subsurface electrical properties (model), inverse methods may be applied to apparent measurements (data). The purpose of the inverse method is to find a model (m) which reproduces the measured data (d) to the specified level of uncertainty [Binley and Kemna, 2005]. However, the use of inverse methods produce no unique solution to the model

[*Binley and Kemna, 2005*], there exists a range of different models that produce the same response. Constraint needs to be applied to the inversion process during model search to obtain a somewhat unique solution with practical relevance to the data [*Binley and Kemna, 2005*]. This is accomplished by formulating the inverse method as a regularized optimization problem.

The 2D σ^* inversion algorithm (described in detail by *Binley and Kemna, [2005]*) uses a Gauss Newton method to iteratively finds the optimum value of a regularization parameter (λ), that minimizes an objective function (Ψ^*) composed of a data misfit term and a model stabilization term,

$$\psi^* = \|W_\varepsilon (d - f(m))\|^2 + \lambda \|W_m(m - m_{ref})\|^2 \quad (2.12)$$

where W_ε represent a data weighting matrix associated with data individual errors, f is a vector describing the finite element forward solution for model vector m . The model stabilization term consists of a reference model m_{ref} and W_m which is a smoothness constraint representing the model weighting matrix [*Binley and Kemna, 2005*]. The iteration process stops when an acceptable data misfit value is reached [*Kemna, 2000*] and/or the maximum number of iterations is reached. The tradeoff between influence of data misfit and model objective function in the inversion process, is controlled by λ [*Binley and Kemna, 2005*]. At each iteration step, the trial value of λ is updated successfully until the desired data misfit is achieved [*Day-Lewis et al., 2005*].

2.2 Fiber Optic Distributed Temperature Sensing

Difference in temperature signatures between groundwater and surface water can be used in studying groundwater-surface interaction. Surface water temperature is known to follow two cycles; seasonal cycle and diurnal cycle [Sinokrat and Stefan, 1993; Constantz *et. al.*, 1994]. Diurnal temperature variations are directly related to weather parameters such as air temperature, solar radiation, humidity, wind speed, rainfall cloud covers etc. This is shown by periodic change in surface temperature i.e. hot in the day and cool at night. Season cycle depends on the summer and winter conditions. On the other hand, groundwater temperature is more or less constant all year round [Schmidt *et. al.*, 2005]. In general groundwater is cooler than surface water in the summer, and is proved to be warmer than surface water in the winter season.

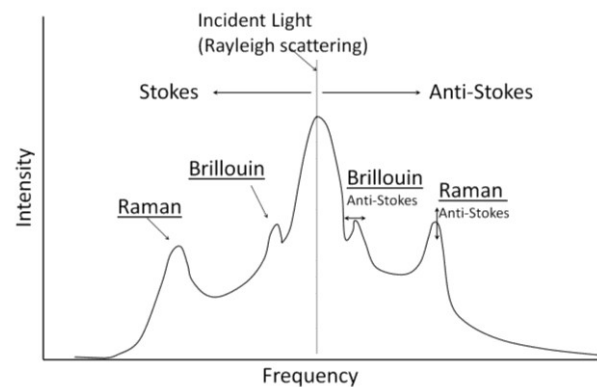


Figure 2.2 Diagram showing Raman and Brillouin scattered signals with Stokes and anti-Stokes frequency. Figure modified from Selker *et.al.* [2006a].

Recent development in using riverbed temperature to study exchange between groundwater and surface water, involves the use of fiber optic distributed temperature sensing (FO-DTS) system. The use of fiber optic cable allows continuous measurements of temperature in both time and space at very high spatial and temporal resolution [Selker *et al.*, 2006a; Lowry *et al.*, 2007; Henderson *et al.*, 2009]. FO-DTS rely on scattering of a laser light to determine temperature along a fiber optic cable [Selker *et al.*, 2006a; Lowry *et al.*, 2007]. A laser pulse is sent down the length of the fiber optic cable where

variations in temperature cause differences in backscatter. The reflected energy will be scattered back with the wavelength less than original (anti-Stokes) or with the wavelength higher than the original (Stokes) due to (1) density change in the fiber caused by electromagnetic forces from the passage of the light (Brillouin Scattering) (2) loss/gain of energy exchange with electrons (Raman Scattering) [Selker *et al.*, 2006a, 2006b] (Figure 2.3). Variation in the intensity of the anti-Stokes wavelength is a function of temperature whereas, variation in intensity of the Stokes wavelength is not affected by temperature [Lowry *et al.*, 2007]. The ratio of the two wavelengths (i.e. anti-Stokes to Stokes ratio) provides a quantity independent of light intensity but only depends on the temperature of the fiber at that location [Tyler *et al.*, 2008]. By timing the two-way travel time of a laser pulse, the distance from where the light was reflected can be calculated [Selker *et al.*, 2006b; Tyler *et al.*, 2008].

Assuming that the distributed temperature sensing (DTS) unit is protected from changes in temperature, a resolution approaching 0.01°C is possible with long integration times [Selker *et al.*, 2006a; Tyler *et al.*, 2008]. A spatial resolution of 1 m with lengths of up to thousands of meters is also possible with temporal resolution of fractions of a minute along standard fiber-optic cables [Selker *et al.*, 2006a]. In steady state temperature conditions in the surface water and groundwater, the temperature distribution measured by the FO-DTS system will help provide both qualitative and quantitative estimation of the interaction between groundwater and surface water.

2.2.1 Heat as Groundwater Tracer

Mixing of groundwater and surface water plays an important role in hydrologic processes such as water-level fluctuations, river/stream discharge, transfer of contaminants and temperature regulation [*Hatch et al.*, 2006; *Anibas et al.*, 2009]. Groundwater acts as a heat source or sink to the surface water depending on the season of the year, whereby heat is exchanged between the aquifer and the land surface. Heat exchanges between rivers and shallow groundwater systems also play a key role in controlling temperatures in the underlying sediments [*Stonestrom and Constantz*, 2003]. As a result, analyses of subsurface temperature patterns provide information about surface-water/ground-water interactions.

The natural contrasts in temperature between groundwater and surface water provide opportunities to use temperature to obtain both quantitative and qualitative information on groundwater-surface water exchange. Groundwater exhibits relatively constant temperature compared to surface water, e.g. stream temperatures varies annually on a range between 0° C and 25° C [*Constantz et al.*, 1994] whereas groundwater commonly exceeds the mean annual air temperature of the locality by 2 to 3 degrees. Monitoring of riverbed temperatures provides information on water movement (water flux) into and out of the river. *Stonestrom and Constantz* [2003] shows a hypothetical streambed temperature profile (Figure 2.3) for a losing stream (downward water flux) versus a gaining stream (upward water flux) over an annual or daily thermal cycle. They reported that, for downward water movement, the temperature change is greater because the downward-moving water has been heated and cooled at the land surface. On the contrary, the penetration of temperature changes is less for upward water movement because the upward-

moving groundwater comes from depths that are buffered from temperature fluctuations at the land surface. By measuring streambed temperature in an environment with significant differences in groundwater and surface water temperature, the intensity of temperature signals can be used as indicator of exchange and flow directions [Anderson, 2005; Keery *et al.*, 2007; Anibas *et al.*, 2009; Hatch *et al.*, 2010; Krause *et al.*, 2012].

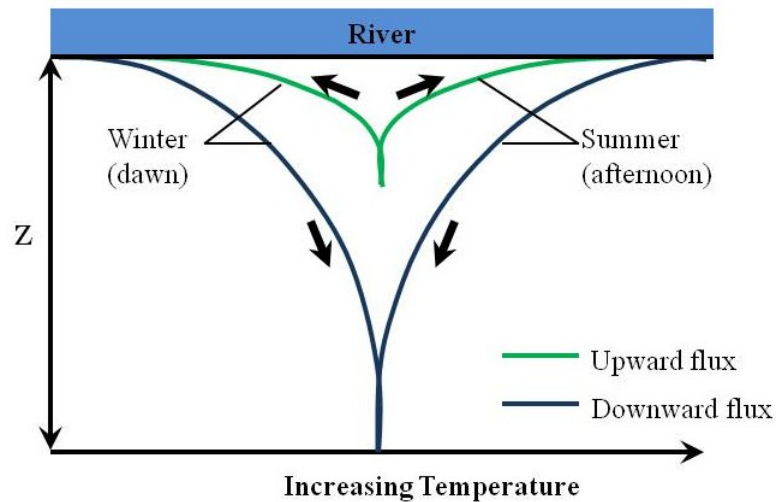


Figure 2.3 Variation of sediment temperature with depth, Z , for gaining (green lines) and losing conditions (blue lines), for daily or annual cycles. The depth at which temperature becomes constant depends on the upward or downward flow of water through the sediments.

CHAPTER 3

3.0 Lithologic Imaging Using Complex Conductivity: Lessons Learned from the Hanford 300 Area¹

Abstract

Field-scale lithologic applications of complex conductivity (σ^*) imaging have been hindered by the challenges of (1) acquiring reliable induced polarization (IP) measurements and (2) obtaining reliable σ^* images from the measurements. A series of 2D time domain resistivity/IP surveys were performed at the Hanford 300 Area (Richland, WA) where the challenge was to image the spatial distribution of two lithologic units that control the exchange between groundwater and surface water of the Columbia River. Exploiting the equivalence between time domain and frequency domain measurements of polarization, a 2D σ^* inversion (real conductivity (σ'), imaginary conductivity (σ'') and phase angle (ϕ)) was utilized to image the spatial distribution of σ^* across the site. Synthetic studies were carried out to investigate the effects of noise on the resolution of σ^* images and to add confidence on the interpretation of possible paleochannels observed in the field datasets. The synthetic studies show that, with increasing representative noise levels, degradation of the resolution of lithologic structures in the parameters most controlled by the IP measurements (ϕ and σ'') is significantly greater than degradation of resolution of σ' images.

¹This work has been published should be cited as: Mwakanyamale, K., L. Slater, A. Binley and D. Ntarlagiannis, (2012), Lithologic Imaging Using Complex Conductivity: Lessons Learned from the Hanford 300 Area, *Geophysics*, 77 (6), P. 1–13, 10.1190/GEO2011-0407.1.

However, the acquisition of IP measurements, and the analysis of changes in both σ' and σ'' constrains the lithological interpretation of the geoelectrical dataset due to the strong dependency of σ'' on lithological properties. A threshold based on σ'' measurements from cores at the site was used to estimate the elevation of the contact between the two key units, which is consistent with boreholes at the site. Variation in the elevation of this contact provides evidence of a depression in the Hanford-Ringold contact connecting the aquifer and the Columbia River; this depression likely represents a paleochannel regulating flow and transport at the site.

3.1 Introduction

Electrical resistivity methods have been extensively used for imaging lithologic variations [Archie, 1942; Waxman and Smits, 1968; Waxman and Thomas, 1974; Jackson et al., 1978; Klein and Sill, 1982]. However, the interpretation of bulk electrical conductivity ($|\sigma|$) obtained from resistivity datasets is inherently uncertain in the absence of other site data. For example, high bulk conductivity may result from enhanced surface conduction associated with large surface area (e.g. due to high clay content), or from enhanced electrolytic conduction due to high water saturation or high ionic concentration of the pore fluid. The strong near linear relationship between parameters determined from Induced Polarization (IP) measurements and structural properties (e.g. specific surface area, clay concentration), coupled with the relatively low sensitivity of these parameters to fluid chemistry, provides an opportunity to reduce ambiguity in the interpretation of conductivity imaging surveys [Slater and Lesmes, 2002]. The additional acquisition of an IP measurement can help separate the electrical response due to pore

fluid properties from that due to lithology [Börner *et al.*, 1996; Kemna *et al.*, 2004; Slater *et al.*, 2010; Slater and Lesmes, 2002], although such discrimination of conduction mechanisms may be limited in high conductivity soils (e.g. high salinity or high clay content) when the signal to noise ratio (SNR) of the IP measurement is low. However, IP is still considered an emerging geophysical technology in environmental applications and it remains relatively infrequently applied in the field for lithological investigations. The following factors likely contribute to the underutilization of the field-scale IP method: (1) acquisition of reliable IP data is more difficult and time consuming relative to resistivity data alone; (2) 2D and 3D inversion of IP datasets is less routine; (3) noise levels for IP measurements are generally higher than for resistivity measurements, such that the resolution of images of IP parameters is degraded relative to the resolution of resistivity images.

Laboratory-scale measurements conclusively illustrate the strong dependence of IP parameters on grain size distribution and associated pore normalized specific surface area [e.g. Lesmes and Frye, 2001, Slater *et al.*, 2006]. Most of these studies have examined the relationship between normalized IP parameters (imaginary conductivity (σ'') and normalized chargeability (M_n) will be used here) and surface area, as well as grain or pore size distribution [e.g. Lesmes and Frye, 2001; Slater and Lesmes, 2002; Slater *et al.*, 2006; Weller *et al.*, 2010]. Similar to σ'' , M_n ($M_n = M * |\sigma|$, where M is the measured chargeability) computed using time-domain IP measurements is largely controlled by the surface area and is only weakly dependent on fluid chemistry [Slater and Lesmes, 2002]. Weller *et al.* [2010] recently showed that a strong linear relationship between the

normalized IP parameters (σ'' and M_n) and surface area normalized to the pore volume (S_{por}) can fit a wide range of sandstone and unconsolidated sediments. They tentatively suggested that this empirical relationship is the IP equivalent of the classic *Archie's Law* for relating resistivity to porosity. Note that S_{por} is often closely associated with cation exchange capacity (CEC) [Vinegar and Waxman, 1984; Lesmes and Friedman, 2005].

Here we show how analyzing complex conductivity (σ^*) variations obtainable from field-scale IP measurements can be used to reduce ambiguity in the interpretation of lithology relative to obtaining only $|\sigma|$ (i.e. the magnitude of the complex conductivity) with a resistivity survey. We assess noise levels and show that resolution of structure in the real part of the conductivity (σ') (and $|\sigma|$) images will be better than structure resolved in the σ'' images due to the noise inherent in IP measurements. However, we show how determination of σ^* images resolves the major hydrogeological framework with confidence at a site where lithology is believed to exert a strong control on the discharge of uranium contaminated groundwater into river water. This confidence would not exist using a conventional resistivity survey alone.

3.2 Study Site

The 300 Area is located on the west bank of the Columbia River at the south end of the Hanford Site in Richland, southeastern Washington state (Figure 3.1). Uranium contamination in groundwater at the 300 Area resulted from underground storage of spent nuclear waste from 1943 to 1975. The contaminated groundwater discharges to the Columbia River through a zone of surface water-groundwater interaction beneath and

adjacent to the river [Peterson and Connelly, 2001; Peterson and Connelly, 2004; Fritz and Arntzen, 2007]. The Hanford 300 Integrated Field Research Challenge (IFRC) site has been designated to study field-scale contaminant mass transfer processes [Ma *et al.*, 2011], and to investigate effective remediation strategies that could protect Columbia River water quality. Seasonal and diurnal fluctuations of the stage on the Columbia River are known to affect the groundwater levels at the IFRC site. The water table elevation ranges between 107.3 m to 104.3 m beneath the IFRC site in response to these stage fluctuations [Bjornstad *et al.*, 2009].

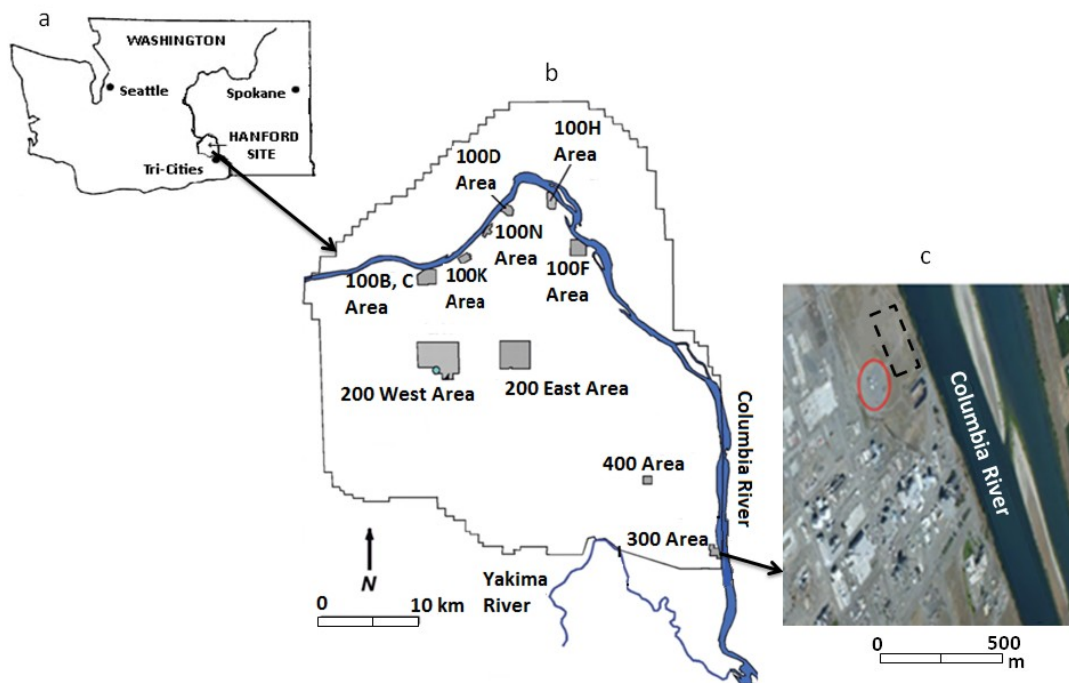


Figure 3.1 (a) Map of Washington State and location of Hanford site. (b) Location of the 300 Area in the south eastern corner of the Hanford site (c) 300 Area with IFRC site (red circle) and the surveyed area (black dashed square) on the northern side of the 300 Area (see Figure 3.3).

Understanding how lithologic variability interacts with river stage variations to regulate exchange between contaminated groundwater and river water is a major scientific

challenge at this site. Mixing of Columbia River water with groundwater is known to change the chemical composition of water sampled in the monitoring wells around the IFRC area [Williams *et al.*, 2007]. Specific conductance of samples suggests that the groundwater-to-river water dilution ratio changes very quickly in response to changes in river stage [Fritz *et al.*, 2007]. Columbia River water has a specific conductance ranging from 120 -150 $\mu\text{S}/\text{cm}$ while groundwater in the 300 Area has a specific conductance ranging from 400 - 500 $\mu\text{S}/\text{cm}$ [Lindberg and Chou, 2001]. Increases in river stage are well documented to cause decreases in specific conductance of groundwater [Lindberg and Chou, 2001; Fritz *et al.*, 2007]. In fact, specific conductance was found to decrease by as much as 150 $\mu\text{S}/\text{cm}$ at high river stage, suggesting complete groundwater displacement by the river water. Specific conductance changes were found to be location specific and to vary with distance, inland from the river corridor as well as with depth between the unconfined aquifer and the confined aquifer [Lindberg and Chou, 2001; Fritz *et al.*, 2007]. A very strong correlation between the specific conductance and uranium concentration has also been reported by Fritz *et al.*, [2007].

The geology of the 300 Area mainly consists of two formations (Figure 3.2): (1) the upper, Hanford Formation hosting the unconfined aquifer in which groundwater flows; (2) the underlying, semi-confining Ringold Formation. The interface between the permeable Hanford Formation and the relatively impermeable Ringold Formation is a critical hydrogeological contact [Fritz *et al.*, 2007] controlling the vertical flow and transport of contaminated groundwater into the Columbia River at the 300 Area [Lindberg and Bond, 1979; Fritz and Arntzen, 2007; Slater *et al.*, 2010]. Identifying

spatial variability in the elevation of this interface across the site is therefore crucial to improve modeling of groundwater flow and transport of uranium from the aquifer towards the river.

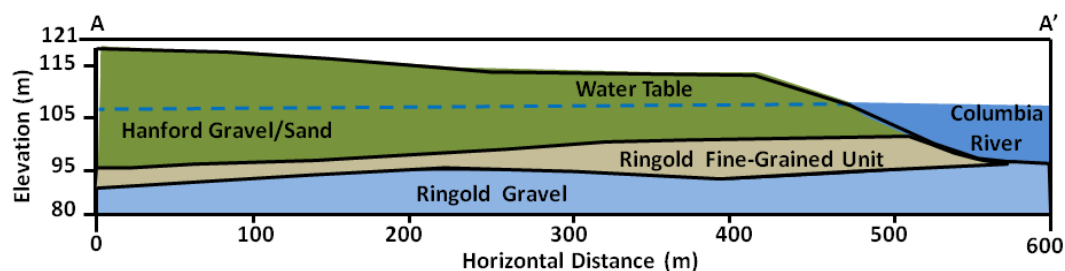


Figure 3.2 Hydrogeologic cross section across the 300 Area intersecting the IFRC well field, our survey profiles and the Columbia River. See Figure 3.3 below for the location of the cross section. The cross section is modified from *Ma et al.* [2011].

The Ringold Formation is mainly divided into gravel dominated (upper) and mud dominated (lower) units [*Newcomb*, 1958]. The upper unit has an average hydraulic conductivity of ≈ 21 meters/day [*Williams et al.*, 2007] and consists largely of cemented and compacted quartzitic gravels embedded within a mica rich silt and fine sand matrix [*Lindberg and Bond*, 1979; *Kunk and Narbutovskih*, 1993; *Fritz et al.*, 2007]. Overlying the Ringold gravel dominated layer is a fine-grained subunit of the Ringold Formation, up to 3.7 m thick within the IFRC [*Bjornstad et al.* 2009] (Figure 3.2). This fine grained unit represents a discontinuous layer as it is locally absent or overlain by the Ringold gravel dominated sediments away from the IFRC site [*Bjornstad et al.* 2009]. The lower mud unit, with a hydraulic conductivity of ≈ 0.2 meters/day [*Williams et al.*, 2007], consists of silty-clay to silty-sand sediments and forms a confining aquitard [*Tyler*, 1992; *Peterson et al.*, 2008]. Geophysical data suggest that this unit thickens to the south, whilst thinning towards the north and west of the 300 Area [*Kunk and Narbutovskih*, 1993]. Cross-sections through the 300 Area based on borehole information from *Bjornstad et al.*

[2009], suggest the contact between the upper (gravel dominated) and lower (mud dominated) Ringold Formation is at an elevation of ~71 m. The reported CEC of the upper and lower Ringold Formation varies from 1-3 meq/100g and 13 – 16 meq/100 g, respectively [Serne *et al.*, 2002].

The overlying Hanford Formation is primarily made up of flood deposits and contains permeable paleochannels that may serve as preferential flow paths for contaminated groundwater, locally facilitating mixing of contaminated groundwater with the river water. These paleochannels, first reported by *Lindberg and Bond*, [1979] are believed to be locally incised below the regional Hanford-Ringold contact. The Hanford Formation consists of pebble to boulder sized basalts gravels and fine to coarse grained sand [Kunk and Narbutovskih, 1993; Fritz *et al.*, 2007; Peterson *et al.*, 2008], with a hydraulic conductivity of ≈ 100 meters/day [Williams *et al.*, 2007] and CEC of ~ 4 meq/100 g [Zachara *et al.*, 2007].

Kunk and Narbutovskih, [1993] used ground penetrating radar and seismic reflection surveys in an attempt to map the presence of paleochannels at this site. Although they did not locate the channel reported by *Lindberg and Bond* [1979], they did identify numerous suspected shallow paleochannels towards the western side of the 300 Area. However, their surveys did not extend to the zone of groundwater-surface water exchange close to the river, so the postulated enhanced connectivity between river water and groundwater due to paleochannels remained uncertain.

In a recent geophysical study, *Slater et al.*, [2010] used M_n [*Slater and Lesmes*, 2002] as a lithological indicator to estimate the depth to the contact between the Hanford and Ringold Formations along the Columbia River corridor. They also reported on fiber-optic distributed temperature sensor (FO-DTS) monitoring results used to improve the understanding of surface water and groundwater interaction at this site. Using the FO-DTS, *Slater et al.* [2010] identified zones of focused groundwater discharge concentrated at locations along the river where the Hanford-Ringold (H-R) contact was predicted to be locally deeper in the electrical images. The waterborne electrical imaging along the river corridor demonstrated that the Hanford and Ringold Formations can be discriminated with IP measurements due to the large lithologic (i.e. surface area, grain size) contrast between the units.

3.3 Electrical Measurements

Conductivity, σ (resistivity (ρ) = $1/\sigma$), is a measure of the ability of a material to conduct electrical current; induced polarization additionally measures the strength of electric charge storage in the electrical double layer forming at a mineral-fluid interface in porous media. Induced polarization measurements can be made in the time or frequency domain.

In the time domain used here, the chargeability (M) is typically calculated as,

$$M = \frac{I}{\Delta t} \frac{I}{V_p} \int_{t_1}^{t_2} V_r dt \quad (3.1)$$

where V_r is the residual voltage defined between times t_1 and t_2 after current shut off, and V_p is the voltage measured during current application. A frequency domain instrument measures the phase shift (ϕ) between induced voltage waveforms and the applied current.

As described by *Olhoeft* [1985], the combined conduction and polarization properties of earth materials measured with resistivity and IP can be conveniently expressed by an effective complex electrical conductivity (σ^*);

$$\sigma^* = \sigma' + i\sigma'' \quad (3.2)$$

where $i = \sqrt{-1}$. The real conductivity (σ') represents energy loss as current flow in phase with the applied electric field whereas the imaginary conductivity (σ'') represents energy stored as displacement of current 90° out of phase with the applied field. The energy storage is assumed to be associated only with the interfacial polarization at low frequencies. The measured parameters, $|\sigma|$ and ϕ , recorded with a frequency domain IP instrument are related to σ' and σ'' as follows;

$$|\sigma| = \sqrt{(\sigma'^2 + \sigma''^2)} \quad (3.3)$$

$$\phi = \tan^{-1} \left[\frac{\sigma''}{\sigma'} \right] \approx \left[\frac{\sigma''}{\sigma'} \right] \quad (3.4)$$

It should be noted that the approximation equation 3.4 only holds in nonmetallic environments where polarization effects are small e.g. $\phi < 100$ mrad [*Vinegar and Waxman*, 1984; *Slater and Lesmes*, 2002; *Kemna et al.*, 2004; *Ulrich and Slater*, 2004]. Note that a conventional resistivity survey only provides $|\sigma|$ and does not allow the σ^* to be computed.

Normalized IP parameters are defined by multiplying the field IP parameters by $|\sigma|$ and provide a direct measure of surface polarization [*Lesmes and Frye*, 2001; *Slater and Lesmes*, 2002]. For example, multiplying ϕ measured with a frequency domain instrument by $|\sigma|$ approximately yields σ'' ;

$$\sigma'' = |\sigma| \sin \phi \approx |\sigma| \phi \quad (3.5)$$

The approximation in equation 3.5 again holds for small phase angles only. Similarly, multiplying M measured with a time domain instrument by $|\sigma|$ yields a normalized chargeability (M_n) [Lesmes and Frye, 2001].

For a linear system, the time and frequency domains are related to one another, e.g. through Fourier transformation, and frequency domain information can in theory be derived from time domain data [Marshall and Madden, 1959; Shuey and Johnson, 1973; de Lima and Niwas, 2000]. A linear proportionality between phase and chargeability can be established both theoretically and experimentally [Marshall and Madden, 1959; Seigel, 1959; Collett and Katsube, 1973; Shuey and Johnson, 1973; VanVoorhis et al., 1973; Vinegar and Waxman, 1984; Wait, 1984; Kemna et al., 1997], although the proportionality constant will differ depending on the configuration settings of the time domain IP instrument. For example, VanVoorhis et al. [1973] found that M and ϕ were equivalent measures of IP by $\phi \text{ (mrad)} \approx 1.2 M \text{ (mV/V)}$, for their time domain instrumentation.

3.4 Electrical Properties

In nonmetallic environments, ignoring electronic conduction through minerals, the majority of electric charge is transferred by two mechanisms; electrolytic conduction (σ_{ele}) and surface conduction (σ_{surf}). Electrolytic conduction involves ionic transport of charge through the fluid in the interconnected pore space, while surface conduction occurs within an ionic double layer at the grain–fluid interface. Electrolytic conduction, a

purely real term (e.g. below 1 kHz), is controlled by water saturation, porosity and ionic concentration of the pore fluid. Surface conduction, a complex, frequency-dependent term is largely determined by specific surface area and grain/pore size distribution of the material. Fluid chemistry and mineralogy control the surface charge density and the surface ionic mobility and typically exert a second order control on surface conduction [Lesmes and Frye, 2001; Slater and Lesmes, 2002; Ulrich and Slater, 2004; Weller et al., 2011]. It is often assumed that the electrolytic and surface conduction paths add in parallel [Marshall and Madden, 1959; Vinegar and Waxman, 1984],

$$\sigma^* = \sigma_{ele} + \sigma_{surf}^* \quad (3.6)$$

Using this model, the real component of the measured complex conductivity (and therefore $|\sigma|$ obtained from a conventional resistivity survey, equation 3.3) is a function of both electrolytic and surface conductivity mechanisms whereas the measured imaginary component of the conductivity is only a function of the surface conductivity,

$$\sigma' = \sigma_{ele} + \sigma'_{surf} \quad (3.7)$$

$$\sigma'' = \sigma''_{surf} \quad (3.8)$$

Combining equation 3.4, 3.7 and 3.8, the phase response is given by:

$$\phi = \frac{\sigma''_{surf}}{\sigma_{ele} + \sigma'_{surf}} \quad (3.9)$$

Equation 3.9 shows that the phase response is controlled by both electrolytic conduction and the real and imaginary components of surface conduction [Schön, 1996]. Note that, in this study, positive phase angles define polarization (capacitive) effects because results are present in conductivity space.

3.5 Methods

3.5.1 Field surveys

Two-dimensional time domain resistivity/IP surveys were carried out in the 300 Area between the river corridor and the IFRC area in June 2010 (Lines 1-5), August 2010 (Lines 3b and 1V-3V) and March 2011 (Line 0). Figure 3.3 shows the location of ten resistivity/IP profiles covering about ~3 km of line length. Seven profiles running approximately parallel to the river were spaced ~20 m apart to better constrain structures and map the continuity of paleochannels that were expected, based on geological interpretations of the site, to run approximately E-W between the IFRC area and the river corridor. Line 0 was purposely close to the river (about 10 m from the river bank) in an effort to better identify paleochannels in direct contact with the riverbed. Three additional profiles were run approximately perpendicular to the river towards the IFRC area to better constrain structures within the local vicinity of the IFRC towards the river. Two boreholes, 399-1-57 and 399-02-01 [*DOE/RL-2010-99*] centered on our survey area (Figure 3.3) provided important information to ground truth the σ^* images.

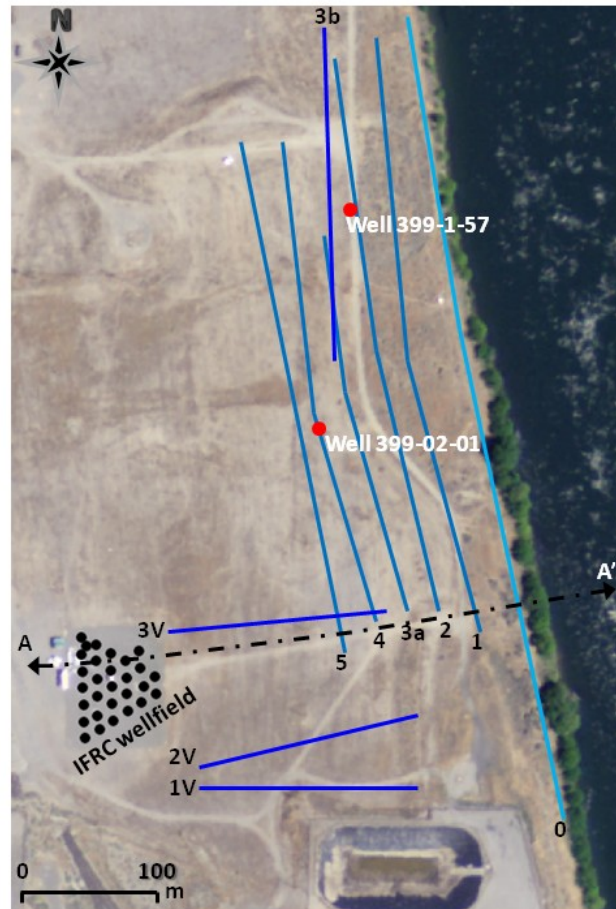


Figure 3.3 Profiles of time domain resistivity/IP performed adjacent to the Columbia River in the Hanford 300 Area, Richland, Washington. Black dots indicate the IFRC wells and the red dots are wells 399-1-57 and 399-02-01. The black dashed line represents the cross-section location.

We consider the first-order requirement for successful time domain IP data acquisition and interpretation to be a high signal-to-noise ratio (SNR) coupled with accurate error quantification. Electrode configuration is a key design factor controlling SNR while reciprocal measurements provide a robust approach to error characterization [LaBrecque *et. al.*, 1996]. All datasets were acquired with a 10-voltage channel Syscal Pro (Iris Instruments, France) time domain resistivity/IP meter (input impedance of 100 M Ω). The Syscal Pro system was used in a constant voltage mode set at 400 V: injected current

varied between 30 – 1850 mA depending on resistance between the current electrodes. For IP data acquisition, a total of 20 windows were sampled using a current waveform with a 1s on time, 1s off time, a 0.12 s delay time and individual window length of 0.04 s (total window length of 0.8 s).

Stainless steel electrodes were used in the field with variable electrode spacing (5 m spacing for Line 0 and Line 1, 4 m spacing for Line 2, Line 4 and Line 5 and 3 m spacing for Lines 3a-3b and Lines 1V – 3V). Electrode spacing varied with electrode cable and profile length e.g. Line 3a was shorter than other lines due to ongoing drilling activities at the time of surveying. We used a 96 electrode cable for the survey conducted on June 2010, a 64 electrode cable for the survey conducted on August 2010, and a 98 electrodes cable on March 2011.

Ideally, non-polarizing porous pot potential electrodes should be used to obtain the most reliable IP measurements. However, although non-polarizable porous pots electrodes may have lower errors levels when compared to metal electrodes [*Dahlin et. al.*, 2002; *LaBrecque and Daily*, 2008], they are not always a practical or cost-permitted choice in the field, especially for large arrays. Previous authors have shown that reliable IP data can be acquired with stainless steel electrodes [*Dahlin et. al.*, 2002; *LaBrecque and Daily*, 2008], under appropriate conditions e.g. using an instrument with a high input impedance (100 M Ω or better). In this study, our error levels when using stainless steel electrodes as an economical substitute for porous pots are quantified via full reciprocal

error analysis. This analysis (detailed below) justifies the use of stainless steel electrodes under the conditions encountered in our study.

We used a data acquisition sequence that consists of a combination of array types including short-offset dipole-dipole, nested dipole, Wenner, and “skip-two” (a dipole length of three electrodes) dipole types. These configurations were selected as they represent a good compromise between signal strength and resolution and provided a high SNR. Contact resistances were kept at below 3 k Ω (by watering electrodes with a salt-water mixture when needed) to minimize capacitive coupling and to ensure good electrical current injection (30 -1850 mA) during measurements. A complete set of reciprocal resistivity and IP measurements was acquired to facilitate error assessment and improve image reconstruction [LaBrecque *et. al.*, 1996]. Figure 3.4 shows representative decay curves indicative of data quality. The decay curves from Line 0 (Figure 3.4a) and Line 2V (Figure 3.4b) illustrate the generally good quality of the measured IP responses. Deterioration of the quality of the decay curve is observed, as expected, for the lower voltage measurements.

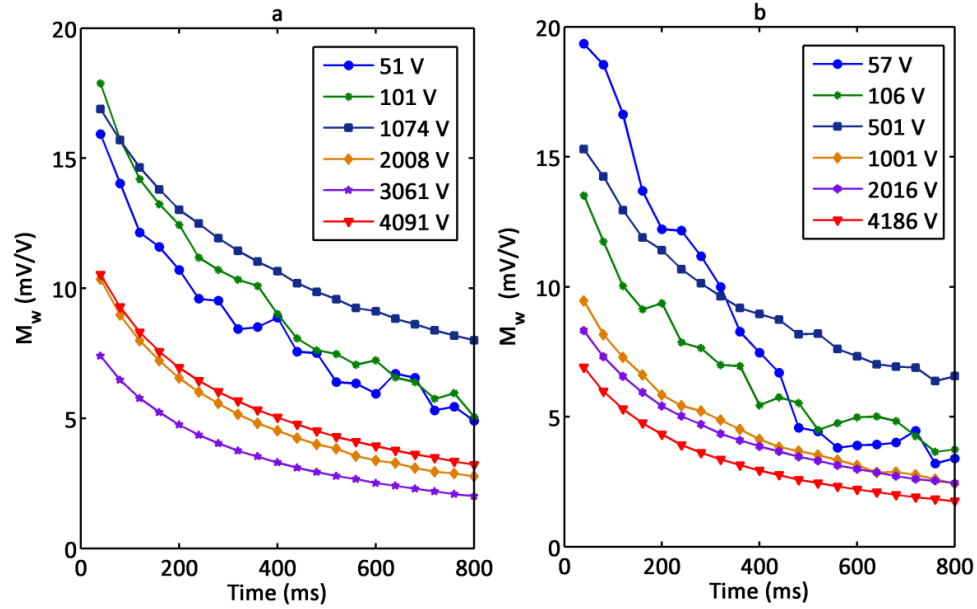


Figure 3.4 Example decay curves to illustrate the quality of measured field data at different voltages. Chargeability of 20 individual time windows (M_w) at different primary received voltages (a) Line 0, (b) Line 2V.

3.5.2 Laboratory calibrations

We carried out a laboratory study to calibrate the proportionality constant between frequency domain phase angle and the chargeability measured with the time domain instrument in the field. The analysis was done on four synthetic samples of sand-iron mixtures. The mixtures bear no relation to the field conditions, and were simply selected to provide a good range of polarization for the needed calibration. The four synthetic samples were (1) 100% sand by weight (2) 90% sand-10% iron by weight (3) 70% sand-30% iron by weight and, (4) 50% sand-50% iron by weight. The samples were saturated with NaCl solution of $\sim 450 \mu\text{S}/\text{cm}$ for 24 hr. We used a dynamic signal analyzer to directly measure the phase lag between current and voltage sinusoids at 1 Hz. Chargeability measurements were then carried out on the same samples using the Syscal Pro time domain resistivity/IP meter with the exact configuration as used in all field

measurements (i.e. for chargeability measurements, 20 windows were sampled using a current waveform with a 1s on and off time with 0.12 s delay time and individual window length of 0.04 s). We found that chargeability as measured with the field instrument could be converted to phase measured at the frequency of 1 Hz by $\phi (mrad) \approx 1.3M(mV/V)$ with a linear coefficient of determination (R^2) of 0.99.

We also used a mathematical approach described by *Kemna et al.* [1997] to convert measured chargeability to phase. This approach assumes a constant phase angle (CPA) with frequency response that would only be valid for soils where this assumption holds. Such a CPA response is likely to hold for materials that are characterized by a broad distribution of grain sizes [Cosenza et al., 2009], as is the case for the poorly sorted Hanford sediments. This assumption is supported by laboratory measurements on cores from the site. The Ringold sediments are somewhat better sorted and laboratory samples do show evidence of a weak polarization peak. Given the instrument settings used in the field, the approach of *Kemna et al.* [1997] estimates an M to phase conversion factor of 1.5 at a corresponding frequency of 0.25 Hz. This conversion coefficient is close to that determined from the laboratory study.

3.5.3 Error analysis

Our analysis of reciprocal errors extends an approach described in *Koestel et al.* [2008] by including an analysis of IP errors. To calculate IP errors, the measured chargeabilities were first converted to phase by using the relationship obtained from our laboratory

calibrations. We next developed error models based on normal and reciprocal measurements of resistance and phase angles.

Reciprocal errors for each resistance and phase measurement were first calculated using

$$\varepsilon_R = \text{abs} \left((N - R) / N \right) \times 100\% , \quad (3.10)$$

where N is a normal and R a reciprocal measurement. Data points were discarded if either the resistance or phase was greater than 100% of the subsequent mean of the normal (N) and reciprocal (R) measurements. After this analysis, we retained between 72 % - 97 % of the measurements on each line. More than 80% of the removed measurements were removed due to unacceptably ($\varepsilon_R > 100\%$) high phase errors.

In order to generate error models for the inversion, we divided the retained resistances and phase angles into 5 equal sized bins, i.e. each bin contained an equal number of measurements sorted in ascending order. For each bin, the average of the reciprocal errors was calculated. We then followed an empirical approach by selecting the simplest function that adequately captures the variation in error over the measurement range. A resistance error model for each dataset was best described by a power law function, representing dependence of the average of the resistance reciprocal error (ε_{res}) for each bin on the average resistance for each bin.

The use of reciprocal error as the only measure of error typically underestimates the true error level [Koestel *et. al.*, 2008; LaBrecque *et.al.*, 1996] and does not account for correlation between the individual errors. Importantly, it does not account for forward

modeling errors [Koestel *et. al.*, 2008; LaBrecque *et.al.*, 1996]. Due to the high quality of the resistance data acquired in the field, it was therefore also necessary to account for the modeling errors. Hence, the resistance error models were modified to account for forward modeling errors by adding 2% of the resistance mean (Equation 3.11);

$$\varepsilon_{res} = (a \times R^b) + (0.02 \times R) \quad (3.11).$$

The first term in equation 3.11 is the estimate of the data error and the second term is included to account for the model error (Figure 3.5A (a)). The 2% was chosen as the maximum representative modeling error, derived from synthetic trials on a flat, homogenous earth models using the same mesh discretization as used in the inversion of field datasets.

The same binning process was performed on the phase measurements. A phase error model for each dataset was best described with a quadratic function, representing the dependence of the average of the phase reciprocal error for each bin on the average of the phase for each bin (ε_ϕ),

$$\varepsilon_\phi = (aa \times \phi^2) + (ab \times \phi) + ac \quad (3.12)$$

For the phase measurements, it was not necessary to include the numerical model error because the phase data errors dominate the model errors (Figure 3.5A (b)). Profiles plotted on Figure 3.5A are generally representative of the entire survey, but only a few examples are shown for brevity. The lines shown are the ones I primarily focus on in the inversion results.

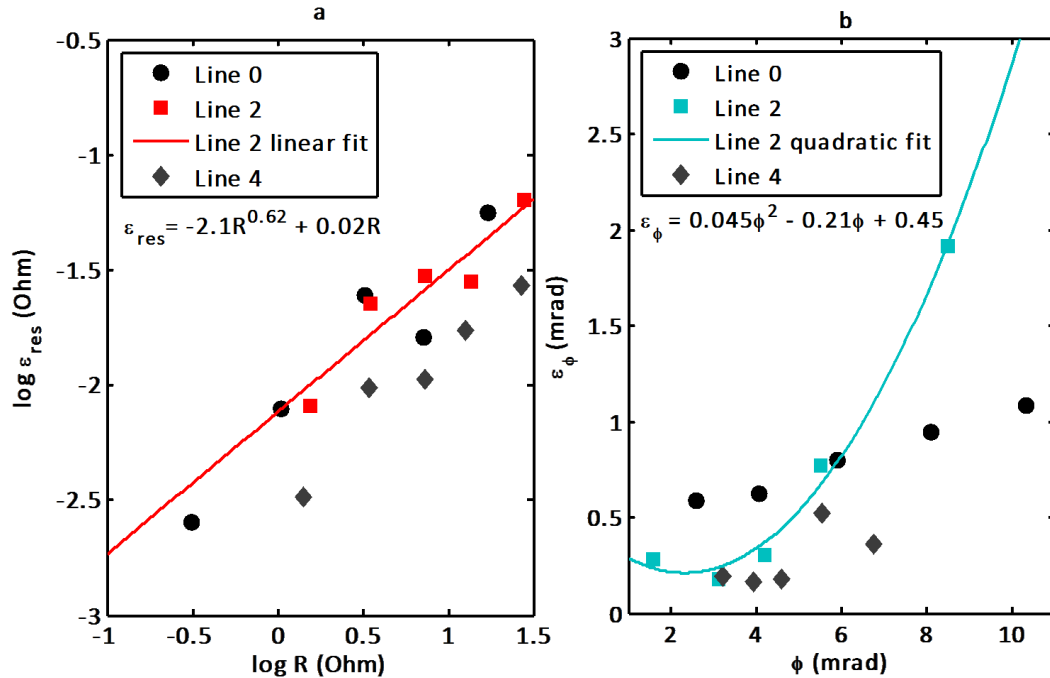


Figure 3.5A Error parameters obtained from modeling reciprocal errors in the field data (a) bins for average of resistance magnitude of Line 0, 2 and 4. Red line represents a power law relation to obtain individual resistance errors for Line 2 (b) bins of average phase angles of Line 0, 2 and 4. Blue line represents a quadratic fit to obtain individual phase errors for Line 2. The x and y axes represents the average values of the 5 bins.

Individual resistance and phase errors estimated from these models were then assigned as the individual data weights for each measurement in the dataset. The estimated weights for Line 4 (1064 data points retained from 1102 data points collected) have a mean of 0.002Ω and a standard deviation of 0.02Ω for the resistance measurements and a mean of 0.5 mrad and standard deviation of 2.6 mrad for phase measurements. These error estimates are close to the estimates found for other survey lines. The relative errors for all profiles show a cluster around zero with resistance showing lower relative error compared to the phase angles. Overall, the estimated relative errors on each line have a mean range of $0.002 - 0.03$ and standard deviation range of $0.002 - 0.24$ for resistance

measurements and a mean range of 0.07 – 0.8 and standard deviation range of 0.15 – 1.69 for phase measurements.

We performed further error analysis to examine the trade-off between data quality and data redundancy (Figure 3.5B). This error analysis was performed on Line 0 only whereby we discarded the resistance or phase with $\epsilon_R > 20\%$ of the subsequent mean of the normal (N) and reciprocal (R) measurements. After this analysis, I retained 716 measurements out of 1285 original measurements. This number (716 measurements) is 212 less measurements than what was retained after the first error analysis (i.e. after removing data with $\epsilon_R > 100\%$). Considering rejected measurements, 569 were removed due to unacceptably ($\epsilon_R > 20\%$) high phase errors compared to 260 resistance measurements of unacceptable high resistance error ($\epsilon_R > 20\%$).

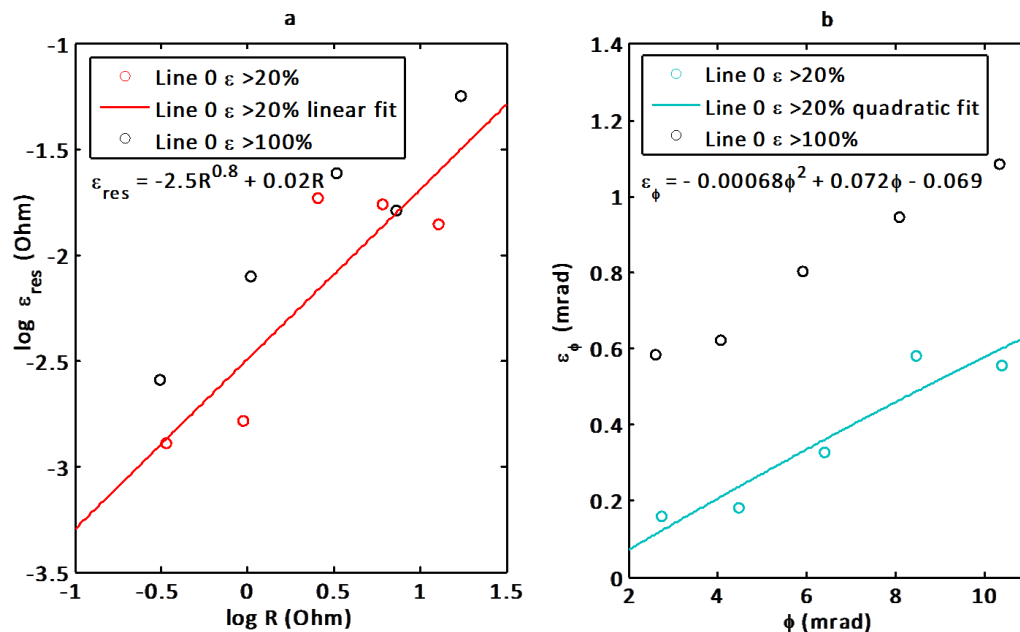


Figure 3.5B Error parameters obtained from modeling reciprocal errors of Line 0 with different error cut-off levels (a) bins for average of resistance magnitude of Line 0 with $\epsilon > 20\%$ removed (red) and $\epsilon > 100\%$ removed (black). The red line represents a power law relation to obtain individual resistance errors for Line 0 with $\epsilon > 20\%$ removed (b) bins of

average phase angles of Line 0 with $\varepsilon > 20\%$ removed (blue) and $\varepsilon > 100\%$ removed (black). The blue line represents a quadratic fit to obtain individual phase errors for Line 0 with $\varepsilon > 20\%$ removed. The x and y axes represents the average values of the 5 bins.

3.5.4 Inversion of field data

The solution of the σ^* forward problem was obtained using finite-element method based on a rectangular finite element mesh divided into foreground (fine discretization) and background (coarse discretization) regions. The foreground region contained two elements between electrodes in the horizontal directions and used half the element width in the vertical direction. The size of the elements in the background region expands away from the foreground region to accommodate the far-field boundary conditions.

We carried out a sequence of 2D σ^* inversions to predict subsurface changes in the spatial distribution of σ^* from our field data. Each profile was inverted individually as the lines were deemed too far apart to permit a 3D inversion of the entire datasets. The 2D σ^* inversion algorithm (described in detail by *Binley and Kemna*, [2005]) applied here uses a Gauss Newton method to iteratively finds the optimum value of a regularization parameter (λ), that minimizes an objective function (Ψ^*) composed of a data misfit term and a model stabilization term,

$$\psi^* = \|W_\varepsilon (d - f(m))\|^2 + \lambda \|W_m m\|^2 \quad (3.13)$$

where W_ε represent a data weighting matrix associated with data individual errors, d and f are vectors describing the measured data and the finite element forward solution for model vector m respectively, and W_m is a smoothness constraint representing the model weighting matrix [*Binley and Kemna*, 2005]. This algorithm requires resistance

magnitude and ϕ as input data [*Binley and Kemna, 2005*]. The phase angles calculated using the laboratory equation to convert M from time domain IP datasets were used as input for the inversion process.

Resistivity and IP image resolution is determined by SNR, survey design (including the spacing between electrodes and the distance from current sources) [*Slater and Binley, 2003*], forward model accuracy as well as parameterization and regularization constraints in the inversion approach [*Kemna, 2000; Day-Lewis et al., 2005, Binley and Kemna, 2005*]. Variations in the resolution of resistivity and IP images can be assessed quantitatively by the use of the model resolution matrix [*Day-Lewis et al., 2005*] or via synthetic studies where data are simulated for known model structures. A limited synthetic study was therefore performed to assess image resolution, particularly with respect to paleochannels.

3.6 Field Results

All 2D inversions resulted in a similar 2-layer structure so, for the sake of brevity, I primarily focus on just three lines for illustration (although integrated results from the inversion of all lines are presented later). Figure 3.6 shows representative inversion results for Line 0, Line 2 and Line 4 (located approximately 10 m, 50 m and 90 m respectively, from the river bank). Note that the 2D assumption is violated due to the presence of the river channel parallel to the survey lines (only significant for Line 0), along with variations in topography in the direction normal to the survey line. The σ^* inversion results are presented in the form of images of σ' , σ'' and ϕ . In all images shown

in this paper, the range of the color scale is centered on the mean of $\log(\sigma')$, $\log(\sigma'')$ and ϕ values, while the maximum is the mean plus one standard deviation and the minimum is the mean minus one standard deviation. The σ' and σ'' images contain very similar structure, a result that is expected when the complex surface conductivity (σ_{surf}^*) dominates the changes in both σ' and σ'' as anticipated here. We stress that, in the absence of ground truth data (e.g. borehole logs), this interpretation can only be made when the σ^* is imaged using IP measurements. All images depict a two-layer structure consistent with a much more polarizable and more conductive lower layer. The phase image indicates that the ratio of polarization to conduction (Equation 3.4 & 3.9) is greater in the lower layer.

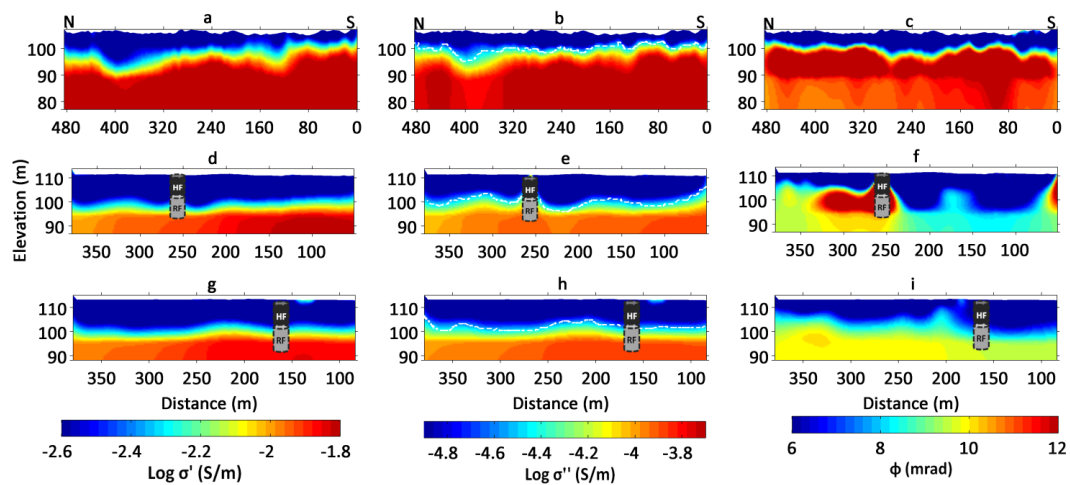


Figure 3.6 Electrical imaging results from 2D inversion of Line 0 (~10 m from shore), Line 2 (~50 m from shore) and Line 4 (~90 m from shore) showing (a) $\log \sigma'$ of Line 0 (b) $\log \sigma''$ of Line 0 (c) ϕ of Line 0 (d) $\log \sigma'$ of Line 2 (e) $\log \sigma''$ of Line 2 (f) ϕ of Line 2 (g) $\log \sigma'$ of Line 4 (h) $\log \sigma''$ of Line 4 and (i) ϕ of Line 4. Shown on Line 2 is the location of borehole 399-1-57 with H-R contact at 17.6 m and on Line 4 is borehole 399-02-01 with H-R contact at 14.33 m. Black dashed lines in b, e and h represent the estimated depth to the H-R contact from $\log \sigma''$ (S/m) = -4.7 threshold at 17.1 m on Line 2 and 12.44 m on Line 4. Note that there is a 6 fold vertical exaggeration on Line 0 and a 3.5 fold vertical exaggeration on Line 2 and 4.

Both the σ' and σ'' images exhibit a sharp contrast across the H-R contact, an observation that is expected assuming that lithology (hence σ_{surf}^*) controls these images. Such a contrast in σ'' (and σ') across the two units in Figure 3.6 is expected given the expected strong contrast in grain size distribution and surface area between the Hanford and Ringold units. Low σ'' and small ϕ observed in the upper layer, is consistent with low σ_{surf}^* associated with coarse-grained unconsolidated sediments of the Hanford Formation. In contrast, higher σ'' and larger ϕ in the bottom layer is consistent with high σ_{surf}^* associated with the fine-grained sediments of the Ringold Formation. The electrical structures observed along the other seven profiles in the 300 Area (not shown here for conciseness) closely resemble those observed in Figure 3.6.

A threshold of $\log_{10} \sigma''$ (S/m) = -4.7 was applied to the σ'' images of Lines 0, 2 and 4 to estimate the depth to the contact between the Hanford Formation and the underlying Ringold Formation. This value was selected based on laboratory spectral induced polarization measurements on samples acquired from the 300 Area IFRC well field whereby for two Ringold cores consistently measured $\log_{10} \sigma''$ (S/m) \geq -4.6. The white dashed line in Figure 3.6b, 3.6e and 3.6h represents the estimated H-R contact in the σ'' images of Line 0, Line 2 and Line 4 based on this threshold. The position of these lines corresponds well with the location of the interface that would be visually inferred from the images.

The images for Line 2 and Line 4 (Figure 3.6d, 3.6e, 3.6g and 3.6h) indicate a contact between the Hanford Formation and Ringold Formation at a depth of approximately 17.5

m and 14.3 m respectively, at the locations that coincide with the boreholes. The estimated depth on Line 2 correlates very well with the 17.6 m depth to the H-R contact observed from the borehole 399-1-57 located at about 240 m along this line [Bjornstad *et al.*, 2009; DOE/RL-2010-99]. Borehole 399-02-01 located at about 180 m along Line 4 encountered the H-R contact at approximately 14.3 m [DOE/RL-2010-99], consistent with our estimated depth. However, the presence of the borehole on Line 2 appears to distort the phase measurements (Figure 6f), which probably results from the steel casing and perhaps also the bentonite grout used to complete the borehole. Line 2 was surveyed at the same time as borehole 399-1-57 was being drilled (in contrast, borehole 399-02-01 was drilled after Line 4 was surveyed).

Considerable variation in the elevation of the H-R contact is captured when moving from locations inland towards the river (Figure 3.6). The estimated elevation of the H-R contact generally decreases towards the river. Substantial variability in the thickness of the Hanford Formation on Line 0, close to the river, is predicted from the inversion. The elevation of the contact is higher towards the southernmost part of Line 0 relative to the middle and northern sections of this line. The thickest sections of the Hanford Formation are observed at 110–140 m, 200 m and 380–420 m along Line 0. Substantial variation in the thickness of the Hanford Formation beneath the riverbed was also observed by Slater *et al.* [2010] from waterborne electrical measurements and was considered significant for determining the connectivity between the aquifer and the river, with implications for controlling the exchange of uranium contaminated groundwater with river water. Slater *et al.*, [2010] argued for the evidence of locations where coarse channel fill materials were

locally eroded below the Hanford-Ringold contact. The land-based measurements recorded in this work also show areas where the σ^* images offer evidence of thicker accumulations of low polarizability materials that could be interpreted as channel features locally eroded beneath the H-R contact. Such features are observed at 50 m–70 m, 110–140 m and 380 m–420 m along Line 0. There is some evidence for continuity of these features between lines across the survey area e.g. towards the end of Line 2 and south of the surveyed area toward IFRC site (Figure 3.6 & 3.10).

Inversion results of long lines (e.g. Line 0) compared to the short lines (e.g. Line 1V) in Figure 3.7 shows that, despite the different electrode settings used in the field, both lines can resolve the primary subsurface structure and the H-R contact. A similar sharp contrast between the top and bottom layer in the σ' and σ'' images in Line 0 (Figure 3.7a and 3.7b) is also observed in Line 1V (Figure 3.7d and 3.7e). The ϕ image in Figure 3.7c is also similar to that shown in Figure 3.7f with small changes in ϕ across the H-R contact. However, some loss in resolution is evident in the shorter line (Line 1V) (Figure 3.7d and 3.7e) compared to Line 0 (Figure 3.7a and 3.7b).

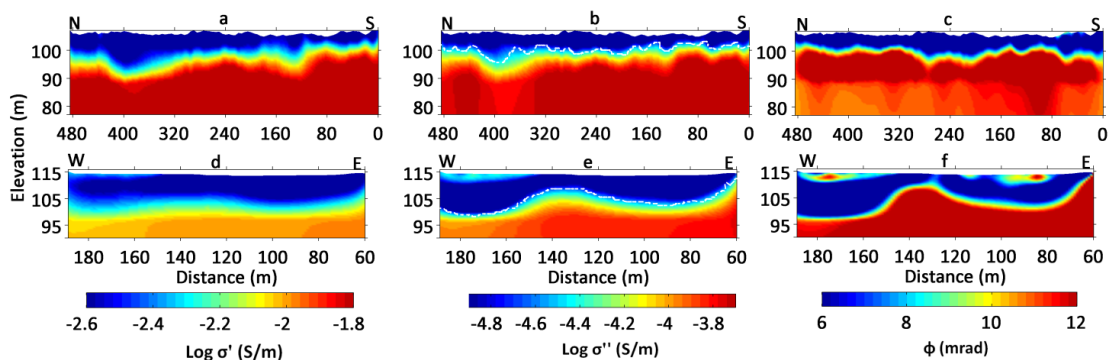


Figure 3.7 Inversion results of Line 0 (parallel to the river) and Line 1V (diagonal to the river) showing (a) $\log \sigma'$ of Line 0 (b) $\log \sigma''$ of Line 0 (c) ϕ of Line 0 (d) $\log \sigma'$ of Line

1V (e) $\log \sigma''$ of Line 1V (f) ϕ of Line 1V. Note that there is a 6 fold vertical exaggeration on Line 0 and a 3.5 fold vertical exaggeration on Line 1V.

Figure 3.8 shows inversion results for Line 0 at two different error cut-off levels. The inversion results with $\epsilon_R > 20\%$ removed (Figure 3.8a, 3.8b and 3.8c) correspond closely to the results with $\epsilon_R > 100\%$ removed (Figure 3.8d, 3.8e and 3.8f). Even though there are slight differences in length and width of the thicker sections of the Hanford Formation at 430 m - 270 m and 220 m - 120 m in both σ' and σ'' images (Figure 3.8a, 3.8b, 3.8d and 3.8e), the resolution of all images is high and the estimated H-R contact (white dashed line) is similar in both σ'' images (Figure 3.8b and 3.8e). The ϕ images exhibit slight differences in the bottom layer (Figure 3.8c and 3.8f). While Figure 3.8c shows an almost uniform Ringold Formation, Figure 3.8f resolves higher ϕ in the uppermost portion of the Ringold. This additional structure may reflect extra information from the additional measurements that are incorporated into the inversion for the case with $\epsilon_R > 100\%$, even though these measurements are not weighted heavily.

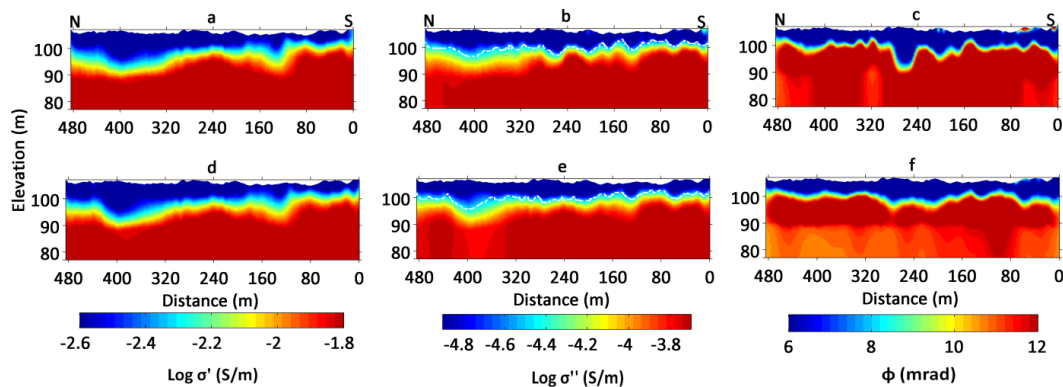


Figure 3.8 Inversion results of Line 0 at different error cut-off levels (a) $\log \sigma'$ of Line 0 with $\epsilon > 20\%$ removed (b) $\log \sigma''$ of Line 0 with $\epsilon > 20\%$ removed (c) ϕ of Line 0 with $\epsilon > 20\%$ removed (d) $\log \sigma'$ of Line 0 with $\epsilon > 100\%$ removed (e) $\log \sigma''$ of Line 0 with $\epsilon > 100\%$ removed (f) ϕ of Line 0 with $\epsilon > 100\%$ removed. Note the 6 fold vertical exaggeration.

3.7 Synthetic Data

Synthetic modeling was conducted to constrain the interpretation of the field data by (1) exploring the ability of the σ^* to resolve a depression in the H-R contact with the characteristic dimensions of a paleochannel expected at this site, and (2) investigating the effects of noise estimates on the resolution of σ^* images.

Synthetic models were constructed based on both borehole observations and the images from the inversion of the field datasets. We generated two models for forward modeling, with Model 1 (see appendix A) based on a 1D model with a two-layer structure to represent a simplified version of the results observed for Line 4 in Figure 3.6g-3.6i. Line 4 was chosen for this synthetic study because of heterogeneity in the Hanford Formation observed within this line. The depth to the H-R contact, along with representative values for $|\sigma|$ (1.053×10^{-3} S/m and 1×10^{-2} S/m for Hanford and Ringold formations, respectively) and ϕ (2.6 mrad and 9.1 mrad for Hanford and Ringold formations, respectively) were based on the field inversion result for Line 4 and consistent with laboratory measurements on cores from the site.

Model 2 (Figures 3.9 & see appendix A for additional figure of Model 2) had two layers as per Model 1 but included a simulated paleochannel incised into the bottom layer (the Ringold Formation). Using ground penetrating radar (GPR) measurements, *Slater et al.* [2010] estimated the width of a paleochannel identified in the 300 Area to be ~35 m while *Kunk and Narbutovskih*, [1993] estimated paleochannels at the site to be 0 - 4.5 m deep and less than 30 m wide. Based on this information, we modeled a hypothetical

channel incised 6 m beneath the H-R contact and 24 m wide. It is conceivable that smaller paleochannels than those mapped by *Kunk and Narbutovskih* [1993] exist at the site. Such paleochannels could exert a strong influence on flow at this site but would be beyond the detection limits of the σ^* imaging. Our model thus likely represents a best case scenario with respect to detection of such a feature with the IP method.

We created two datasets per model, one using the electrode configuration used in the field measurements (field configuration, Figures 3.9) and one using a dipole-dipole array (see appendix A for figures from dipole-dipole array modeling). Synthetic data were created using only electrode configurations that were retained in the field data after the error analysis defined previously (i.e. after removing data with $\varepsilon_R > 100\%$). To better understand the limitations of field-scale IP imaging and illustrate how noise affects the resolution of conductivity/IP images, we ran the model simulation with a range of different simulated reciprocal error levels. Synthetic data were contaminated with either (1) the noise representative of the site estimated from field error models of Line 4, or (2) random, normally distributed noise representing two error levels for resistance data and two error levels for phase data. The two error levels were defined for the resistance data by a standard deviation (σ_d) of the relative resistance error of 0.05 and 0.1; for the phase data the standard deviation of phase error (ϕ_d) was varied between 1 mrad and 2 mrad. In all cases the mean of the errors was zero. We used the field error model for Line 4 as this is the line modeled here. Individual error estimates for the inversion were then calculated based on the procedure described earlier (Equation 3.11 – 3.12).

3.8 Synthetic inversion results

Figure 3.9 shows the synthetic model and the corresponding inversion results. The black dashed lines define the modeled H-R contact in the synthetic models while the white dashed line represents the predicted H-R contact (based on the $\log_{10}(\sigma'')$ (S/m) = -4.7 threshold) from the inversion of the synthetic data. As expected, image resolution decreases with increasing error level. The H-R contact is well resolved at the field error level and there is also evidence of the paleochannel, although the feature is not well defined. The H-R contact (black dashed line in the σ'' images) is resolved in both σ' and σ'' images (white dashed line in Figure 3.9(2b)). However, the paleochannel is only resolvable at the field error level, as evident in the σ' and σ'' images of Figure 3.9 (1b & 2b). At higher error levels ($\sigma_d \geq 0.02$) neither the σ' nor σ'' image shows evidence of the depression. There is no evidence of variable resolution along the profile resulting from bias in the sensitivity due to the measurement sequence.

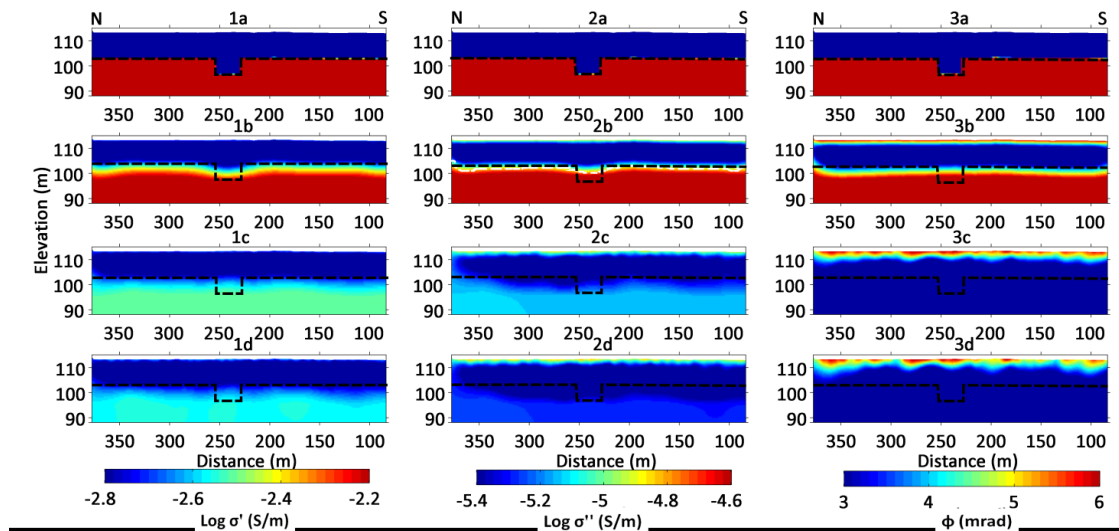


Figure 3.9 Inversion results of the synthetic data from the configuration used in field (1a) model of $\log \sigma'$ (1b) inversion results with field error (1c) inversion results with $\sigma_d = 0.05$ (1d) inversion results with $\sigma_d = 0.1$ (2a) model of $\log \sigma''$ (2b) inversion results with field error (2c) inversion results with $\sigma_d = 0.05$ (2d) inversion results with $\sigma_d = 0.1$ (3a) model of ϕ (3b) inversion results with field error (3c) inversion results with $\phi_d = 1$ mrad (3d)

inversion results with $\phi_d = 2$ mrad. The black dashed lines represent the modeled H-R contact while the white dashed lines on the σ'' images represents the resolved H-R contact from inversion of the synthetic data using $\log(\sigma'')$ (S/m) = -4.7 threshold. Evidence of the modeled paleochannel and H-R contact can only be resolved at the field error level. Note the 3.5 fold vertical exaggeration.

Phase angles show high sensitivity to errors, resulting in severe loss of model structure with increasing noise level. In fact, evidence of the H-R contact can only clearly be resolved in the ϕ image with the field error estimate (Figure 3.9 (3b)) as significant distortion of true model structure is observed even for the lowest synthetic error level (1 mrad). At 2 mrad and higher error levels, there is no evidence of the H-R contact and ϕ artifacts are severe enough to result in an anomalously thin layer of high phase angle (Figure 3.9 (3c and 3d)).

3.9 Discussion

3.9.1 Implications for lithological characterization of the 300 Area

We show how field-scale σ^* imaging can be used to remove the inherent ambiguity in the interpretation of lithological structure that exists when using measurements obtained from resistivity imaging alone. Whereas σ' (and $|\sigma|$ (measured with resistivity) is strongly controlled by fluid conductivity, porosity and surface area/grain size distribution, σ'' resolvable with an additional IP measurement is primarily controlled by the surface area/grain size distribution. The full σ^* images confirm that the geoelectrical structure at this site results from the high surface conductivity of the Ringold Formation compared to the overlying Hanford Formation in response to changes in surface area/grain diameter and grain size distribution. The σ^* images also suggest that changes in water chemistry

due to surface water- groundwater interaction along the river corridor exert only a weak impact on the geoelectrical structure.

We have previously emphasized that the H-R contact is an important interface controlling flow and transport at this site. There exists a strong need to better characterize the spatial distribution of the depth to this interface between the 300 Area IFRC and the river to improve understanding of transport of uranium between the aquifer and the river. The σ^* images provide unique near continuous information on the spatial variation in depth to this contact across the survey area. In order to illustrate this information content further, the threshold of $\log_{10} \sigma'' \text{ (S/m)} = -4.7$ was applied to the σ'' images for all lines to represent the transition from the Hanford Formation to the underlying Ringold Formation. Figure 3.10a is a plan view of the site showing the estimated elevation of the H-R contact between the river and the IFRC area based on this threshold. The overlying contours on Figure 3.10a represent the elevation of the H-R contact estimated from boreholes scattered across the 300 Area. The interpolation of the borehole data points suggest a depression in the H-R contact in the middle of the surveyed area, running perpendicular to the surveyed profiles toward the Columbia River. However, this spatial interpolation is very uncertain due to the low number of data points.

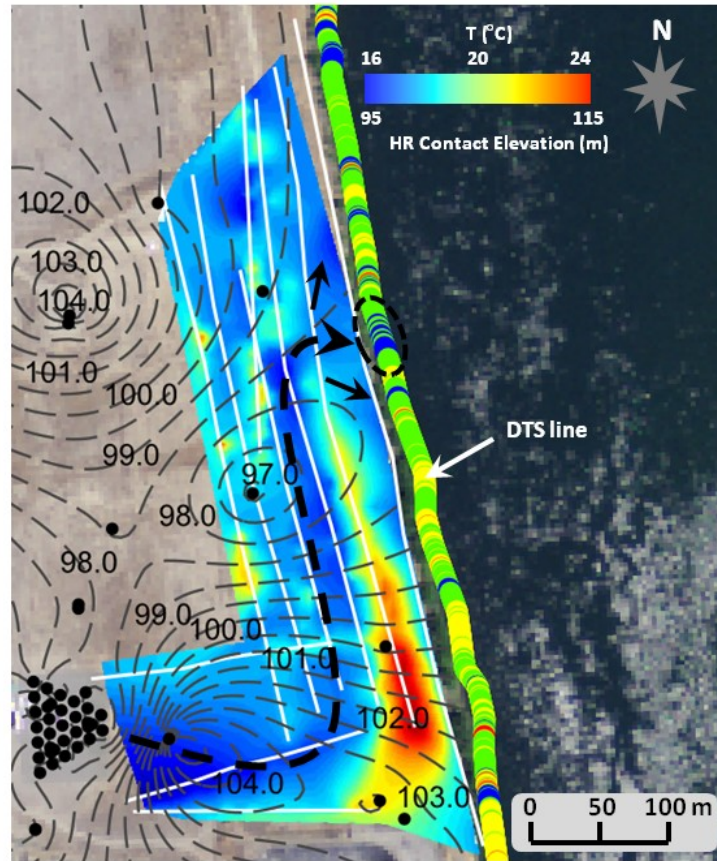


Figure 3.10a Elevation of the Hanford-Ringold contact estimated using $\log(\sigma'')$ (S/m) = -4.7 threshold overlaid on H-R elevation contours estimated from borehole data across 300 Area. Black dots represent boreholes at the 300 Area used for the interpolation. White lines indicate resistivity/IP survey profiles. Black dashed arrows outline center of an estimated depression in the H-R contact that might reflect a paleochannel. Temperature (T °C) distribution from fiber optic-distributed temperature sensing (FO-DTS) for measurements at low river stage on August 2009 is plotted next to the H-R contact elevation to indicate areas of focused groundwater discharge (cooler temperatures in the summer) that appear to be associated with the depression on the H-R contact.

The results from 2D inversion of the σ^* data show evidence of depressions in the H-R contact that roughly correspond to the depression depicted from the borehole data. The predicted distribution of the H-R elevation based on the σ'' threshold extracted from the field images is based on a much greater data density providing more confidence in the predictions of the interpolation. We primarily attribute the large discrepancies between the σ^* derived H-R elevation estimates and the borehole estimates to the small number of

boreholes, some of them >100 m apart, used to approximate the elevation. A similar problem likely holds for the estimation of the H-R elevation between the diagonal profiles, 1V, 2V and 3V. Profiles 1V and 2V are further apart (>100 m) from profile 3V, which likely further explains the discrepancy between the borehole estimation of the H-R elevation and our σ^* derived H-R elevation estimates.

We estimated the depth to the H-R contact to range from ~19.8 m, inland close to the IFRC area, to < 5 m in the shallowest parts close to the river. A prominent depression in the elevation of the contact appears to exist east of the IFRC, turning to run approximately parallel to the river corridor. The size of this depression, ~30 m wide, is consistent with the size of potential paleochannels estimated by Slater *et.al.* [2010] and Kunk and Narbutovskih [1993] and might therefore represent a paleochannel at one point running parallel with the river from the IFRC area. As proposed earlier, the presence of paleochannels in this study site may result in preferential groundwater-surface water exchange between the 300 Area and the Columbia River. Our results support this idea due to the fact that the location where the proposed paleochannel connects with the river corresponds to enhanced groundwater discharge zones predicted from distributed temperature sensing (DTS) datasets from the 300 Area river corridor (Figure 3.10a). Furthermore, the depression in the H-R contact appears to correspond well to an area exhibiting high uranium discharge [Williams *et al.*, 2007] in the 300-Area (Figure 3.10b). The highest uranium contours occur at the point where the paleochannel mapped within the σ^* images exits to the river; this also coincides with the temperature anomalies, suggesting a zone of focused groundwater discharge (Figure 3.10b). Synthetic modeling

demonstrated that it is feasible to resolve depressions on the scale of expected paleochannels at this site given the noise levels recorded in this survey.

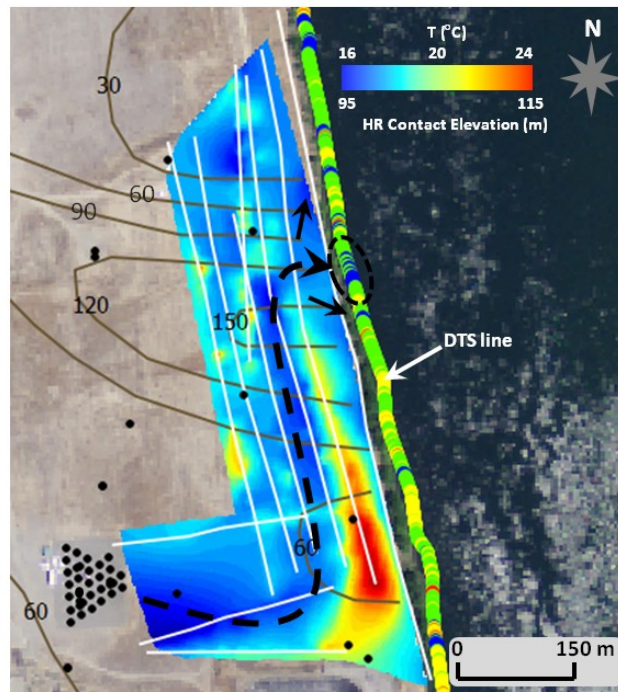


Figure 3.10b Elevation of the Hanford-Ringold contact overlaid on brown contours representing uranium concentration ($\mu\text{g/L}$), after *Williams et al.* [2007]. The areas of high uranium concentration appear to coincide with a depression in the Hanford-Ringold contact and areas of focused groundwater discharge.

3.9.2 Implications for complex conductivity field surveys

Our synthetic studies emphasize the point that good quality IP measurements are essential for reliable interpretation of such data in terms of lithological structures. In general, degradation of the resolution of the σ^* parameters most strongly controlled by the IP measurements (ϕ , σ'') is significantly greater than the degradation of resolution of σ' (the property primarily sensed in a conventional resistivity survey) for representative increases in noise level for resistance and phase measurements. The reciprocal errors for the phase measurements were significantly higher than those of the resistance

measurements, an unavoidable consequence of the lower SNR of the IP measurements. This lower SNR is propagated through the inversion and results in lower resolution images for the ϕ images.

The synthetic modeling confirms that discrimination of lithologic contacts, and even depressions in this contact, is plausible given the error levels in our field dataset. However, the poor resolution of the two layers observed in the ϕ images for the higher error level ($\phi_d \geq 1$ mrad) is an unavoidable consequence of the low SNR in the IP measurements. The resolution of the contrast between the two layers decreases significantly with the increase in σ_d . The resolution of a two layer structure in the σ' images is less affected by the increasing error levels compared to the σ'' images. For the σ' images, the resolution of two layers is qualitatively clear at all error levels although the contrast between the two layers decreases with increasing error level. The σ'' image similarly resolves a two layer structure with a decreasing contrast as error levels increase, but artifacts develop in the top layer of σ'' images at higher error levels ($\sigma_d \geq 0.02$). Artifacts in the σ'' images are expected as σ'' is more dependent on the IP measurements, being the source of these artifacts.

The modeled depression in the H-R contact can only be resolved at the field error level in the σ' and σ'' images only. The ϕ images were unable to resolve the paleochannel at all error levels due to low SNR in phase data. As a result of its dependency on ϕ , σ'' failed to resolve the paleochannel at high error levels ($\sigma_d \geq 0.02$). The ability to resolve a

synthetic paleochannel feature at the field error level gives confidence in our interpretation of evidence for depressions in the H-R contact at the 300-Area.

In summary, the low SNR of IP measurements is a major factor affecting the resolution of σ^* images. However, given appropriate care to quantify and model measurement errors, IP measurements can provide an important constraint on the geoelectrical interpretation of a site. As discussed, the IP measurements and full σ^* imaging permit evaluation of the relative strengths of lithology versus fluid chemistry on the electrical datasets. We therefore argue that IP measurements should always be acquired, when possible, to build confidence in the interpretation of imaged geoelectrical structure, even given the inherent lower SNR of IP measurements relative to resistance measurements.

3.10 Conclusions

The strong dependency of surface conductivity on surface area makes σ^* imaging a unique geophysical tool for lithological identification when compared to electrical resistivity imaging alone. However, σ^* parameters that depend most strongly on the IP measurements will inevitably be low resolution due to unavoidably small SNR for chargeability or phase angle measurements, requiring additional care during data acquisition and data processing to ensure high quality information. In particular, appropriate data weight needs to be considered for successful inversion of IP measurements. Through synthetic studies we have shown how the increase in error level rapidly produces artifacts and decrease the resolution of σ^* parameters most controlled by the IP measurements.

Time domain resistivity/ IP data collected at the Hanford 300 IFRC area have provided high-resolution information on spatial variation in depth to a critical lithological contact known to control flow and transport between the river and the 300 Area. The large contrast in surface conductivity between the two lithologic units is well resolved in σ^* imaging. Variations in the imaged elevation of this contact reveal evidence of depressions that may represent paleochannels improving the hydraulic connectivity of the IFRC area to the river. Such information is needed to improve groundwater flow models and hence understanding of the transport of uranium from the 300 Area into the Columbia River.

CHAPTER 4

4.0 Spatially variable stage-driven groundwater-surface water interaction inferred from time-frequency analysis of distributed temperature sensing data²

Abstract

Characterization of groundwater-surface water exchange is essential for improving understanding of contaminant transport between aquifers and rivers. Fiber-optic distributed temperature sensing (FO-DTS) provides rich spatiotemporal datasets for quantitative and qualitative analyses of groundwater-surface water exchange. We demonstrate how time-frequency analysis of FO-DTS and synchronous river stage time series from the Columbia River adjacent to the Hanford 300-Area, Richland, Washington, provides spatial information on the strength of stage-driven exchange of uranium contaminated groundwater in response to subsurface heterogeneity. Although used in previous studies, the stage-temperature correlation coefficient proved an unreliable indicator of the stage-driven forcing on groundwater discharge in the presence of other factors influencing river water temperature. In contrast, S-transform analysis of the stage and FO-DTS data definitively identifies the spatial distribution of discharge zones and provided information on the dominant forcing periods (≥ 2 days) of the complex dam operations driving stage fluctuations and hence groundwater-surface water exchange at the 300-Area.

²This work has been published, should be cited as: Mwakanyamale, K., L. Slater, F. Day-Lewis, M. Elwaseif, and C. Johnson (2012), Spatially variable stage-driven groundwater-surface water interaction inferred from time-frequency analysis of distributed temperature sensing data, *Geophysical Research Letters*, 39, L06401, doi: 10.1029/2011GL050824.

4.1 Introduction

The natural contrasts in temperature between groundwater and surface water provide opportunities to use temperature to obtain both quantitative and qualitative information on groundwater-surface water exchange. Groundwater exhibits relatively constant temperature compared to surface water, e.g. stream temperatures vary annually on a range between 0° C and 25° C [*Constantz et al.*, 1994] whereas groundwater commonly exceeds the mean annual air temperature of the locality by 2 to 3 degrees [*Bechert and Heckard*, 1966] and varies little over the seasons. The use of fiber optic distributed temperature sensing (FO-DTS) allows continuous measurements of temperature in both time and space at a high spatiotemporal resolution, and can now be deployed with cable lengths up to thousands of meters, with temperature resolution of 0.01 °C for every meter, and with temporal resolution of fractions of a minute. FO-DTS has been used in a number of hydrological studies, especially in studies of groundwater-surface water exchange. For example, *Selker et al.* [2006a] used FO-DTS in fluvial systems to locate groundwater sources along a stream, whereas *Lowry et al.* [2007] used FO-DTS to identify spatial variability in groundwater discharge in wetland systems. FO-DTS produces rich temporal datasets suitable for both time series and time-frequency analysis, although, until recently, the benefits of this analysis of FO-DTS data have not been fully exploited.

The Fourier transform has been used for spectral analysis of time series for decades. The lack of time localised information in the Fourier spectrum [*Mansinha et al.*, 1997] led to the development of more powerful methods that offer joint time-frequency representation

of time series, e.g. the S-transform [Stockwell *et al.*, 1996]. Such transforms offer progressive resolution of both time and frequency. Time-frequency analysis of FO-DTS data therefore provides a means to better understand spatial and temporal variations of hydrological processes by examining the frequency content of those processes as a function of time. Henderson *et al.* [2009] demonstrated the use of time-frequency analysis of FO-DTS by using a wavelet transform to characterize the time-variable frequency content of a FO-DTS temperature time series and comparing it with a tidal level time series, in order to improve understanding of forcing mechanisms on aquifer-estuary exchange.

In this study, we (1) demonstrate the use of time-frequency analysis to provide proxy indicators of exchange that are more reliable than parameters extracted from the time series alone, and (2) obtain spatial information on the strength of the stage-driven exchange in response to subsurface heterogeneity along a major river corridor where heterogeneity is believed to influence the exchange of uranium contaminated groundwater with river water.

4.2 Field Site

The 300-Area is located at the south end of the Hanford site, north of Richland, Washington (Figure 4.1a). In the 300-Area, uranium-contaminated groundwater discharges into the Columbia River through the zone of groundwater-surface water exchange along the river corridor. The Integrated Field Research Challenge (IFRC) site has been established in the 300-Area to study field-scale contaminant mass transfer

processes [Ma et. al., 2011]. Our study site is a 1.6-km long portion of the river corridor approximately centered on the IFRC. The hydrogeologic framework of the river corridor at the 300-Area is defined by an upper unconsolidated permeable aquifer (Hanford Formation) overlying a less permeable semi-consolidated and semi-confining unit (Ringold Formation). Geophysical imaging suggests that the thickness of the Hanford Formation ranges from 13.01 to 0.33 m along the 300-Area river corridor, being thicker towards the north, and thinning out in the south where the underlying Ringold Formation is in contact with the riverbed [Slater et. al., 2010].

The Hanford Formation consists of unconsolidated sediments, pebble to boulder sized basalts and fine to coarse grained sand [Kunk and Narbutovskih, 1993] with a high hydraulic conductivity of ~2000 m/d [Williams et. al., 2007]. The Ringold Formation is divided into gravel-dominated (upper) and mud-dominated (lower) units [Newcomb, 1958]. The upper unit consists of cemented and compacted quartzitic gravels with mica-rich silt and fine sand matrix [Lindberg & Bond, 1979] with a hydraulic conductivity of 40-120 m/d [Williams et. al., 2007]. The lower unit has hydraulic conductivity of ~1 m/d [Williams et. al., 2007] and consists of silty-clay to silty-sand sediments [Tyler, 1992]. Focused exchange between groundwater and river water along the Columbia River corridor in the 300-Area is believed to be facilitated by buried channels of high permeability floodwater deposits locally incised below the Hanford-Ringold contact during low river stage [Lindberg and Bond, 1979]. These channels are believed to run both parallel and perpendicular to the river. Slater et al., [2010] found evidence of the paleochannels in waterborne electrical imaging surveys and temperature anomalies from

FO-DTS datasets along the 300-Area river corridor. These results suggest that spatial variation in lithology along the Columbia River corridor is likely to exert a strong control on stage-driven focused groundwater discharge into the river. Direct evidence for focused exchange at the riverbed comes from uranium seeps identified at a number of locations (Spr-7 – Spr-11) [Williams *et. al.*, 2007] along the river corridor (Figure 4.2). Complex river stage fluctuations controlled by dam operations upstream of the 300-Area [Lindberg and Bond, 1979] impose a complex flow head boundary condition, regulating groundwater exchange and presumably influencing uranium transport via these seeps.

4.3 Methods

4.3.1 Fiber Optic Distributed Temperature Sensing

The FO-DTS method is based on measuring the travel time of a scattered or reflected laser pulse returned from points along the fiber optic cable. A portion of the transmitted energy is scattered back with wavelength less than (anti-Stokes) and higher than (Stokes) the original wavelength, as a result of (1) density changes in the fiber caused by electromagnetic forces from the passage of light (Brillouin Scattering) [Selker *et al.*, 2006b], and (2) loss/gain of energy exchange with electrons (Raman Scattering) [Selker *et al.*, 2006b]. The amplitude of the Raman anti-Stokes backscatter is linearly dependent on temperature. By measuring the ratio of the amplitude of the anti-Stokes to the Stokes backscatter, temperature can be recorded everywhere along the cable [Selker *et al.*, 2006a, 2006b].

4.3.2 S-transform

The S-transform is an extension of the windowed Fourier transform that was introduced and defined by *Stockwell et al.* [1996] as a time-frequency representation, whereby the local frequency spectrum is defined at each point along the time axis. This spectral localization is different from the wavelet transform [*Mansinha et. al.*, 1997a] used to analyze FO-DTS data by *Henderson et al.* [2009] in that the S-transform preserves frequency-dependent resolution while simultaneously maintaining the direct relationship with the Fourier spectrum through time-averaging [*Stockwell et al.*, 1996].

The 1-D S-transform is based on a moving and scalable localizing Gaussian window [*Stockwell et al.*, 1996]. The width of this Gaussian window varies as a function of frequency along the time axis as it maps the 1-D time series into a complex function of both time and frequency [*Mansinha et. al.*, 1997b]. A complete and lossless invertibility between the time (t) to time-frequency (t, f), to frequency (f) and back to time domain is achieved. The 1-D S-transform is defined as,

$$S(\tau, f) = \int_{-\infty}^{\infty} h(t) \frac{|f|}{\sqrt{2\pi}} e^{-\frac{(\tau-t)^2 f^2}{2}} e^{-i2\pi f t} dt \quad (4.1)$$

where $h(t)$ is the time series to be analyzed and τ is the time of the spectral localization. Note that the time average of $S(\tau, f)$ gives the Fourier spectrum.

The 2-D S-transform provides variations in the amplitude of a time series for a particular period at each location. The 2-D S-transform is defined using,

$$\begin{aligned} & S(x, y, k_x, k_y) \\ &= \int_{-\infty}^{\infty} \int_{-\infty}^{\infty} h(x', y') \frac{|k_x| |k_y|}{2\pi} e^{-\frac{(x'-x)^2 k_x^2 + (y'-y)^2 k_y^2}{2}} e^{-i2\pi(k_x x' + k_y y')} dx' dy' \quad (4.2) \end{aligned}$$

where x and y are spatial variables and k_x and k_y are wavenumber variables ($k_x = 1/\lambda_x$, where λ_x is the wavelength in the respective direction).

4.3.3 Field data acquisition

In November 2008, a 1.6 km long ruggedized SensorNet EnviroFlex FO cable (~1 cm diameter) with two 50-micron multimode fibers was installed on the riverbed at ~2 m from the river bank, about 0.15 to 0.76 m deep, approximately centered on the IFRC area (Figure 4.1). (Note that any use of trade, product, or firm names is for descriptive purposes only and does not imply endorsement by the U.S. Government). The cable was installed at 2 m from the river bank with the aim of capturing the connectivity between aquifer and the river. Heavy weights (large cobbles and/or breeze-blocks) were used to anchor the cable to ensure it remained static and under water. A Sensortran 8-channel Gemini control unit was programmed to collect the water temperature at the river bed every 0.51 m along the cable (for a total of 2871 measurement locations) at a 5 minutes interval. The FO-DTS system acquired data continuously for up to 6 months at a time, with occasional down time used for system maintenance and re-calibration. In this study, we analyze two uninterrupted parts of the dataset with lengths of 19 and 30 days acquired during winter and summer months respectively. We also analyze the river stage data collected at 1hr interval at ~1000 m from the IFRC area.

4.3.4 Time series and time-frequency analysis

Time series analysis of FO-DTS data first focused on assessment of the temperature along the cable at different times of the year to identify likely zones of enhanced

groundwater-surface water exchange. Time-series analysis was subsequently used to jointly interpret temperature time series and river stage time series in order to quantitatively evaluate how complex stage variations regulate exchange. Correlation coefficients were next calculated to evaluate the strength of the linear dependence between temperature and river stage time series for all spatial points along the river corridor.

A 1-D S-transform was then used to describe the frequency content of the temperature signals at selected locations along the cable, in order to identify the periodic features present over the time series. Finally, we applied a 2-D S-transform to the temperature time series to acquire the space localized spectral (wavenumber) information at selected frequencies of interest as identified by the 1-D S-transform [*Mansinha et. al.*, 1997b].

4.4 Results

We first examine temperature variations along the cable at times of low river stage in the time series when the groundwater discharge into the river is expected to be strongest, due to the increase in the groundwater head. Groundwater discharge zones (GDZ) are identified as areas with both anomalously warm temperature in winter (Figure 4.1b (2)) and anomalously cool temperature in the summer (Figure 4.1c (4)). Such anomalies are only visible at low river stage (Figure 4.1b (2) and 4.1c (4)) and diminish at high river stage (Figure 4.1b (1) and 4.1c (3)).

All S-Transform analysis was performed using Matlab codes provided by Dr.Mehrez Elwaeif (National Research Institute of Astronomy and Geophysics, Egypt).

The locations of the anomalies are consistent in both winter and summer data. See appendix B for seasonal and diurnal comparison of temperature variations along the cable.

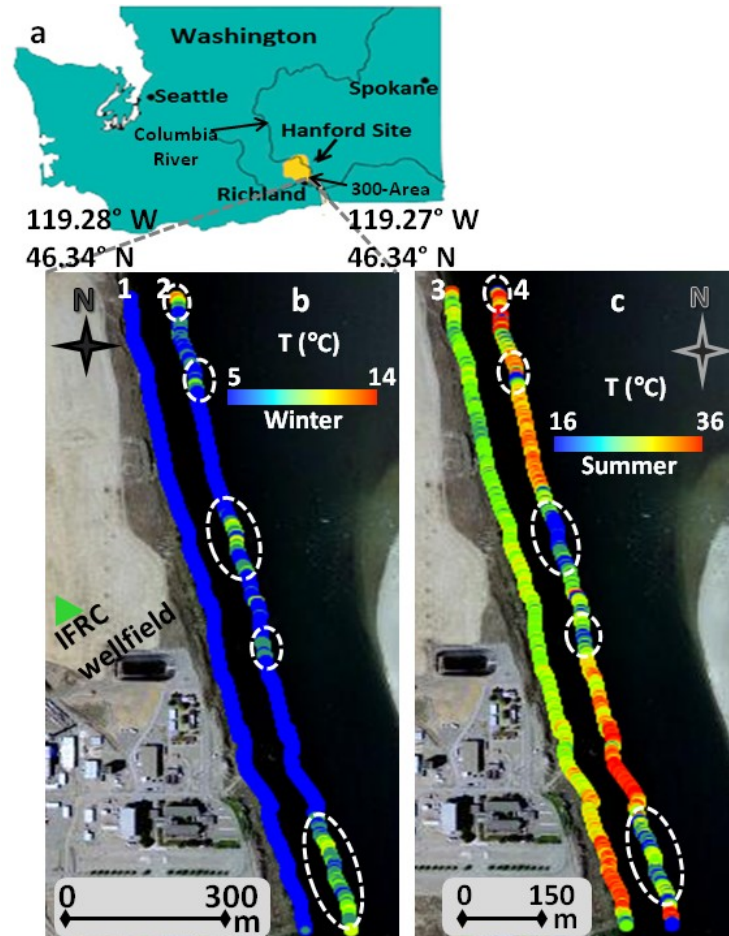


Figure 4.1 (a) Map of Washington State showing the location of Hanford Site in Richland, Washington, with the 300-Area located in the southeast. (b) Winter temperature distribution over 1.6 km of fiber-optic cable placed 2 m from shore, with the green triangle representing the IFRC wellfield area. (1) Temperature measurements at high river stage on 28 February 2009 (2) Temperature measurements at low river stage on 15 March 2009 (80 m offset for clarity). (c) Summer temperature distribution over the fiber-optic cable (3) Temperature measurements at high river stage on 20 August 2009 (4) Temperature measurements at low stage on 3 August 2009 (80 m offset for clarity). White dashed circles represent areas of focused groundwater - surface exchange. All color scales are linear.

Figure 4.2 presents the relation between river stage and temperature for an exchange and a non-exchange zone. These locations are selected for analysis based on their proximity to the IFRC area and the fact that the zone of focused exchange coincides with a known uranium spring (Spr-9, Figure 4.2d) [Williams *et al.*, 2007]. The time series in the non-exchange zone (Figure 4.2a) shows a temperature variation that is primarily driven by diurnal variation. Conversely, the temperature fluctuation in the GDZ (Figure 4.2b) shows a diurnal pattern with additional non-diurnal periods consistent with what might be inferred from the river stage data (Figure 4.2c). As expected, the difference in temperature is observed in Figure 4.2c when subtracting the temperature of the non-exchange zone from temperature of the exchange zone. The correlation coefficient between river stage and river water temperature along the cable provides more direct evidence of stage-controlled focused groundwater exchange along the river corridor. The temperature in the focused GDZ exhibits a weak negative correlation (~ -0.39 to -0.1) in the winter (Figure 4.2d (1 and 2)) and a strong positive correlation (~ -0.75 to 0.88) in the summer (Figure 4.2d (3 and 4)). Outside of the exchange zones, the correlation coefficient is relatively uniform, ~ 0.48 in the winter and ~ 0.7 in the summer. The sign of the correlation coefficient within GDZs is consistent with stage-driven groundwater discharge, as discussed below. Although there is a strong correlation outside of the GDZs, the sign of the correlation is inconsistent with stage-driven groundwater discharge and instead likely results from stage driven variations in the amount of summer solar heating of the water column. Although the correlation coefficient offers a simple way to represent the control of stage on focused groundwater exchange, the relatively weak correlation in the winter data (Figure 4.2d (2)), along with the fact that much of the cable

(away from the exchange locations) shows a strong correlation in the summer resulting from solar heating (Figure 4.2d (4)), raises the need for less ambiguous measures of the mechanisms controlling the exchange—hence our consideration of the S-transform.

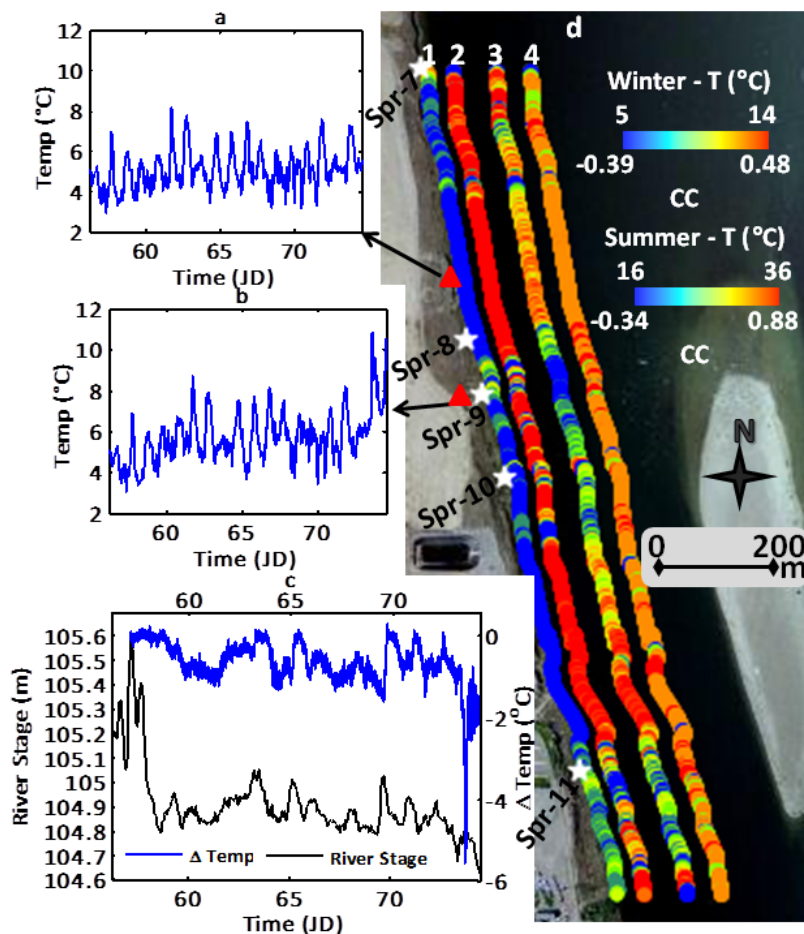


Figure 4.2 (a) Temperature distribution time series for an inferred non-exchange area. (b) Temperature distribution time series for a selected GDZ. (c) Interpolated river stage time series (black) and the difference in temperature between (b) and (c) (blue). (d) Analysis of the complete FO-DTS cable, with labels at top as follows: (1) temperature distribution for measurements at low stage on 15 March 2009; (2) correlation coefficient between temperature and river stage on 15 March 2009 (60 m offset); (3) temperature distribution for measurements at low stage on 3 August 2009 (130 m offset); and (4) correlation coefficient between temperature and river stage on 3 August 2009 (190 m offset). White stars represent known uranium seeps (Spr -7 – Spr-11) [Williams *et al.*, 2007]. Red triangles identify locations of time series for non-exchange versus exchange locations shown in (a) and (b), respectively. All color scales are linear; the top axis of the color bar is temperature, the bottom axis displays the correlation coefficient (CC): JD denotes Julian Day.

Figure 4.3 shows the 1-D S-transform results of the river stage time series (Figure 4.3a), selected GDZ (Figure 4.3b) and a nearby non-exchange location (Figure 4.3c) (triangles in Figure 4.2). Short periods of 0.5 and 1 day characteristic of diurnal temperature variations are present in both GDZ and non-exchange zones. These are the only strong periods in the non-exchange area. In contrast, the strong amplitudes at longer periods (2-16 days) in the temperature data from the exchange area correspond well with the strong amplitudes observed at the same periods in the river stage data (Figure 4.3a and 4.3b). These periods are weak (period 7-15 days) or absent (period 2-7 days) in the non-exchange area (Figure 4.3c). These periodicities are also apparent in the time-averaged normalized power spectra (Fourier Spectrum) plots shown to the right of the S-transforms in Figure 4.3.

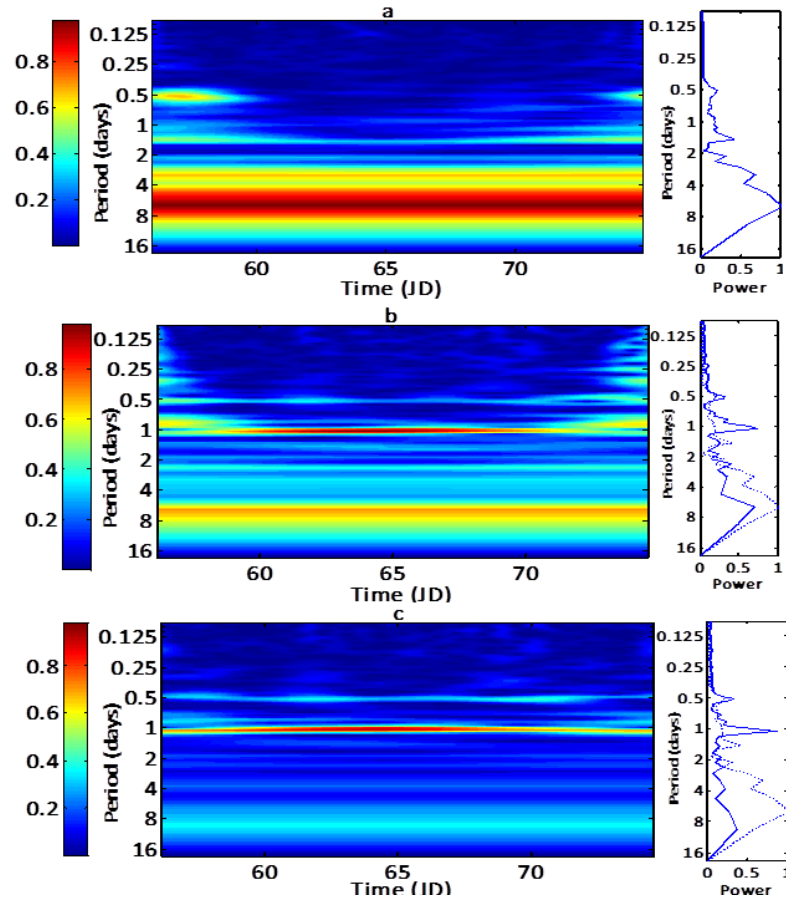


Figure 4.3 S-transform spectrum of time series for 19 days (27 February – 16 March 2009). (a) S-transform of the river stage time series. (b) S-transform of the FO-DTS time series from a GDZ. (c) S-transform of the FO-DTS time series from a non-exchange zone. Plots on the right of the S-transform images represent the time averaged normalized power spectra (equivalent to the FFT), wherein the dashed lines are the river stage time average for comparison. Color bars display amplitude (power) linearly.

The 2-D S-transform analysis of the entire FO-DTS dataset for three dominant periods (4, 1, and 0.5 day) identified in Figure 4.3 is shown in Figure 4.4b and 4.4c. The long-period behavior dominating the river stage (Figure 4.3a) is only evident in the zones of focused GDZ (Figure 4.4b (2)). Other locations along the cable exhibit low amplitudes of ≤ 0.1 for the 4 days period. In contrast, the diurnal variations marked by short periods (0.5 and 1 day) are evident along the entire cable length (Figure 4.4c (3 and 4)).

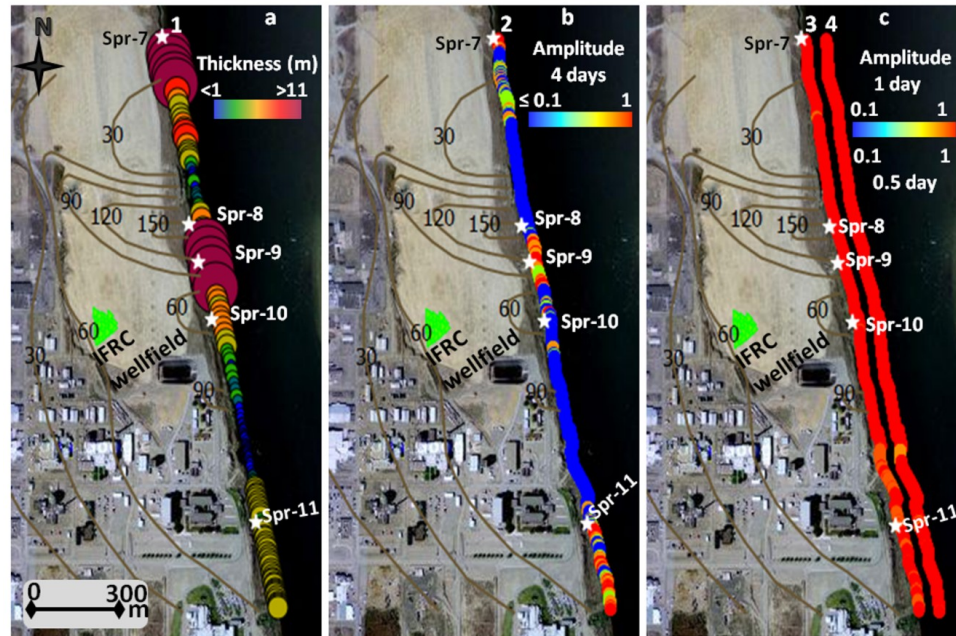


Figure 4.4 (a). (1) Hanford Formation thickness as estimated from continuous waterborne electrical imaging measurements [Slater *et al.*, 2010]. White stars represent uranium seeps (Spr -7 – Spr-11) [Williams *et al.*, 2007]. (b). (2) Amplitude of period 4 days. (c). (3) Amplitude of period 1 day and (4) Amplitude of period 0.5 day (60 m offset). Long periods shows strong signals in the exchange zones (thicker Hanford Formation), while I see effect of short periods (≤ 1 day) for the entire cable length. Brown contours on (a), (b) and (c) shows uranium concentration ($\mu\text{g/L}$) [Williams *et al.*, 2007]. All color scales are linear.

4.5 Discussion

FO-DTS of riverbed temperature along the Columbia River reveals the presence of focused groundwater exchange zones which likely facilitate the transfer of uranium contaminated water from the aquifer to the river. Five identified exchange zones coincide with known uranium springs reported by Williams *et al.* [2007]. The relatively similar temperature recorded in the GDZs ($\sim 13^{\circ}\text{C}$ in the winter and $\sim 15^{\circ}\text{C}$ in the summer) is consistent with groundwater discharge during low river stage, as groundwater is known to have relatively constant temperature. The correlation coefficient between temperature and river stage provides a semi-quantitative link between groundwater discharge and

river stage at the GDZs. The negative temperature-river stage correlation during winter results from discharge of warmer groundwater as the river stage falls. The positive temperature-river stage correlation during summer results from discharge of cooler water as the river stage falls. However, the high positive correlation between temperature and river stage in the non-exchange areas resulting from solar heating or seasonal changes highlights one limitation of relying solely on time series analysis of the stage-discharge relation for characterizing exchange. Furthermore, there are a few points on the cable where we see negative stage-discharge correlations in both the winter and summer data (Figure 4.2d (2) and (4)). These responses cannot be due to groundwater-surface water interaction.

Time-frequency analysis of the FO-DTS data identified a distinct difference in the dominant periods of the temperature time series for the GDZ compared to a non-exchange area. Only diurnal variations in the temperature time series, marked by short periods of 1 day and 0.5 day appear in both exchange and non-exchange locations. Comparison of the S-transform for the river stage time series with the temperature time series shows that long period signals (≥ 2 days) dominating river stage time series are only present at the GDZ location (Figure 4.3). We argue that the amplitudes of these periods characterizing the stage-time series provide a more reliable indication of active stage-driven groundwater discharge relative to analysis of the stage-temperature correlation.

The 2-D S-transform computed at these long periods (e.g. 4 days used here) captures information on spatial variability in the strength of the stage-driven groundwater discharge. High amplitudes at these long periods occur at locations along the river corridor (Figure 4.4b (2)) corresponding to thicker Hanford Formation deposits (Figure 4.4a (1)), possibly associated with buried channels incised into the Ringold Formation. Figure 4.4b (2) suggests that the zones of exchange may be more continuous than would be inferred using the stage-discharge correlation alone (Figure 4.2). A thicker Hanford Formation also coincides with the location close to the IFRC wellfield exhibiting high uranium concentration (Figure 4.4a) and identified GDZs (Figure 4.4b (2)). The known uranium seeps reported by *Williams et al.* [2007] (Figure 4.4a and 4.4b) all coincide with high amplitudes zones in the 4 days period of the temperature time series identified with the 2-D S-transform. This is in contrast to the stage-discharge correlation results. For example, whereas Spr-8 (Figure 4.2d) would be interpreted as a non-exchange zone in the stage-discharge correlation plot, the 2-D S-transform identifies Spr-8 as a GDZ (Figure 4.4a (1) and 4.4b (2)). We therefore argue that time-frequency analysis provides a more reliable indication of where exchange is occurring compared to the stage-discharge correlation or temperature at low stage alone. The S-transform analysis suggests that exchange is occurring more continuously along sections of the river corridor where the Hanford Formation is thickest. The 1-D S-transform analyses show that the long period signals related to groundwater-surface water exchange have a fairly uniform strength throughout the time series (unlike the 1 day and 0.5 day periods that are variable in strength). The variation in amplitude in 1 day and 0.5 day periods from 2-D S-transform analysis in Figure 4.4c) probably reflects variations in water depth and effect on solar

heating. The time-frequency approach also allows us to effectively filter out all such diurnal effects and focus our interpretation on features in the time series associated with the salient periodicity of stage.

4.6 Conclusions

We have demonstrated how the use of time-frequency analysis of FO-DTS time series can provide insights into the forcing mechanisms controlling groundwater-surface water exchange along a major river corridor. The time-frequency analysis using S-transform identified zones of contaminated groundwater discharge along a 1.6 km section of the Columbia River corridor and provided conclusive evidence of the stage-driven discharge associated with relatively long periods (≥ 2 days) in the river stage fluctuations. The correlation coefficient between river stage and temperature also identified spatial variability in exchange. However, linear correlation proved to be a less robust proxy indicator of groundwater discharge than the S-transform, as the river water temperature and hence correlation responds to variables other than the groundwater discharge alone. We conclude that time-frequency analysis is a powerful tool for improving understanding of dynamics of groundwater-surface water exchange from the spatially and temporally rich FO-DTS datasets.

CHAPTER 5

5. Statistical classification of spatial variation of groundwater discharge from DTS data³

Abstract

Fiber-optic distributed temperature sensing increasingly is used to map zones of enhanced groundwater/surface-water interaction (GWSWI). Previous efforts to infer GWSWI from FO-DTS data have relied on subjective interpretation of time-series statistics (e.g., variance), cross-correlation between temperature and stage, or spectral analysis of FO-DTS data. Commonly, classification of zones of enhanced GWSWI has been qualitative in nature with no rigorous selection of cutoffs on classification criteria (e.g., variance, correlation coefficient, or spectral power at a specific frequency) or evaluation of classification uncertainty (e.g., posterior probability). New approaches are needed to extract quantitative information from large, complex FO-DTS datasets while concurrently providing an assessment of uncertainty associated with this information. Here, we present a strategy combining discriminant analysis (DA) and spectral analysis (SA) to more objectively map zones of enhanced GWSWI while providing measures of classification uncertainty. The approach identifies a classification criterion (discriminant function) based on components of the spectral representations of FO-DTS time series.

³This chapter has been submitted as: Mwakanyamale, K., F. Day-Lewis and L. Slater, (*in review*), Statistical classification of spatial variation of groundwater discharge from DTS data. Submitted to *Water Resources Research*, September, 2012.

We demonstrate the approach using field experimental data from a reach of the Columbia River adjacent to the Hanford 300 Area site. We use geophysically estimated thickness of the permeable bed unit as training data for the classification. Results of the combined SA/DA approach are shown to be superior to previous results from qualitative interpretation of FO-DTS spectra.

5.1 Introduction

Interactions between groundwater and surface water occur at zones beneath and adjacent to surface water bodies. Mixing of groundwater and surface water plays an important role in hydrologic and ecological processes such as water-level fluctuations, stream/river discharge, transfer of contaminants, temperature regulation and nutrient cycling [*Hatch et al.*, 2006]. Groundwater may be a heat source or sink to the surface water depending on the season of the year, whereby heat is exchanged between the aquifer and the land surface. Temperature exchange across the groundwater/surface-water interface has been studied in detail for decades, with most studies focused on using temperature to quantify the amount of exchange [e.g. *Hatch et al.*, 2006; *Keery et al.*, 2007]. Spatial patterns of exchange also can be inferred qualitatively from temperature variations at the groundwater/surface-water interface (GWSWI) [e.g., *Selker et al.*, 2006b; *Lowry et al.*, 2007; *Slater et al.*, 2010; *Henderson et al.*, 2009; and *Mwakanyamale et al.*, 2012].

The development of fiber-optic distributed temperature sensing (FO-DTS) technology [*Selker et al.*, 2006a&b] has helped to increase the spatial and temporal coverage of temperature measurements. With spatial resolution as fine as 0.5 – 2 m and temporal

resolution of commonly 10 – 60 seconds, FO-DTS has provided insights into local-scale hydrological processes that were previously impossible to resolve with traditional temperature monitoring instruments [Tyler *et al.*, 2008]. Successful applications of FO-DTS in hydrological studies have been reported, especially in studies of GWSWI [e.g., Selker *et al.*, 2006b; Lowry *et al.*, 2007; Slater *et al.*, 2010; Henderson *et al.*, 2009; and Mwakanyamale *et al.*, 2012]. Previous efforts have demonstrated the information content of FO-DTS data for GWSWI, but relied on qualitative and subjective interpretation to map zones of enhanced GWSWI. A second, important limitation of past efforts is that they lacked evaluations of uncertainty associated with mapped zones.

Here, we present a strategy for objective mapping of zones of enhanced GWSWI and quantification of classification (in terms of exchange versus non-exchange zone) uncertainty. We combine discriminant analysis (DA) and spectral analysis (SA) using the discrete Fourier Transform (DFT). DA is a widely applied statistical technique in hydrological studies. Herrmann and Symader [1976], for example, reported on successful application of DA to predict phosphate load in streams. DA has also been applied to predict groundwater sources or mixing among aquifers [Steinhorst and Williams, 1985]. A recent groundwater application of DA focused on estimation of groundwater age [Daughney *et al.*, 2010]. SA of time series is also well established in hydrology, with applications ranging from catchment processes to fluvial processes.

Using a combination of SA and DA, we demonstrate development of a statistical rule for identifying zones of enhanced GWSWI along a reach of a major river. Our specific

objectives are to use a high resolution (in space and time) FO-DTS dataset to (1) objectively map exchange zones, and (2) quantify uncertainty of these classifications. We also assess how the selection of the periodic (or frequency) components (or their combinations) influences the effectiveness of the classification of zones of enhanced GWSWI.

5.2 Study Site

We demonstrate the combined SA/DA approach on a FO-DTS dataset acquired on the western bank of the Columbia River, along a reach adjacent to the Hanford 300 Area (Figure 5.1). From the 1940s to 1975, the 300-Area was used for nuclear fuel production and research and development. These processes resulted in contamination of the groundwater system. Groundwater discharges into the Columbia River (Figure 5.1b and 5.1c) through the zone of GWSWI along the 300-Area river corridor [*Peterson and Connelly, 2004; Fritz and Arntzen, 2007*]. This reach of the Columbia River experiences rapid stage fluctuations in response to operation of Priest Rapids Dam (upstream of the 300-Area) [*Arntzen et al., 2006*]. Consequently, flow reversals are common. River water flows into the aquifer as the river stage increases whereas groundwater discharges from the aquifer into the river as the river stage decreases. The area is underlain by an unconfined aquifer consisting of flood deposits of the Hanford Formation and fluvial deposits of the Ringold Formation. Riverbed permeability varies widely along the reach, with hydraulic conductivity values ranging from ~2000 m/d (Hanford Formation) to 40–120 m/d (Ringold Formation) [*Williams et al., 2007*].

The contact between the Hanford and Ringold Formations is believed to control the vertical transfer of groundwater at the 300-Area and the thickness of the Hanford Formation is considered a good indicator of exchange versus non-exchange locations, with enhanced exchange expected where the Hanford Formation is thickest [*Fritz and Arntzen, 2007*]. *Slater et al.* [2010] used waterborne electrical surveys to determine spatial variability in the depth to the Hanford-Ringold contact along the river corridor adjacent to the 300-Area; they also report on temperature anomalies from FO-DTS along this reach. *Mwakanyamale et al.* [2012] demonstrated how SA, in this case based on S-transform, better discriminated likely exchange zones (relative to temperature anomalies alone) and also provided information on the hydrological controls on exchange. GWSWI was found to have a distinct spectral signature in FO-DTS data and to coincide with locations along the river where the Hanford-Ringold contact is predicted to be locally deeper (i.e. thicker Hanford Formation) in electrical images [*Slater et al., 2010; Mwakanyamale et al., 2012*]. Here, we further capitalize on the distinct spectral signature of GWSWI in FO-DTS data identified qualitatively by *Mwakanyamale et al.* [2012].

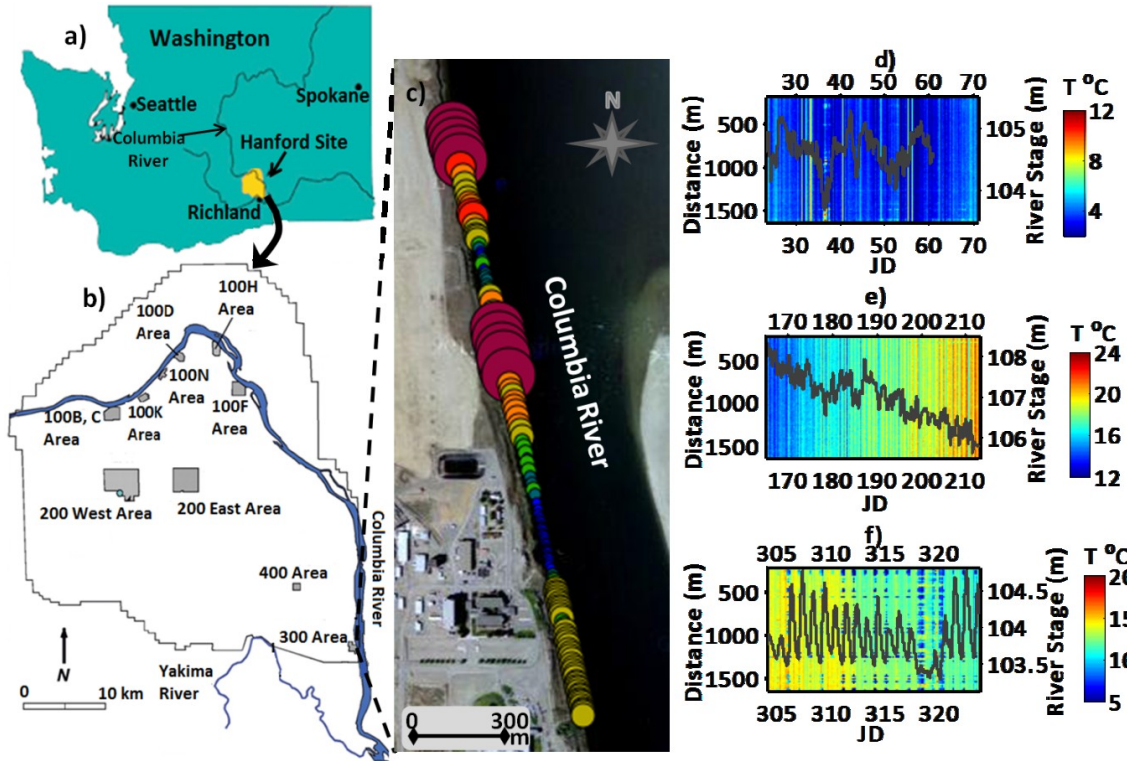


Figure 5.1 (a) Map of Washington State showing the location of Hanford site in Richland, Washington. (b) Map of Hanford site showing the location of the 300 Area in the south east. (c) Hanford Formation thickness as estimated from continuous waterborne electrical imaging measurements [Slater *et al.*, 2010]. The fiber-optic cable was placed at 2 m from shore along the same location as the Hanford Formation thickness. Temperature time series superimposed on the Columbia River stage time series (d) January 24, 2011 – March 4, 2011 (e) June 15, 2011 – August 1, 2011 (f) November 1, 2010 – November 22, 2010. JD stands for Julian Day. All color scales are linear.

5.3 Methods

5.3.1 Fiber-Optic Distributed Temperature Sensing

FO-DTS offers a means to continuously measure temperature at high spatial and temporal resolution. The FO-DTS method relies on backscattering of a laser pulse along a fiber optic cable to determine temperature at a particular distance along the fiber [Selker *et al.*, 2006b, Selker *et al.*, 2006a]. The ratio of the anti-Stokes amplitude to the Stokes amplitude in Raman backscatter provides temperature measurements everywhere along the cable [Selker *et al.*, 2006a, 2006b]. The location of the temperature measurement

along the fiber optic cable is estimated using optical time-domain reflectometry, based on time of flight of the incident light and scattered light [Selker *et al.*, 2006a].

5.3.2 Spectral Analysis

The fast fourier transform (FFT) is an efficient tool for computing the discrete fourier transform (DFT) of a time series [Cochran *et al.*, 1967]. The DFT is defined as

$$X^F(k) = \sum_{n=0}^{N-1} x(n)W_N^{kn}, \quad \text{and} \quad (5.1)$$

$$W_N^{kn} = \exp\left[\left(\frac{-j2\pi}{N}\right)kn\right], \quad (5.2)$$

where N denotes the sample number; $x(n)$ is a uniformly sampled time series ($n = 0, 1, \dots, N-1$); $j = \sqrt{-1}$; and $X^F(k)$ is the k -th DFT coefficient ($k = 0, 1, \dots, N-1$) [Cooley and Tukey, 1965]. We use the FFT algorithm to decompose the temperature time-series signals into components of different frequencies/periods. Although we used time-frequency analysis (S-transform) in previous work [Mwakanyamale *et al.*, 2012], here we independently analyze short intervals of data, for which stationarity can be assumed, thus obviating more complicated time-frequency analysis for the demonstration here. We stress, however, that DA also could be combined with time-frequency SA.

5.3.3 Discriminant Analysis

Discriminant analysis [Fisher, 1936] is a powerful statistical tool used for multivariate classification problems. DA generates a set of classification functions to predict the category an observation belongs to. This prediction is based on a combination of input variables [Daughney *et al.*, 2010]. Each observation is classified into the group for which the probability of belonging is the greatest. The effectiveness of the computed functions

is quantified as the posterior probability (P). As defined by *Hung et. al.* [1996], this is the probability that a predicted class (x) belongs to a prior defined group (j):

$$P(w_j|x) = \frac{f(x,w_j)}{f(x)}, \quad (5.3)$$

$$f(x, w_j) = f(x|w_j)P(w_j),$$

$$f(x) = \sum_{j=1}^m f(x, w_j),$$

where w_j denotes the fact that x is a member of j ; m is the number of groups; $P(w_j)$, is the prior probability of group j ; and $f(x, w_j)$ is the conditional probability density function for x being a member of j . Discriminant functions are functions of the posterior probabilities [*Hung et. al.*, 1996]. The discriminant function for the quadratic discriminant analysis, used here, is

$$g_{ij}(x) = -\frac{1}{2}(x - \mu_i)^t \Sigma_i^{-1} (x - \mu_i) + \frac{1}{2} (x - \mu_j)^t \Sigma_j^{-1} (x - \mu_j) + \ln \frac{P(w_j)}{P(w_i)} \quad (5.4),$$

where, Σ is a covariance matrix; μ is the mean vector; and superscript t denotes the matrix transpose [*Hung et. al.*, 1996]. Here, we summarize classification success as a hardness (H) value [*Deutsch and Journal*, 1998, p. 86]. For our binary classification problem, H is the probability of assignment to class 1 given an observation correctly belongs to class 1 (correct positive classification), minus the probability of assignment to class 1 given an observation belongs to class 0 (false negative classification); thus, $H=1$ would correspond to the case of perfect classification of all zones of enhanced GSWSI.

We use DA to classify exchange vs. non-exchange zones along the FO-DTS cable, with input as the amplitudes of different periods from spectral analysis of FO-DTS data and as training data the thickness of the Hanford Formation as previously determined by boat-

towed electrical surveys [Slater *et al.*, 2010]. The approach presented (1) uses information from the SA to support classification (information from multiple frequency components), (2) is more objective than past work in that it relies on the DA to identify the classification rule, rather than subjective visual inspection, and (3) provides a measure of prediction uncertainty, quantified in a spatially distributed manner as posterior probability and subsequently summarized in terms of hardness. Ideally, training data would come in the form of direct measurements of seepage; however, spatially exhaustive seepage measurements are unavailable and impractical to collect given the difficulty and expense of installation of probes in the cobble-armored riverbed. Instead, we use electrically estimated Hanford Formation thickness.

5.3.4 Data Acquisition

A 1.6 km long ruggedized SensorNet EnviroFlex fiber optic cable (~1 cm diameter) with two 50-micron multimode fibers was installed below the water surface at ~2 m from the Columbia River bank, and about 0.15 to 0.76 m deep, along the location of the Hanford Formation thickness (Figure 5.1c) (note that any use of trade, product, or firm names is for descriptive purposes only and does not imply endorsement by the U.S. Government). The cable was installed 2 m from the river bank to capture the connectivity between the aquifer and the river. The cable remained secured on the streambed (underwater) by the use of large cobbles and/or breeze-blocks.

The riverbed temperature was recorded by a Sontaran 8-channel Gemini control unit at 5 minute intervals for every 0.51 m along the cable length (for a total of 2871

measurement locations). The FO-DTS system acquired data from November 2008 – January 2012 with occasional down time used for system maintenance and re-calibration. The river stage data was collected at 1 hour intervals by a probe stationed upstream of 300-Area. We analyze 3 uninterrupted parts of the dataset ranging from 17 to 48 days acquired during winter, summer and fall months. Although most results presented here are from winter and summer, analysis was done for all three seasons (see Appendix C).

5.3.5 Data Analysis

The FFT was used to analyze the frequency content of the FO-DTS data at different times of the year (winter (38 days), summer (48 days) and fall (22 days)) in order to identify the periodic features in the time series. The datasets have variable durations due to interruptions for maintenance and recalibration of the FO-DTS system. Amplitudes of selected periods (0.5, 1, 3, 4, 6 and 8 days) obtained from FFT were used as inputs in the DA. These periods were chosen as they demonstrate high amplitude in the sampling seasons [Mwakanyamale *et. al.*, 2012]. To classify spatial points of different amplitudes as exchange or non-exchange zones, the thickness of the Hanford Formation estimated by Slater *et.al.* [2010] was used as a grouping variable for training data. Using a threshold of 5 m all the spatial points along the river corridor were categorized as either exchange or non-exchange zones. All the locations with thickness ≥ 5 m were defined as exchange zones, whereas, locations with thickness of < 5 m were identified as non-exchange zones. DA was performed for the following combinations of data (1) all periods (0.5 – 8 days) for individual sampling seasons, (2) 4-day period only, for different sampling seasons, and (3) all periods (0.5 – 8 days) for all sampling seasons. Comparing results for these

three analyses yields insights into the effectiveness of the SA/DA approach for combining information across frequencies and seasons. In addition, it provides a test of the validity of focusing on the 4-day period as the most informative of GWSI zones in this dataset in previous work [Mwakanyamale *et al*, 2012]. Use of a single frequency component might neglect important information available from consideration of multiple frequencies.

5.4 Results

Figure 5.1 shows riverbed water temperature and river stage of three subsets of the FODTS data collected on cable 1 in January – March 2011 (Figure 5.1d), June - August 2011 (Figure 5.1e) and November 2010 (Figure 5.1f). The temperature time series exhibit evidence of temperature anomalies in winter (Figure 5.1d), and fall (Figure 5.1f) that correspond well to decreases in river stage.

The FFT analysis results exhibit distinct spatial and temporal patterns in different sampling seasons (Figure 5.2). Higher amplitudes at longer periods are seen for some locations along the cable length. Long periods of 3, 4, and 6 days exhibit strong amplitude in the winter data (Figure 5.2c, 5.2d & 5.2e, blue lines), and these strong amplitudes coincide with the locations of thicker Hanford Formation (≥ 5 m) (Figure 5.2g). Short periods of 0.5 and 1 day (Figure 5.2a & 5.2b, blue lines) show weaker amplitudes in the discharge zones while exhibiting similar amplitudes to the longer periods at the other locations along the cable.

The distribution of amplitudes in the summer FFT analysis results (Figure 5.2, black lines) is in contrast to what was observed in the winter data (Figure 5.2, blue lines). Only one long period shows strong amplitudes in all the locations projected to be groundwater exchange zones based on the Hanford Formation thickness (Figure 5.2e, black line). All long periods, 3 - 8 days (Figure 5.2c – 5.2f, black lines) show high amplitudes at cable length 220 m -380 m. This location is also identified as a discharge zone. Short periods of 0.5 and 1 day in the summer data (Figure 5.2a & 5.2b, black lines), show stronger amplitudes than what was observed in winter results. The FFT analysis results from the fall season (see Appendix C) exhibit amplitudes that are in contrast to all other sampling seasons (winter and summer). Unlike in winter and summer, we see strong amplitudes at most locations along the cable for all periods (0.5 – 8 days). We note that in fall the surface and groundwater temperatures converge, rendering fall (or spring, presumably) data less informative than summer or winter, when temperature contrasts are optimal for interpreting GWSWI.

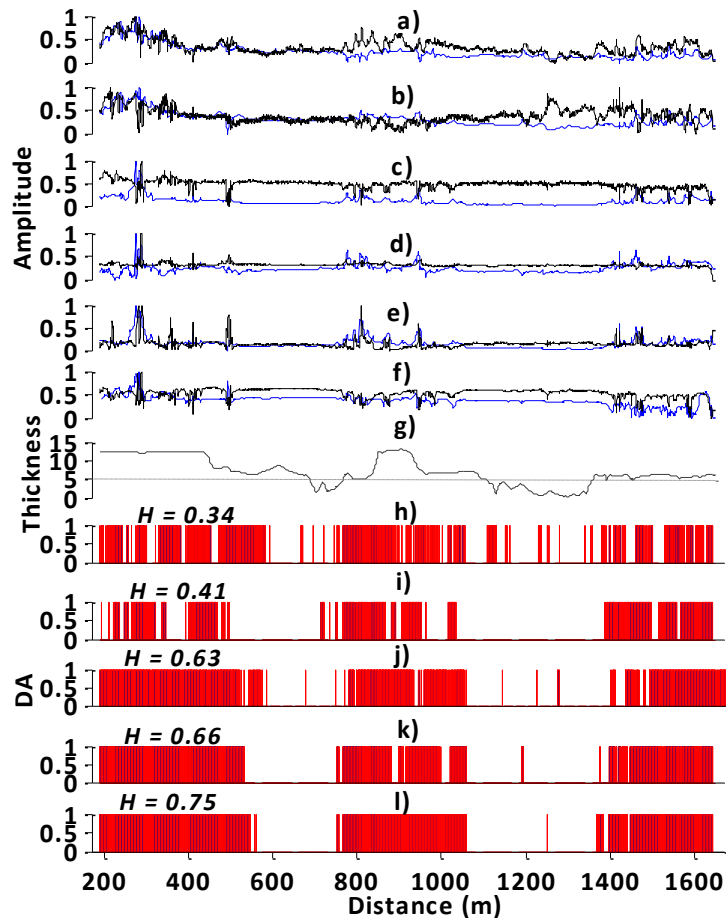


Figure 5.2 FFT results for winter data (January – March) (blue lines) and for summer data (June – August) (black lines) (a) normalized amplitude of period 0.5 day (b) normalized amplitude of period 1 day (c) normalized amplitude of period 3 days (d) normalized amplitude of period 4 days (e) normalized amplitude of period 6 days (f) normalized amplitude of period 8 days (g) Hanford Formation thickness as estimated from continuous waterborne electrical imaging measurements [Slater *et al.*, 2010]. The gray dashed line indicates the 5 m threshold used as a cut-off for identifying exchange vs. non-exchange zones. DA classification results for winter and summer data. The red bars indicate areas classified as groundwater exchange zones (h) DA results using amplitude from period 4 days in the summer (i) DA results using amplitude from period 4 days in the winter (j) DA results using amplitudes from all periods in the summer (k) DA results using amplitudes from all periods in the winter (l) DA results using all amplitudes of all periods from all sampling seasons.

The DA classification results are presented in Figures 5.2h and 5.2j (summer data), Figures 5.2i and 5.2k (winter data) and Figure 5.2l (all seasons). The effectiveness of the DA function is presented by the hardness (H) criteria. For the winter data (all periods), H

was ~66% (0.66), hence 66% of classifications were correct. Figure 5.2k shows the identified exchange sites which are in alignment with the thicker Hanford Formation and the locations with higher amplitudes at the longer periods. The summer classification (all periods) performance is similar to the winter classification performance with ~63% (0.63) H (Figure 5.2j). There are new erroneously classified exchange sites in the summer data (Figure 5.2j) that were classified as non-exchange sites in the winter data (Figure 5.2k). Notably, more sites are misclassified by the DA function in the fall sampling season (Appendix C). The H for fall DA classification was only ~49% (0.49), ~16% less than the winter classification. The use of a single frequency for DA classification is thus less effective than use of multiple frequencies. Classification using amplitudes from only the 4-day period performed poorly, for both summer (Figure 5.2h) and winter (Figure 5.2i) data, producing H values of ~34% (0.34) and ~41% (0.41), respectively. Application of the DA to a combined dataset including all periods from all sampling seasons, provided the best classification (Figure 5.2l), with H of ~75% (0.75). The SA/DA approach thus uses combinations of frequency components to give a superior classification than possible using only a single frequency component.

The DA results are displayed as maps in Figure 5.3. The locations of the classified groups from DA (exchange vs. non-exchange zones) correspond well with Hanford Formation thickness. For each classification, the DA provides a measure of classification uncertainty in the form of posterior probability (P), shown in Figure 5.3 as the probability of correct classification. Considering only fall data and a single frequency (4-day period), the SA/DA produces classifications with low confidence, such that only ~20% of the sites

are classified with 90 - 100% certainty (Appendix C). The use of single frequency for classification with winter and summer data result in classification certainties ranging from 50% - ~70% (Figure 5.3a&5.3b). Using summer data (all periods), ~90% of the sites were classified with certainty of 90 - 100% (Figure 5.3c), whereas, using winter data (all periods), ~95% of the sites were classified with certainty of 90 - 100% (Figure 5.3d). The best classification results from considering data for all periods from all sampling seasons (Figure 5.3e), for which 98% of the sites are classified with 90-100% confidence. The SA/DA approach effectively combines data across frequency and time and is not adversely affected by inclusion of low quality data from seasons with unfavorable conditions (e.g., fall).

The use of spatially exhaustive IP-estimated thickness as training data allows us to evaluate the data requirements for our SA/DA approach. Down-sampling the co-located IP-thickness/FO-DTS spectral data to 10% for training (i.e., construction of the discriminant function) and then performing classification for all FO-DTS locations, results in a classification almost identical to that developed with the full dataset, with only negligible change to H . Retaining only 5% of data for training and then discriminating everywhere results in a classification with $H=0.67$. These results indicate that, at least for our study area and dataset, the SA/DA approach produces a classification that is robust and stable when developed based on limited data.

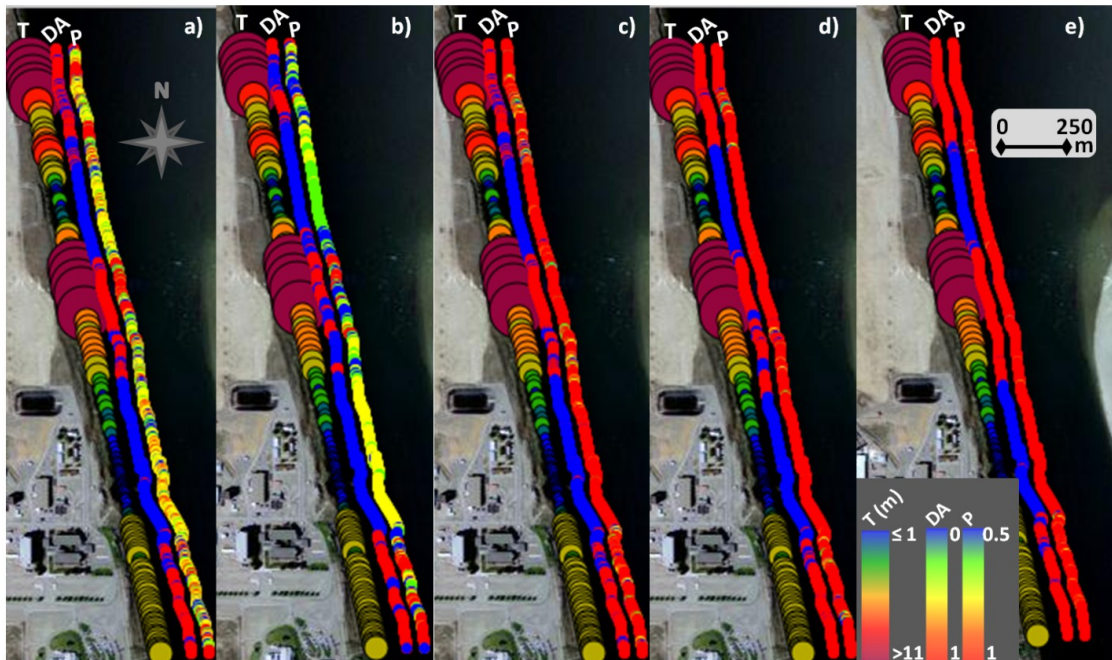


Figure 5.3 Map view of; Hanford Formation thickness (T) as estimated from continuous waterborne electrical imaging measurements [Slater et al., 2010], DA results and posterior probability (P) of DA classification. (a) single amplitude of period 4 days from summer data (b) single amplitude of period 4 days from winter data (c) all amplitudes of all periods in the summer (d) all amplitudes of all periods in the winter (e) all amplitudes of all periods from all sampling seasons. All color scales are linear.

5.5 Discussion and Conclusions

Extracting information from large FO-DTS datasets is challenging, and new approaches are needed to map zones of enhanced GWSWI objectively while providing assessments of classification uncertainty. Whereas past work [Henderson et al., 2009; Mwakanyamale et al., 2012] relied on subjective selection of a single spectral component as an indicator of exchange, here we have combined DA and SA to capitalize more fully and objectively on the information content of FO-DTS data; this combination proved an effective strategy to classify exchange vs. non exchange sites using FO-DTS time-series data and training data in the form of bed thickness. Although we used the Hanford Formation thickness as the training data in this study, more concrete training data e.g. locations of known

seepage flux measurements, could equally be used if available. The results obtained by DA show a clear distinction between groundwater exchange and non-exchange zones. Our results showed that classification combining information from multiple frequencies over multiple seasons provided results superior to those derived from a single frequency component of the FO-DTS power spectrum from a single season. Although analysis of autumn data provided poor results, as expected given the low groundwater/surface-water temperature contrast in autumn, the inclusion of autumn data did not adversely affect the SA/DA results. Indeed, the SA/DA approach proved to be most effective when considering amplitudes from all periods at all sampling seasons. In addition to providing superior classifications compared to past work, our approach also provides a quantitative measure of classification uncertainty. The SA/DA approach was shown to be robust when developed from down-sampled training data, at least for the Hanford 300-Area. This finding underscores the effectiveness of the SA/DA approach with limited training data, and thus points to the potential consideration of direct seepage measurements with sparse spatial distribution for training.

CHAPTER 6

6.0 Conclusion

6.1 General Conclusion

This research explore the use of electrical geophysical imaging in combination with fiber optic distributed temperature sensor (FO-DTS), to improve the understanding of the hydrological framework for how groundwater/surface water interactions regulates solute transport between the contaminated aquifer and the Columbia River at the Hanford site 300-Area. This work also examine how fluctuations in river stage driven by dam operations impact variation in the water table elevation and hence groundwater discharge into the river. Using the two methods mentioned above, this work provide information on the spatial variation of elevation of the Hanford-Ringold contact in the vicinity of the 300-Area and spatial distribution of the groundwater discharge zones along the Columbia River corridor at the 300-Area.

Chapter 3 explore the use of conductivity and induced polarization methods to understand the variation in depth to the Hanford-Ringold contact at the 300-Area and its control on the vertical migration of groundwater into surface water of the Columbia River. A 2D complex conductivity inversion was utilized to image subsurface distribution of complex conductivity across the site, from which the spatial distribution of the key hydrogeologic units at the 300-Area was reconstructed. Synthetic studies were carried out to investigate the effects of noise on the resolution of conductivity and IP images and to add confidence to the interpretation of lithology from the field datasets. Variation in the elevation of this contact provides evidence of a depression in the Hanford-Ringold contact connecting the

aquifer and the Columbia River. This finding demonstrates how field-scale conductivity and induced polarization measurements can be used in the interpretation of lithological structure.

Chapter 4 and 5 exploits the natural contrast in temperature between groundwater and surface water along with hourly river stage fluctuations, to map groundwater discharge zones along the Columbia River corridor. Time series and spectral analysis in conjunction with statistical analysis of the FO-DTS data and synchronized river stage data yielded new insights into the dynamics of groundwater-surface water interaction. Time series analysis of the temperature data together with the river stage data highlights the control of the river stage fluctuation on the discharge of groundwater, and hence helped to identify areas of enhanced groundwater exchange along the river corridor. Time-frequency analysis of the temperature time series and correlation with river stage time series helped to point out variables controlling the river stage fluctuations and hence the exchange between groundwater and surface water at the 300 Area. Daily dam operations were identified as a factor controlling stage fluctuations and hence groundwater discharge at high amplitudes of 0.4 – 0.8 for long periods (4 – 8 days).

Integration of spectral analysis and statistical analysis allows a detailed mapping of the discharge zones and assigning uncertainty associated with the mapping. Hanford Formation thickness together with the amplitudes identified from spectral analysis was used as input in statistical analysis to classify the exchange vs. non-exchange zones, in

this we also looked at the optimum frequency/amplitude that gives the best classification results.

6.2 Implication for 300-Area Hydrological Framework

Combined interpretation of electrical and DTS datasets helped to identify areas of focused groundwater exchange at very high spatiotemporal resolution. The areas of focused groundwater exchange coincide with the mapped depression in the complex conductivity results. This work demonstrates how integration of geophysical methods can be used to characterize the hydrogeological systems at unique spatiotemporal scales unachievable without geophysics.

It has also been demonstrated how rapid river stage fluctuation controlled by hydroelectric dam operations in a large river results in daily variations of groundwater discharge from a contaminated aquifer. As the river stage decreases there are an immediate impact on the riverbed temperature due to groundwater input. FODTS monitored temperature patterns in different seasons revealed distinct discharge locations on the streambed. Spatial repeatability of the temperature anomalies and the strength of the correlation coefficient on the riverbed at different sampling period confirmed the presence of discharge zones. This also implies the possibility of direct transfer of uranium from aquifer into the river. While the results shown here are qualitative in nature, they provide information that could help constrain locations for further investigations. Rapid river stage changes of large magnitude allows groundwater-surface water interactions to

be studied on a scale of days, providing high resolution information for defining the boundary conditions for flow and transport in the aquifer.

6.3 Recommendations

This study provides information on lithology and groundwater/surface water exchange across the 300 area. The approach focused on extracting the signatures of riverbed temperature and the river stage fluctuation to infer the interactions between groundwater and surface water. This information can be used as input to assist in improving the representation of the hydrologic framework within flow and transport models developed for this site. The spatial variation to the depth of the Hanford-Ringold interface provided in this study can also be incorporated to the site wide geologic model. As this work concentrated on the location between IFRC wellfield and the Columbia River corridor, additional geophysical mapping is suggested to cover the entire 300- Area, especially the landward portion, in order to map the continuity of the depth to the H-R contact.

The spatiotemporally rich datasets acquired in this project provide opportunities for future research. The results presented strongly encourage further geophysical and hydrological characterization and monitoring work at the 300 Area. For example, the inferred discharge zones could be used to quantitatively estimate groundwater flux e.g. using vertical (1D) temperature measurements. Further information on the distribution of depressions in the H-R contact would help to better constrain preferential flow/transport

at the site. Resistivity/IP mapping further inland could address primary questions regarding the extent of the zone of groundwater/surface water interactions.

The consistency of the information obtained from the different methods and analyses used in this study, combined with the agreement against ground-truth information where available (e.g. location of uranium seeps and boreholes) provides confidence in the interpretation of the datasets. Hence, it is appropriate to suggest that integration of resistivity/IP mapping and FO-DTS monitoring could be employed at other sites where groundwater/surface water interaction exerts a control on contaminant flow and transport.

REFERENCES

Alley, W. M., R. W. Healy, J. W. LaBaugh and T. E. Reilly (2002), Flow and storage in groundwater systems, *Science*, **296**.

Archie, G. E. (1942), The electrical resistivity log as an aid in determining some reservoir characteristics: Transactions of the American Institute of Mineral, Metallurgy and Petroleum Engineers, **146**, 54–62.

Arntzen, E. V., D. R. Geist, and P. E. Dresel (2006), Effects of fluctuating river flow on groundwater/surface water mixing in the hyporheic zone of a regulated, large cobble bed river, *River Research and Applications*, **22**(8), 937-946,

Bechert, C. H., J. M. Heckard (1966), Ground Water, *in* Natural Features of Indiana, 1816-1966: Sequacentennial Volume, Indiana Academy of Science, Indianapolis, IN. 100–115.

Binley, A. and A. Kemna, (2005), DC resistivity and induced polarization methods, in: Rubin, Y., Hubbard, S. (Eds.), Hydrogeophysics, Springer, **129**.

Biskey, T.M., and E.D. Gross (2001), The hyporheic zone: Linking groundwater and surface water-understanding the paradigm, *Remediation: The Journal of Environmental Cleanup Costs, Technologies, and Techniques*, **12**, 55-62.

Bjornstad, B. N., D.C. Lanigan, J.A. Horner, P.D. Thorne, and V.R. Vermeul (2009), Borehole completion and conceptual hydrogeologic model for the IFRC wellfield, 300 Area, Hanford site, Integrated Field Research Challenge Project, Prepared for the U.S. Department of Energy Office of Biological and Environmental Research under Contract DE-AC05-76RL01830, PNNL-18340, Pacific Northwest National Laboratory, Richland, Washington, 99352.

Börner, F. D., J. R. Schopper, and A., Weller, (1996), Evaluation of transport and storage properties in the soil and groundwater zone from induced polarization measurements: Geophysical Prospecting, **44**, 583–602.

Cochran, W.T., J.W. Cooley, D.L. Favon, H.D. Helms, R.A. Kaenel, W.W. Lang, G.C. Maling, D.E. Nelson, C.M. Rader and P.D. Welch (1967), What is the Fast Fourier Transform? IEEE Trans. Audio and Electroacoustics, **15** (2), 45-55.

Constantz, J., L. C. Thomas, and G. Zellweger (1994), Influence of diurnal variations in stream temperature on streamflow loss and groundwater recharge, *Water Resources Research*, **30** (12), , 3253-3264.

Collett, L. S. and T. J. Katsube, (1973), Electrical parameters of rocks in developing geophysical techniques, *Geophysics*, **38** (1), 76.

Commer, M., G. A. Newman, K. H. Williams, and S. S. Hubbard (2011), 3D induced-polarization data inversion for complex resistivity, *Geophysics*, **76** (3), 10.1190/1.3560156.

Cooley, J. W. and J. W. Tukey (1965), An algorithm for the machine calculation of complex Fourier series. *Math. Comput.* **19**:297-301.

Cooley, W.W. and P. R. Lohnes (1971), *Multivariate Data Analysis*, John Wiley & Sons.

Cosenza, P., A. Ghorbani, C. Camerlynck, F. Rejiba, R. Guérin and A. Tabbagh (2009), Effective medium theories for modelling the relationships between electromagnetic properties and hydrological variables in geomaterials: a review: *Near Surface Geophysics*, **7**, 563-578

Dahlin, T., V. Leroux, and J. Nissen, (2002), Measuring techniques in induced polarisation imaging, *Journal of Applied Geophysics*, **50**, 279– 298.

Dahlin, T. and M. H. Loke, (1998), Resolution of 2D Wenner resistivity imaging as assessed by numerical modeling, *Journal of Applied Geophysics*, **38**, 237-249.

Daughney, C. J., U. Morgenstern, R. van der Raaij and R. R. Reeves (2010), Discriminant analysis for estimation of groundwater age from hydrochemistry and well construction: application to New Zealand aquifers, *Hydrogeology Journal*, **18**, 417–428, DOI 10.1007/s10040-009-0479-2

Day-Lewis, F. D., K. Singha, and A. M. Binley, (2005), Applying petrophysical models to radar travel time and electrical resistivity tomograms: Resolution-dependent limitations, *Journal of Geophysical Research*, **110**, doi: 10.1029/2004JB003569.

de Lima, O.A.L. and Sri Niwas, (2000), Estimation of hydraulic parameters of shaly sandstone aquifers from geoelectrical measurements, *Journal of Hydrology*, **235**, 12.

Dennison, D. I., D. R. Sherwood and J. S. Young, (1989), Status Report on Remedial Investigation of the 300 Area Process Ponds, Prepared for the U.S. Department of Energy under contract DE-AC06-76RLO 1830, Pacific Northwest Laboratory, Operated for the U.S. Department of Energy, by Battelle Memorial Institute.

Deutsch, C. V., and A. G. Journel, (1998): *GSLIB: Geostatistical Software Library and Users Guide*, Oxford University Press, New York, Second Edition, 369 p.

DOE/RL-2010-99, Internal Draft, (2011), 300 Area Remedial Investigation/Feasibility Study Report for the 300-FF-1, 300-FF-2, and 300-FF-5 Operable Units, Prepared by CH2M-Hill Plateau Remediation Company for the U.S. Department of Energy, Richland, Washington.

Fisher, R.A., (1936), The use of multiple measurements in taxonomic problems, *Annals of Eugenics*, **7**, 179-188.

Freshley, M. D. (2008), 300 Area Integrated Field-Scale Subsurface Research Challenge (IFRC) Field Site Management Plan, PNNL-17067 Rev. 2, Pacific Northwest National Laboratory, Richland, Washington 99352

Fritz, B. G. and E. V. Arntzen, (2007), Effect of rapidly changing river stage on uranium flux through the Hyporheic Zone: *Ground Water*, **45** (6), 753–760.

Fritz, B. G., R. D. Mackley, N. P. Kohn, G. W. Patton, T. J. Gilmore, D. P. Mendoza, D. McFarland, A. L. Bunn, and E. V. Arntzen, (2007), Investigation of the hyporheic zone at the 300 Area, Hanford site, PNNL-16805, Pacific Northwest National Laboratory, Richland, Washington.

Ginzburg, A. and A. Levanon (1976), Determination of a saltwater interface by electric resistivity depth soundings, *Hydrogeological Sciences*, **21**, 561-568.

Hartman, M. J., L. F. Morasch, and W. D. Webber (eds.) (2006), Hanford Site Groundwater Monitoring for Fiscal Year 2005. PNNL-15670, Pacific Northwest National Laboratory, Richland, Washington.

Hatch, C. E., A. T. Fisher, J. S. Revenaugh, J. Constantz, and C. Ruehl (2006), Quantifying surface water–groundwater interactions using time series analysis of streambed thermal records: Method development, *Water Resources Research*, **42** (10), 1-14, doi:10.1029/2005WR004787.

Henderson, R. D., F. D. Day-Lewis, and C. F. Harvey (2009), Investigation of aquifer-estuary interaction using wavelet analysis of fiber-optic temperature data, *Geophysical Research Letters*, **36** (6), 1-6, doi:10.1029/2008GL036926.

Herrmann, R. and W. Symader (1976), Phosphate prediction model for streams by means of Discriminant analysis, *Hydrological Sciences Bulletin*, **21** (3), 397-406, doi.org/10.1080/02626667609491648.

Jackson, P. D., D. Taylor Smiths, and P. N. Stanford (1978), Resistivity-porosity-particle shape relationships for marine sands, *Geophysics*, **43** (b), 1250-1268.

Keery, J., a Binley, N. Crook, and J. Smith (2007), Temporal and spatial variability of groundwater–surface water fluxes: Development and application of an analytical method using temperature time series, *Journal of Hydrology*, **336** (1-2), 1-16, doi:10.1016/j.jhydrol.2006.12.003.

Kemna, A. (2000), Tomographic inversion of complex resistivity - Theory and application, PhD Thesis, Bochum Ruhr- University, Germany (published by: Der Andere Verlag, Osnabrück, Germany).

Kemna, A., A. Binley, and L. Slater (2004), Crosshole IP imaging for engineering and environmental applications: *Geophysics*, **69** (1), 97, doi: 10.1190/1.1649379.

Kemna, A., E. Räckers, and A. Binley, (1997), Application of complex resistivity tomography to field data from a kerosene-contaminated site: *Environmental and Engineering Geophysics (EEGS) European Section*, 151-154.

Klein, J. D., and W. R. Silli (1982), Short Note, Electrical properties of artificial clay-bearing sandstone: *Geophysics*, **47**(11), 1593.

Koestel, J., A. Kemna, M. Javaux, A. Binley, and H.Vereecken (2008), Quantitative imaging of solute transport in an unsaturated and undisturbed soil monolith

with 3-D ERT and TDR: *Water Resources Research*, **44** (12) 1, doi:10.1029/2007WR006755.

Kunk , J. R., S. M. Narbutovskih (1993), Phase I summary of surface geophysical studies in the 300-FF-5 operable unit. Richland, WA, Westinghouse Hanford Company.

LaBrecque, D., M. Miletto, W. Daily, A. Ramirez and E. Owen (1996), The effects of noise on Occam's inversion of resistivity tomography data: *Geophysics*, **61** (2), 538.

LaBrecque, D. and W. Daily, (2008), Assessment of measurement errors for galvanic-resistivity electrodes of different composition; *Geophysics*, **73** (2), F55–F64, 10.1190/1.2823457.

Lambs, L, (2004), Interaction between groundwater and surface water at river banks and the confluence of rivers, *Journal of Hydrology*, **288**.

Lesmes, D. P., and K. M. Frye (2001), Influence of pore fluid chemistry on the complex conductivity and induced polarization responses of Berea sandstone: *Journal of Geophysical Research*, **106** (B3), 4079 - 4090, doi: 10.1029/2000JB900392.

Lesmes, D. P., and S. P. Friedman (2005), Relationships between the electrical and hydrogeological properties of rocks and soils, in: Rubin, Y., Hubbard, S. (Eds.), *Hydrogeophysics*, Springer, **87**.

Lindberg, J. W. and F. W. Bond (1979), *Geohydrology and Groundwater quality beneath the 300 Area, Hanford site, Washington, Pacific Northwest Laboratory Richland, Washington 99352*.

Lindberg, J. W. and C. J. Chou (2001), *300 Area Process Trenches Groundwater Monitoring Plan, Prepared for the U.S. Department of Energy under Contract DE-AC06-76RL01830, Pacific Northwest National Laboratory, Richland, Washington 99352*.

Loke, M.H. 1996. *Tutorial : 2-D and 3-D electrical imaging surveys*.

Lowry, C. S., J. F. Walker, R. J. Hunt, and M. P. Anderson (2007), Identifying spatial variability of groundwater discharge in a wetland stream using a distributed temperature sensor, *Water Resources Research*, **43** (10), 1-9, doi:10.1029/2007WR006145.

Ma, R., C. Zheng, M. Tonkin, J. M. Zachara (2011), Importance of considering intraborehole flow in solute transport modeling under highly dynamic flow conditions, *Journal of Contaminant Hydrology*, **123** (1-2), 11-19.

Mansinha, L., R. Stockwell, R. Lowe, M. Eramian, R. Schincariol (1997a), Local S-spectrum analysis of 1-D and 2-D data, *Physics of The Earth and Planetary Interiors*, **103** (3-4), 329-336, doi: 10.1016/S0031-9201(97)00047-2.

Mansinha, L., R. Stockwell, and R. Lowe (1997b), Pattern analysis with two-dimensional spectral localisation: Applications of two-dimensional Stransforms, *Physica A: Statistical Mechanics and its Applications*, **239** (1-3), 286-295, doi: 10.1016/S0378-4371(96)00487-6.

Marshall, D.J. and T. Madden (1959), Induced Polarization, a study of its causes: *Geophysics*, **24** (4), 790.

Mwakanyamale, K. E., L. D. Slater, F. D. Day-Lewis, M. Elwaseif, and C. D. Johnson (2012), Spatially variable stage-driven groundwater-surface water interaction inferred from time-frequency analysis of distributed temperature sensing data, *Geophysical Research Letters*, **39**, 1-6, doi:10.1029/2011GL050824.

Newcomb, R.C., (1958), Ringold Formation of Pleistocene age in type locality, the White Bluffs, Washington: *American Journal of Science*, **256**, 328-340.

Olhoeft, G.R., (1985), Low frequency electrical properties: *Geophysics*, **50**, 2492-2503.

Patton G. P., B. L. Tiller, E. J. Antonio, T. M. Poston, and S. P. Van Verst (2003), Survey of Radiological and Chemical Contaminants in the Near-Shore Environment at the Hanford Site 300 Area, PNNL-13692, Rev. 1, Pacific Northwest National Laboratory, Richland, Washington.

Peterson, R. E. and M. P. Connelly, (1992), Characterization of a Chromium plume in groundwater along the Columbia River shoreline, Hanford Site, Washington, Westinghouse Hanford Company, Richland, Washington, WHC-SA-1674-VA.

Peterson, R. E. and M. P. Connelly, (2001), Zone of interaction between Hanford site groundwater and adjacent Columbia River, Progress report for the Groundwater/River Interface Task Science and Technology Groundwater/Vadose Zone Integration Project, Prepared for the U.S. Department of Energy under contract DE-AC06-76RL01830.

Peterson, R.E. and M.P. Connelly, (2004), Water movement in the zone of interaction between groundwater and the Columbia River, Hanford site, Washington: *Journal of Hydraulic Research*, **42**, 53-58.

Peterson, R. E., M. L. Rockhold, R. J. Serne, P. D. Thorne and M. D. Williams (2008), Uranium contamination in the subsurface beneath the 300 Area, Hanford site, Washington, Prepared for the U.S. Department of Energy under Contract DE-AC05-76RL01830.

Reynolds, J.M. (1998), An Introduction to Applied and Environmental Geophysics, John Wiley and Sons (Eds), England, 681-796.

Schmidt, C., R. Krieg and M. Bayer-Raich, (2005), Innovative methods to estimate water fluxes at the groundwater - surface water interface, ICID 21st European Regional Conference.

Schön, J.H., (1996), Physical properties of rocks: Fundamentals and principles of petrophysics. In Helbig, K. and Treitel, S. (Eds): *Handbook of geophysical exploration*, **18**, Pergamon Press, 583 pp.

Seigel, H. O. (1959), Mathematical formulation and type curves for induced polarization: *Geophysics*, **24** (3), 547.

Selker, J. S., L. Thévenaz, H. Huwald, A. Mallet, W. Luxemburg, N. van de Giesen, M. Stejskal, J. Zeman, M. Westhoff, and M. B. Parlange (2006a), Distributed fiber-optic temperature sensing for hydrologic systems, *Water Resources Research*, **42** (12), 1-8, doi:10.1029/2006WR005326.

Selker, J., N. van de Giesen, M. Westhoff, W. Luxemburg, and M. B. Parlange (2006b), Fiber optics opens window on stream dynamics, *Geophysical Research Letters*, **33** (24), 6-9, doi:10.1029/2006GL027979.

Serne, R. J., R. E. Clayton, I. V. Kutnyakov, G. V. Last, V. L. LeGore, T. C. Wilson, H. T. Schaef, M. J. O'Hara, K. B. Wagnon, D. C. Lanigan, C. F. Brown, B. A. Williams, C. W. Lindenmeier, R. D. Orr, D. S. Burke, C. C. Ainsworth (2002), Characterization of vadose zone sediment: Borehole 41-09-39 in the S-SX Waste Management Area, Prepared for CH2M HILL Hanford Group, Inc., and the U.S. Department of Energy under Contract DE-AC06-76RL01830.

Shuey, R. T. and M. Johnson (1973), On the phenomenology of electrical relaxation in rocks: *Geophysics*, **38** (1) 37.

Sinokrat, B. A. and H. G. Stefan (1993), Stream temperature dynamics: Measuring and modeling, *Water Resources Research*, **29**(7), 2299-2312.

Slater, L. D. and D. Lesmes (2002), IP interpretation in environmental investigations: *Geophysics*, **67** (1), 77, doi:10.1190/1.1451353.

Slater, L., and A. Binley (2003), Evaluation of permeable reactive barrier (PRB) integrity using electrical imaging methods: *Geophysics*, **68** (3), 911–921, 10.1190/1.1581043.

Slater, L., and A. Binley (2006), Synthetic and field-based electrical imaging of a zerovalent iron barrier: Implications for monitoring long-term barrier performance: *Geophysics*, **71** (5), B129–B137, 10.1190/1.2235931.

Slater, L., D. Ntarlagiannis, and D. Wishart (2006), On the relationship between induced polarization and surface area in metal-sand and clay-sand mixtures: *Geophysics*, **71** (2), A1, doi: 10.1190/1.2187707.

Slater, L. D., D. Ntarlagiannis, F. D. Day-Lewis, K. Mwakanyamale, R. J. Versteeg, A. Ward, C. Strickland, C. D. Johnson, and J. W. Lane Jr. (2010), Use of electrical imaging and distributed temperature sensing methods to characterize surface water–groundwater exchange regulating uranium transport at the Hanford 300 Area, Washington: *Water Resources Research*, **46**, doi:10.1029/2010WR009110.

Steinhorst, R. K. and R. E. Williams (1985), Discrimination of groundwater sources using Cluster Analysis, MANOVA, Canonical Analysis and Discriminant Analysis, *Water Resources Research*, **21** (8), 1149-1156.

Stockwell, R. G., L. Mansinha, and R. P. Lowe (1996), Localization of the complex spectrum: the S-transform, *IEEE Transactions on Signal Processing*, **44** (4), 998-1001, doi:10.1109/78.492555.

Stonestrom, D. A. and J. Constantz (Eds.) (2003), Heat as a tool for studying the movement of groundwater near streams, USGS Circular 1260, United States Geological Survey, Reston, Va.

Tyler, D. K. (1992), Assessment of potential environmental impacts from continued discharge to the 300 Area process trenches at Hanford, WHC-SD-WM-EE-005, Rev. 0, Westinghouse Hanford Company, Richland, Washington.

Ulrich, C. and L. Slater (2004), Induced polarization measurements on unsaturated unconsolidated sands: *Geophysics*, **69** (3), 762.

Van Voorhis, G. D., H. Nelson, and T. L. Drake (1973), Complex resistivity spectra of porphyry Copper mineralization: *Geophysics*, **38** (1), 49.

Vinegar, H. J. and M. H. Waxman (1984), Induced Polarization of shaly sands: *Geophysics*, **49** (8), 1267.

Wait, J. R. (1984), Relaxation phenomena and induced polarization: *Geoexploration*, **22**, 107-127.

Waxman, M.H. and L.J.M. Smits (1968), Electrical conduction in oil-bearing shaly sands: *Society of Petroleum Engineers Journal*, **8**, 107.

Waxman, M. H. and E. C. Thomas (1974), Electrical conductivities in shaly sands: *Society of Petroleum Engineers Journal*, **14**, 213.

Weller, A., L. Slater, S. Nordsiek, and D. Ntarlagiannis (2010), On the estimation of specific surface per unit pore volume from induced polarization: A robust empirical relation fits multiple data sets: *Geophysics*, **75** (4).

Weller, A., K. Breede, L. Slater, and S. Nordsiek (2011), Effect of changing water salinity on complex conductivity spectra of sandstones: *Geophysics*, **76**.

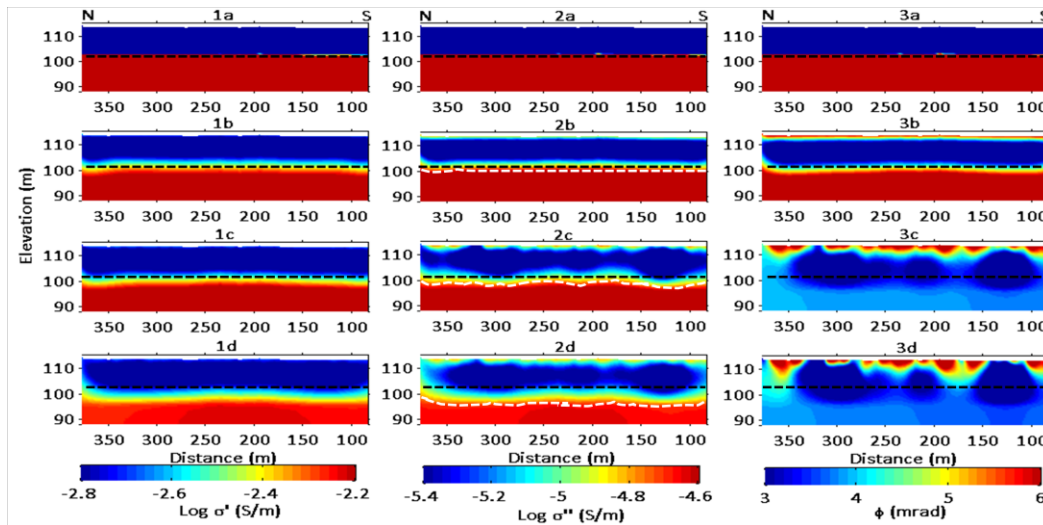
Williams, B. A., C. F. Brown, W. Um, M. J. Nimmons, R. E. Peterson, B. N. Bjornstad, D. C. Lanigan, R. J. Serne, F. A. Spane, and M. L. Rockhold (2007), Limited field investigation report for uranium contamination in the 300 Area, 300 FF - 5 operable unit, Hanford site, Washington, Rep.PNNL - 16435, Pacific Northwest National Laboratory, Richland, Washington.

Zachara, J. M., J. Serne, M. Freshley, F. Mann, F. Anderson, M. Wood, T. Jones, and D. Myers (2007), Geochemical processes controlling migration of tank wastes in Hanford's vadose zone: *Vadose Zone Journal*, **6** (4), 985–1003.

APPENDICES

Appendix A. Supplemental material for Chapter 3

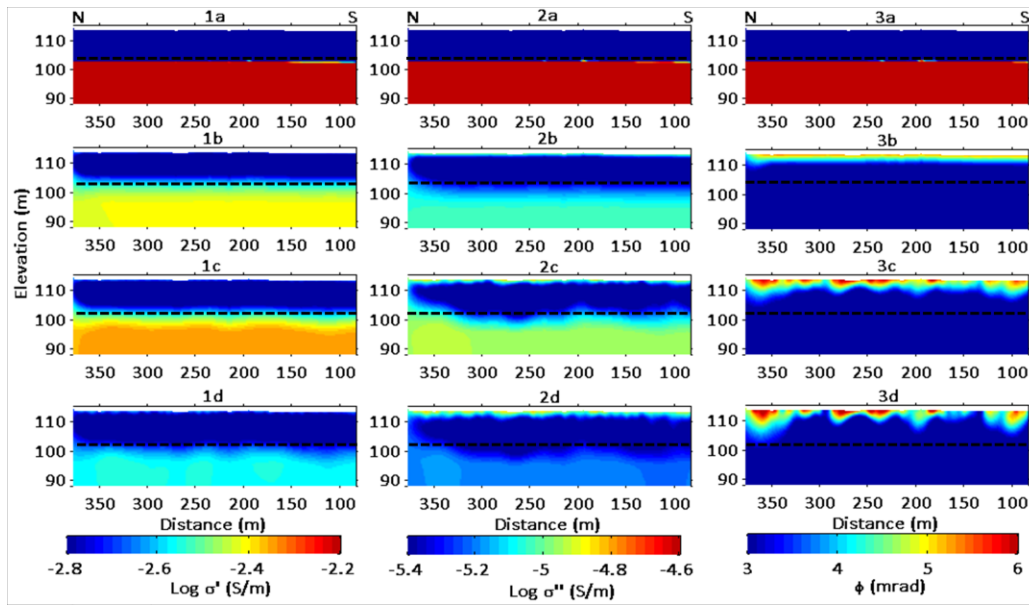
1. Inversion results of the synthetic data from Model 1, a 2-layer model for a uniform H-R contact (no paleochannel) with the survey configuration used in field (1a) model of $\log \sigma'$ (1b) inversion results with field error (1c) inversion results with $\sigma_d = 0.02$ (1d) inversion results with $\sigma_d = 0.1$ (2a) model of $\log \sigma''$ (2b) inversion results with field error (2c) inversion results with $\sigma_d = 0.02$ (2d) inversion results with $\sigma_d = 0.1$ (3a) model of ϕ (3b) inversion results with field error (3c) inversion results with $\phi_d = 2$ mrad (3d) inversion results with $\phi_d = 4$ mrad. The black dashed lines represent the true H-R contact in the model while the white dashed lines on σ'' images represent the resolved H-R contact from inversion of the synthetic data, using $\log(\sigma'')$ (S/m) = -4.7 threshold.



The Hanford and Ringold Formations are generally very well resolved with no evidence of variable resolution along the profile due to varying sensitivity from the measurement

sequence. The estimated H-R contact presented by the white dashed lines on the Figure above is well resolved at the field error levels on 2b and coincides closely with the modeled H-R contact (black dashed line). With an increase in error level, the estimated depths (white lines) deviates further from the true depths (black lines) (2c and 2d). At the highest error levels, artifacts start to develop in the near surface (e.g. 111 m – 114 m) (1d and 2d) even though the main structure of the H-R contact can still be resolved. Phase angles show high sensitivity to errors, resulting in severe loss of model structure with increasing noise level. In fact, evidence of the H-R contact can only clearly be resolved in the σ image with the field error estimate (3b) as significant distortion of true model structure is observed even for the lowest synthetic error level (1 mrad). At 2 mrad and higher error levels, there is no evidence of the H-R contact and artifacts are severe enough to result in an anomalous thin layer of high phase angle (3d).

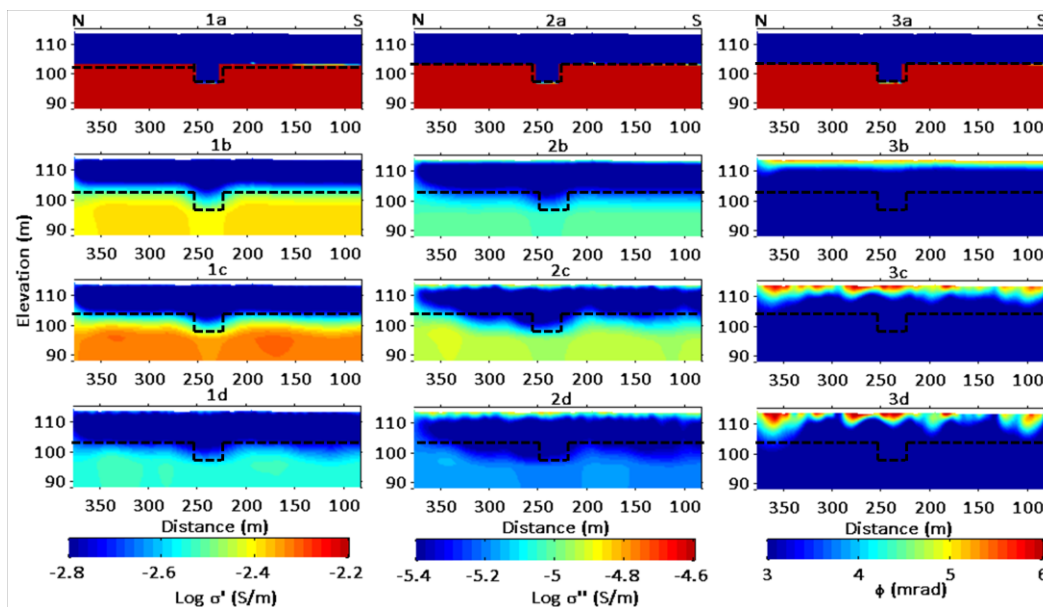
2. Inversion results of the synthetic data from Model 1, a 2-layer model for a uniform H-R contact (no paleochannel) with the dipole-dipole configuration (1a) model of $\log \sigma'$ (1b) inversion results with field error (1c) inversion results with $\sigma_d = 0.02$ (1d) inversion results with $\sigma_d = 0.1$ (2a) model of $\log \sigma''$ (2b) inversion results with field error (2c) inversion results with $\sigma_d = 0.02$ (2d) inversion results with $\sigma_d = 0.1$ (3a) model of ϕ (3b) inversion results with field error (3c) inversion results with $\phi_d = 2$ mrad (3d) inversion results with $\phi_d = 4$ mrad. The black dashed lines represent the modeled H-R contact. Inversion of the synthetic data from dipole-dipole configuration is unable to resolve the H-R contact using $\log(\sigma'')$ (S/m) = -4.7 threshold.



The dipole-dipole configuration proved unable to resolve the H-R contact based on the $\log_{10}(\sigma'')$ (S/m) = -4.7 S/m threshold at all error levels, although a 2-layer structure is evident from the images. Resolution of the true two layer structure is generally low in the σ'' and ϕ images, even for the dataset containing the field errors (the lowest errors assessed). Evidence of distortion in the σ'' model structure appears at $\sigma_d = 0.02$ and worsens with increasing noise levels. The H-R contact is poorly resolved in the ϕ image. For all error levels, I see a thin high phase layer at a depth of 102 m -115 m. The thickness of this layer increases with the error level (3b – 3d). The two units are significantly better resolved in the σ' image, with significant distortion of model structure only at $\sigma_d = 0.1$.

3. Inversion results of the synthetic data from Model 2, a two layers model with included simulated paleochannel incised into the bottom layer (the Ringold Formation) with the dipole-dipole configuration (1a) model of $\log \sigma'$ (1b) inversion results with field error (1c) inversion results with $\sigma_d = 0.02$ (1d)

inversion results with $\sigma_d = 0.1$ (2a) model of $\log \sigma''$ (2b) inversion results with field error (2c) inversion results with $\sigma_d = 0.02$ (2d) inversion results with $\sigma_d = 0.1$ (3a) model of ϕ (3b) inversion results with field error (3c) inversion results with $\phi_d = 2$ mrad (3d) inversion results with $\phi_d = 4$ mrad. The black dashed lines represent the true H-R contact in the model. Inversion of the synthetic data from dipole-dipole configuration is unable to resolve the H-R contact, using $\log(\sigma'')$ (S/m) = -4.7 threshold, even though the visual evidence of the modeled paleochannel is present up to $\sigma_d = 0.02$



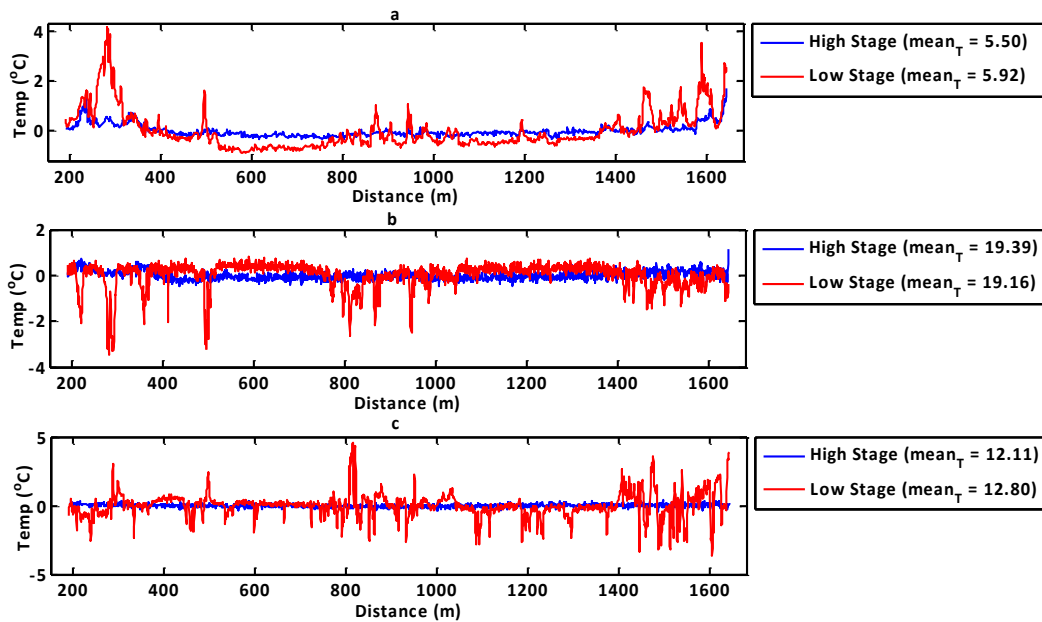
It is interesting to note that visual evidence for the depression is clearer in the images obtained with the dipole-dipole configuration for $\sigma_d = 0.02$ (1b & 1c) and (2b & 2c). However, the true complex conductivity of each unit is again not well recovered when compared to the field configuration.

Due to its relatively poor vertical resolution [Loke, 1994-2004], the dipole-dipole configuration was unable to resolve the H-R contact based on the threshold in the

imaginary conductivity data derived from laboratory measurements. It is interesting to note that the modeled paleochannel feature is well resolved in the dipole-dipole configuration due to its high lateral resolution [Loke, 1994-2004]. However, despite its long popularity in IP surveys due to the reduction in EM coupling effects, the dipole-dipole survey is often not a viable field acquisition protocol due to the low SNR resulting from large separation between current and potential electrodes.

Appendix B. Supplemental material for Chapter 4

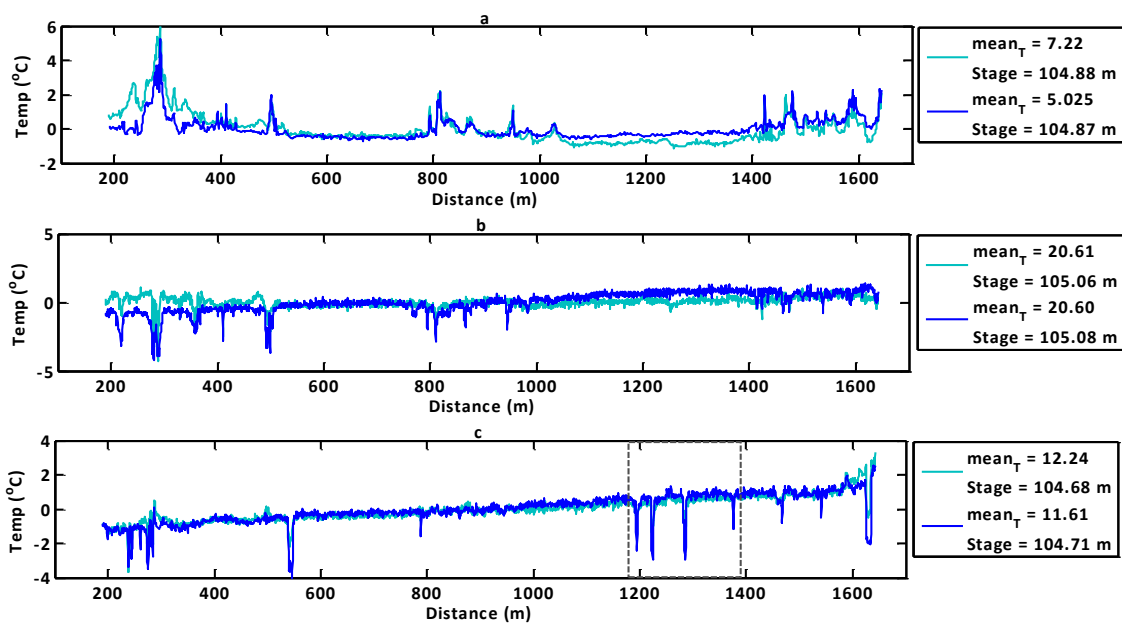
- Temperature responses to river stage fluctuation. (a) Detrended winter temperature on, February 27, 2009 (day 57.6033) during high river stage (105.38 m) and February 28, 2009 (day 58.6033) during low river stage (104.77 m). (b) Detrended summer temperature on, July 4, 2009 (day 184.1335) during low river stage (104.8 m) and July 17, 2009 (day 197.8418) during high river stage (105.75 m). (c) Detrended fall temperature on, November 17, 2009 (day 320.8023) during low river stage (104.35 m), November 19, 2009 (day 322.3995) during high river stage (105.63 m).



At low river stage, the detrended temperature shows variations along the entire cable length. For some locations along the cable, riverbed temperature varied by more than 4 °C in both winter and summer data, in response to decrease in river stage. Such variations appear as spikes in temperature between cable length 200 – 360 m, 480 – 520 m, 780 –

960 m and 1440 – 1640 m. The prominent locations that show temperature variations at low river stage are consistent in both winter and summer data. There are additional locations in the November data between cable length 1100 – 1300 m that exhibit anomalous temperature characteristics of cold groundwater input. These additional locations are not present in the winter and summer sampling periods. There are no significant variations in temperature for the entire cable length during high river stage. The appearance and disappearance of the anomalous temperatures along the cable can occur within a day or within days depending on the river stage fluctuation.

2. Temperature deviation from mean temperature at 6 am (blue) and at 6 pm (teal).
 - (a) Winter – detrended temperature on day 64 (March 06 2009). (b) Summer – detrended temperature on day 185 (July 05, 2009). (c) Fall – detrended temperature on day 325 (November 22, 2009). Gray dashed box represents fall temperature anomalies inconsistent with winter and summer data.



Temperature anomalies are evident in winter, summer and fall data, irrespective of diurnal variations in temperature. Figure above shows deviation in riverbed temperature from the mean temperature at 6 am (blue) and at 6 pm (teal) where the difference in river stage was ≤ 0.2 m. Temperatures plotted on the figure above were recorded during low river stage. The locations exhibiting anomalous temperatures shows significant deviation from the mean temperatures, an observation that is expected assuming groundwater input in these locations. This contrast in temperature is higher at the time of the day with the highest mean temperature (at 6 pm).

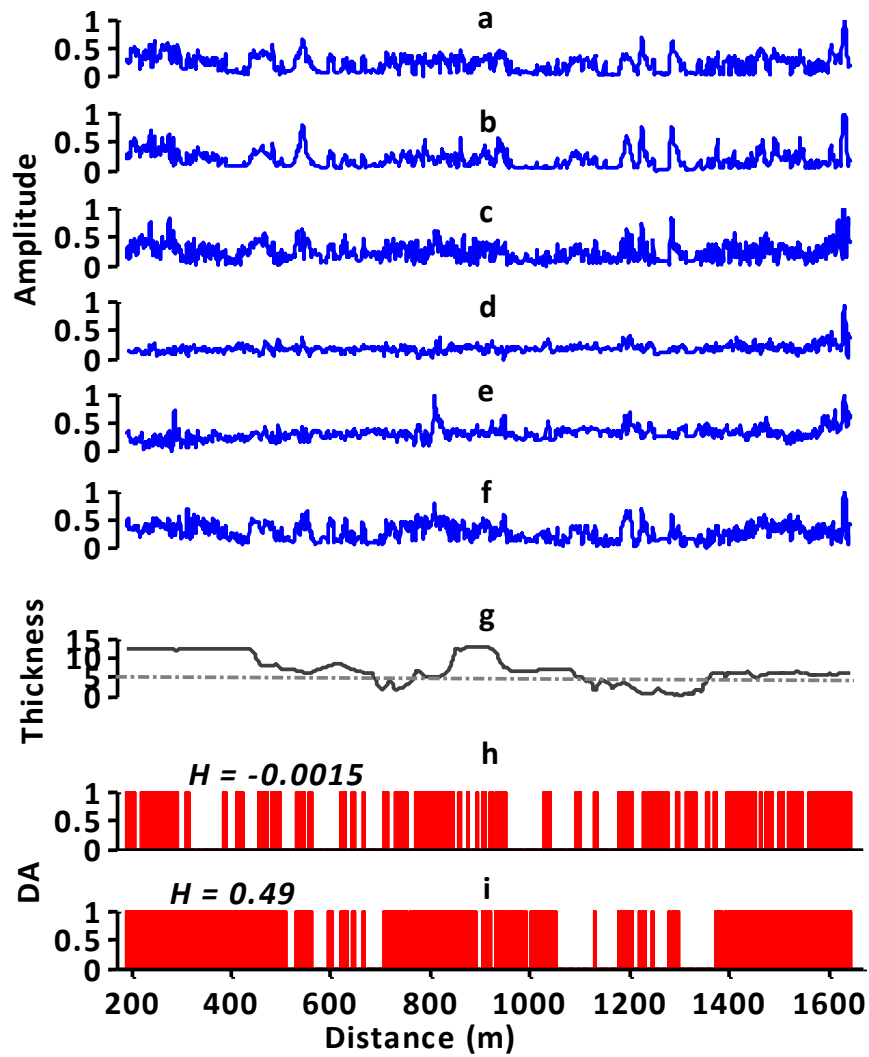
Although different seasons (winter, summer and fall) experienced similar fluctuations in river stage over short (hourly) time periods, the location of some of the discharge zones varied with seasons. Most discharge zone locations appeared consistently in the winter (January – March) and summer (June – August) where significant difference in temperatures between groundwater and the surface water exist. I suspect that, the anomalous discharge location in November data at 1100 m – 1300 m is a false positive due to lack of significant difference in temperatures between groundwater and the surface water. This being the case, other factors that do not play a key role during winter and summer, for example, shading from vegetation on the river bank or length of the water column above the cables (due to different water depth), will affect the temperature recorded at this location. A deeper water column could cause cooler temperature anomalies observed at these locations; on the other hand, vegetation (tree cover) could cause shades on this location also resulting in cooler water column. The effect of afore mentioned factors is overshadowed by the solar radiation effect in the winter and summer months.

Appendix C. Supplemental material for Chapter 5

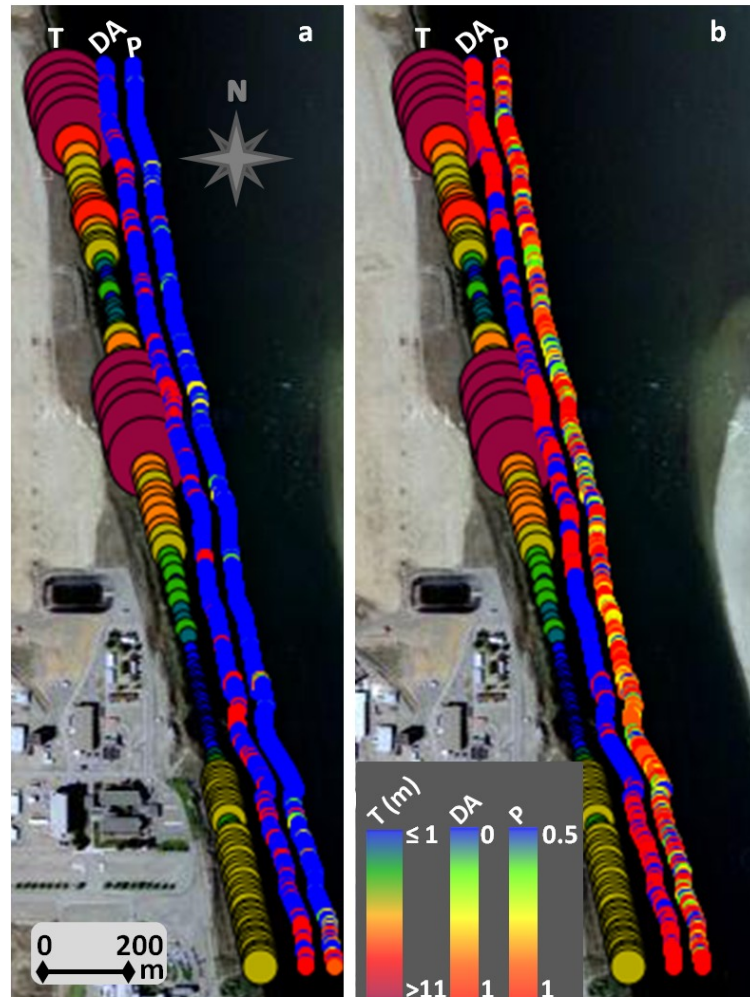
Table 1. Classification performance of discriminant analysis for exchange and non exchange zones. Feb, July and Nov, represents classification performance results when using all periods (0.5 – 8 days) for winter, summer and fall respectively, Feb P4, July P4 and Nov P4, represents classification performance results when using 4 days periods for winter, summer and fall respectively. All data represents classification performance results when using all amplitudes from all sampling seasons and 1/11 and 1/21 represents classification performance results when using limited data of all amplitudes from all sampling seasons.

| | Feb | | July | | Nov | | Feb P4 | | July P4 | | Nov P4 | | All data | | 1/11 data | | 1/21 data | |
|-------------------------|---------|------|---------|------|---------|------|---------|------|---------|-----|----------|-----|----------|------|-----------|------|-----------|------|
| Confusion Matrix | 644 | 39 | 668 | 15 | 570 | 113 | 636 | 47 | 629 | 54 | 520 | 163 | 657 | 26 | 643 | 40 | 527 | 158 |
| | 627 | 1561 | 772 | 1416 | 748 | 1440 | 1148 | 1040 | 1274 | 914 | 1669 | 519 | 457 | 1731 | 391 | 1797 | 215 | 1973 |
| Hardness | 0.65634 | | 0.62520 | | 0.49269 | | 0.40651 | | 0.33867 | | -0.00145 | | 0.75307 | | 0.76273 | | 0.6704 | |

1. FFT and DA results for fall data (November) (a) normalized amplitude of 0.5 day period (b) normalized amplitude of 1 day period (c) normalized amplitude of 3 days period (d) normalized amplitude of 4 days period (e) normalized amplitude of 6 days period (f) normalized amplitude of 8 days period (g) Hanford Formation thickness as estimated from continuous waterborne electrical imaging measurements [Slater *et al.*, 2010]. The gray dashed line indicates the 5 m threshold used as a cut-off for identifying exchange vs. non-exchange zones. DA classification results. The red bars indicate areas classified as groundwater exchange zones (h) DA results using amplitude from period 4 days in the fall (i) DA results using amplitudes from all periods in the fall.



2. Map view of; Hanford Formation thickness (T) as estimated from continuous waterborne electrical imaging measurements [Slater *et al.*, 2010], DA results and posterior probability (P) of DA classification, (a) single amplitude of period 4 days from fall data (b) all amplitudes of all periods in the fall.



- Map view of; Hanford Formation thickness (T) as estimated from continuous waterborne electrical imaging measurements [Slater *et al.*, 2010], DA results and posterior probability (P) of DA classification, (a) all amplitudes of all periods from all sampling seasons at 1/21 sample size (b) all amplitudes of all periods from all sampling seasons at 1/11 sample size.



CURRICULUM VITAE

- 1979 Born June 15th in Tanga, Tanzania
- 2001 Graduated from Jangwani High School in Dar es Salaam, Tanzania
- 2001 – 2005 Attended University of Dar es Salaam, Dar es Salaam, Tanzania
Major in Chemistry and Geology
- 2004 Internship at Geita Gold Mining, Mwanza, Tanzania
- 2005 B.Sc. with Geology, University of Dar es Salaam
- 2005 – 2007 Masters student, Western Michigan University, Kalamazoo, MI
- 2005 – 2006 Rood Scholarship, Western Michigan University, Kalamazoo, MI
- 2006 – 2007 Teaching Assistant, Western Michigan University, Kalamazoo, MI
- 2007 M.Sc. of Geology, Western Michigan University
- 2007 – 2012 Ph.D. student, Rutgers University, Newark, New Jersey
- 2007 – 2011 Teaching Assistant, Rutgers University, Newark, New Jersey
- 2011 – 2012 Dissertation Fellowship, Rutgers University, Newark, New Jersey
- 2012 Article “Spatially variable stage-driven groundwater-surface water interaction inferred from time-frequency analysis of distributed temperature sensing data”, *Geophysical Research Letters*, **39**, L06401, doi:10.1029/2011GL050824, 2012
- 2012 Article “Lithologic Imaging Using Complex Conductivity: Lessons Learned from the Hanford 300 Area”, *Geophysics*, **77** (6), P. 1–13, 10.1190/GEO2011-0407.1.
- 2012 Internship at ExxonMobil Exploration Company, Houston, Texas